

2006

Resonant cavity enhanced (RCE) techniques for increasing the efficiency of quantum well photodetectors

Jang Pyo Kim
University of Dayton

Follow this and additional works at: https://ecommons.udayton.edu/graduate_theses

Recommended Citation

Kim, Jang Pyo, "Resonant cavity enhanced (RCE) techniques for increasing the efficiency of quantum well photodetectors" (2006). *Graduate Theses and Dissertations*. 3923.
https://ecommons.udayton.edu/graduate_theses/3923

This Dissertation is brought to you for free and open access by the Theses and Dissertations at eCommons. It has been accepted for inclusion in Graduate Theses and Dissertations by an authorized administrator of eCommons. For more information, please contact mschlange1@udayton.edu, ecommons@udayton.edu.

Resonant Cavity Enhanced (RCE) Techniques for Increasing the Efficiency of Quantum Well Photodetectors

Dissertation

Submitted to

The School of Engineering of the

UNIVERSITY OF DAYTON

in Partial Fulfillment of the Requirements for

The Degree

Doctor of Philosophy in Electro-Optics

by

Jang Pyo Kim

UNIVERSITY OF DAYTON

Dayton, Ohio

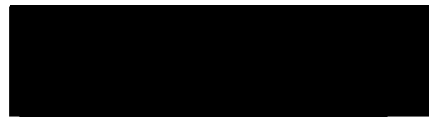
May, 2006

Resonant Cavity Enhanced (RCE) Techniques for Increasing the Efficiency of Quantum Well Photodetectors

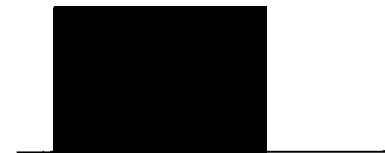
APPROVED BY:



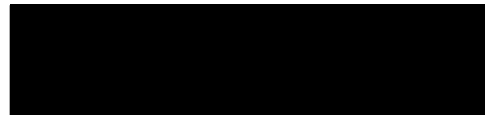
Andrew M. Sarangan, Ph.D.
Associate Professor,
Electro-Optics Program
Committee Chairman



Joseph W. Haus, Ph.D.
Director and Professor,
Electro-Optics Program
Committee Member



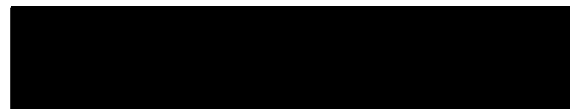
Partha P. Banerjee, Ph.D.
Professor,
Electro-Optics Program
Committee Member



Robert J. Brecha, Ph.D.
Associate Professor,
Department of Physics
Committee Member



Donald L. Moon, Ph.D.
Associate Dean and Professor,
Graduate Engineering
Program and Research
School of Engineering



Joseph E. Saliba, Ph.D., P.E.
Dean, School of Engineering

ABSTRACT

RESONANT CAVITY ENHANCED (RCE) TECHNIQUES FOR INCREASING THE EFFICIENCY OF QUANTUM WELL PHOTODETECTORS

Name: Jang Pyo Kim

University of Dayton

Advisor: Dr. Andrew M. Sarangan

In this dissertation, a novel resonant cavity enhanced (RCE) photodetectors for enhanced quantum efficiency (QE) is studied. By utilizing a resonant cavity around the active region, RCE photodetectors enable the photons to make multiple passes across the active region, improving the probability of absorption. This feature also makes the detector very sensitive to the incident wavelength and the incident angle. Thus several numerical techniques such as a finite difference time domain (FDTD) method as well as a transfer matrix method (TMM) have been developed under this work, and the RCE concept has been applied to novel device structures, including the quantum well infrared photodetectors (QWIP) for long-wavelength applications. The key advantage of using the FDTD method is that it accurately captures the energy distribution inside the cavity as a

function of time. This build-up time is an important factor in RCE photodetectors designed for high-speed operations.

As a step towards FDTD simulation, a temperature-dependent Sellmeier equation for $\text{Al}_x\text{Ga}_{1-x}\text{As}$ compounds has been derived. Since QWIP and corrugated QWIP (C-QWIP) typically operate at cryogenic temperatures, it is important to know their refractive indices at these low temperatures. This refractive index model is applied to the analysis of the device structures.

Both grating-coupled QWIP and C-QWIP are investigated and simulated using the FDTD method. Although these structures have been proven to have high reliability and ease of manufacture in infrared applications, their low quantum efficiencies make them less favorable compared to mercury cadmium telluride (HgCdTe) detectors, which have nearly 100% QE. In order to alleviate some of these problems, a novel RCE approach is proposed for the QWIP and C-QWIP structures to enhance their QE and to make them more attractive. These structures are named RCE-QWIP and RCE-CQWIP, respectively. QE is even further enhanced in the RCE-CQWIP by using a novel implementation that includes a form birefringence layer to overcome the polarization selection rule in quantum well sub-band transitions. This structure allows part of the remaining half of the photons to be absorbed, significantly increasing the QE. Dependence of QE on the angle of incidence in both cases is also discussed.

ACKNOWLEDGEMENTS

I am greatly indebted to the many people who have helped over the last five years. Above all, my advisor, Dr. Andrew M. Sarangan, is the one I want to acknowledge due to his excellent advice and continuous guidance to bring my research to a conclusion. He always gave me such wonderful ideas to broaden the depth of my knowledge. In addition, because he is a leading scientist in the fields of semiconductor, optoelectronics and nano-fabrication technology, I am especially honored to be his first Ph.D. graduate and I will be forever grateful to him.

I also want to acknowledge Dr. Joseph W. Haus, one of my committee members and the Electro-Optics Program Director. He is a well known scientist and professor in quantum optics and photonic crystals who, based on his strong leadership ability, has a passion for promoting the Electro-Optics Program. He was always kind enough to take care of any request I made and willing to respond to any problem that I encountered. Because of his vast experience in a variety of fields, it was a delight for me to share in his knowledge of optics.

I am grateful to Dr. Partha P. Banerjee, one of my committee members, for his continuous support throughout my study. He is a former chair of the Electrical and

Computer Engineering Department, and is also a renowned scientist, especially in the fields of photorefractive materials, nonlinear optics, acoustic optics, and image processing. Because of his excellent instruction in my Linear System and Fourier Optics (EOP 513) class, my knowledge of Fourier analysis was enhanced significantly compared with a similar subject I studied in my master's program. Also he has served as an advisor of SPIE student chapter at UD. Under his guidance, many of the SPIE student members benefited from the privileges it offered.

I am also indebted to Dr. Robert J. Brecha, one of my committee members, for his understanding and help. He is an expert in the fields of quantum optics and ultracold atoms. I worked with him for a couple of semesters as a teaching assistant for the Optical Radiation and Matter (EOP 502) course.

There is a special person I would like to acknowledge. He is Mr. Aziz Mahfoud Familia, my year-long partner since 2001. We started the Ph.D. program at the same time and since then we have done almost everything together. We took the same courses, conducted outreach activities, and attended several conferences, to name a few. I strongly feel that I am fortunate to have him during my study and I believe this partnership will last for many years to come. I also thank our group members, Ms. Cijy E. Sunny and Mrs. Lirong Sun, for their help and collaboration. It was a pleasure to work with all of them in the same group with Dr. Sarangan. There are, of course, many other fellow colleagues including Cong, Joe, May, George, Zasim, Masud that I need to express my sincere appreciation because of their direct or indirect support. I appreciate their cooperation.

Also all of the professors at the University of Dayton who taught me during my study deserve receiving my acknowledgement. These professors include Dr. Loomis for Geometric Optics (EOP 501), Dr. Duncan for Guided Wave Optics (EOP 514), and Dr. Yaney for Advanced Electro-Optics Lab (EOP 543L). Thanks go to Dr. Powers for letting me use his lab and giving me valuable suggestions for determining the temperature-dependent refractive index of $\text{Al}_x\text{Ga}_{1-x}\text{As}$. I also thank Dr. Zhan for his fruitful discussion on the simulation of the form birefringence layer. Furthermore, I should not neglect the assistance from previous and present staffs of the Electro-Optics Program: Trina, Nancy, and Erin.

I take this opportunity to acknowledge my family. First of all, Hyun Ju Lee, my devoted wife and lifelong friend, is entitled to receive all the credit because of her continuous cooperation and sincere understanding. Throughout our marriage she has shown her faithful support despite the difficult situations we have faced. I have shared joys and sorrows with her since 1988. Also, my beloved children, Jin Young Kim and Ho Young Kim, are the reason why I came to the U.S.A. They always encouraged me when I encountered difficult circumstances. I couldn't overcome all of these obstacles without their help and cooperation. For this reason, this achievement is not mine alone but ours together.

Finally, I thank the Dayton Area Graduate Studies Institute (DAGSI) for its financial assistance since 2002. Without its help, I could not have completed my research successfully.

TABLE OF CONTENTS

ABSTRACT.....	iii
ACKNOWLEDGEMENTS.....	v
LIST OF FIGURES	xii
LIST OF TABLES	xvii
LIST OF SYMBOLS	xviii
LIST OF ABBREVIATIONS.....	xx
OVERVIEW OF DISSERTATION	xxii
CHAPTER	
I. INTRODUCTION	1
II. REVIEW OF RELATED RESEARCH	4
2.1 Introduction.....	4
2.2 Quantum efficiency of photodetectors.....	5
2.2.1 Conventional photodetectors	6
2.2.2 RCE photodetectors	7
2.3 Angle dependence of quantum efficiency	13
2.4 Transfer Matrix Method (TMM)	15
2.4.1 Formulation of the quantum efficiency for RCE photodetectors using TMM	16

2.4.2 Results and discussion	19
2.5 Finite Difference Time Domain (FDTD).....	22
2.5.1 Formulation of the FDTD method	22
2.5.2 Results and discussion	24
2.5.2.1 Optical field distribution in GaAs/ $\text{In}_{0.2}\text{Ga}_{0.8}\text{As}$ detector	24
2.5.2.2 Quantum efficiency in GaAs/ $\text{In}_{0.2}\text{Ga}_{0.8}\text{As}$ detector	27
2.5.2.3 MCT detector using FDTD method.....	29
2.6 Conclusion	32
III. DETERMINATION OF TEMPERATURE-DEPENDENT REFRACTIVE INDEX OF $\text{Al}_x\text{Ga}_{1-x}\text{As}$ MATERIAL	33
3.1 Introduction.....	33
3.2 Experimental setup	34
3.3 Results and discussion	37
3.4 Conclusion	42
IV. GRATING-COUPLEDD QUANTUM WELL INFRARED PHOTODETECTOR (QWIP).....	44
4.1 Introduction.....	44
4.2 Polarization selection rule.....	46
4.2.1 Dipole matrix element	46
4.2.2 The oscillator strength	48
4.3 Vector diagram of light propagation in different structures	49
4.4 Theory	51
4.4.1 Scattering matrix of the lamellar grating	51

4.4.2	Transfer matrices and the coupling of the grating to the MQW structure	55
4.4.3	Calculation of quantum efficiency	57
4.4.4	FDTD method in 2-dimensions	58
4.4.4.1	The perfectly matched layer (PML)	60
4.5	Schematic diagram of grating-coupled QWIP	61
4.6	Schematic diagram of grating-coupled QWIP with an AlAs layer	61
4.7	Schematic diagram of grating-coupled RCE-QWIP	63
4.8	Simulation results and discussion	64
4.8.1	Quantum efficiency at normal incidence	64
4.8.1.1	Numerical calculation	64
4.8.1.2	FDTD simulation	64
4.8.1.3	Result and discussion	65
4.8.2	Quantum efficiency as a function of incidence	68
4.8.3	Steady-state analysis using FDTD	69
4.9	Conclusion	70
V.	RESONANT CAVITY ENHANCED (RCE) CORRUGATED QUANTUM WELL INFRARED PHOTODETECTORS (C-QWIP)	71
5.1	Introduction	71
5.2	Schematic diagram of RCE-CQWIP	72
5.3	Simulation results and discussion	74
5.4	Conclusion	78
VI.	RCE-CQWIP WITH A FORM BIREFRINGENCE LAYER	79
6.1	Introduction	79

6.2 Background of form birefringence	80
6.3 Schematic diagram of a form birefringence layer	84
6.4 Second-order effective medium theory (EMT)	85
6.5 Rigorous coupled wave analysis (RCWA)	87
6.6 Numerical simulation and comparison	94
6.7 Schematic diagram of RCE-CQWIP with a form birefringence layer	98
6.8 Simulation results and discussion	99
6.9 Conclusion	103
VII. CONCLUSIONS	104
BIBLIOGRAPHY	107
VITA	113

LIST OF FIGURES

Fig. 2-1. Schematic diagram of a conventional junction photodetector (after reference [1]).....	6
Fig.2-2. Analytical model of a RCE photodetector (after reference [2]).....	7
Fig.2-3. Quantum efficiency as a function of the normalized absorption coefficient for $\lambda = 900\text{nm}$ at different values of R_1 and R_2 (equation (2-10)).....	10
Fig.2-4. Wavelength dependence of quantum efficiency of RCE detectors for $R_1 = 0.3$ and $R_2 = 0.99$ (equation (2-9))	10
Fig.2-5. Quantum efficiency versus channel thickness dependence for $\lambda_1 = 820\text{nm}$ and for reflectivities $r_1 = 0.7$ and $r_1 = 0.3$ (after reference [4]).....	12
Fig.2-6. Quantum efficiency versus channel thickness dependence for $\lambda_2 = 532\text{nm}$ and for reflectivities $r_1 = 0.7$ and $r_1 = 0.3$ (after reference [4]).....	12
Fig.2-7. Degradation of η for off-angle incidence at $\lambda = 1.0$ and $1.5 \mu\text{m}$ for $F = 10$ and 20 (equation (2-12))	15
Fig.2-8. Analytical model of a RCE photodetector using TMM	16
Fig.2-9. Calculated quantum efficiency as a function of the normalized absorption coefficient for $\lambda = 900\text{nm}$ and at different values of R_1 and R_2 using TMM	20
Fig.2-10. Wavelength dependence of quantum efficiency for RCE detectors for $R_1 = 0.3$ and $R_2 = 0.99$ using TMM	20

Fig.2-11. Quantum efficiency versus channel thickness dependence for $\lambda_1 = 820\text{nm}$ and for reflectivities $r_1 = 0.7$ and $r_1 = 0.3$ by using TMM.....	21
Fig.2-12. Quantum efficiency versus channel thickness dependence for $\lambda_2 = 532\text{nm}$ and for reflectivities $r_1 = 0.7$ and $r_1 = 0.3$ by using TMM.....	21
Fig.2-13. Dependence of QE on incident angle at wavelength of $1\ \mu\text{m}$ for $F=10$. Dashed line shows efficiency decrease $\Delta\eta/\eta$ derived by Kishino <i>et al.</i> [2] and solid line represents $\Delta\eta/\eta$ using TMM	22
Fig.2-14. Optical field distribution in a RCE photodetector with no absorption.....	25
Fig.2-15. Optical field distribution in a RCE photodetector. with absorption.....	26
Fig.2-16. The energy distribution inside the cavity as a function of time with absorption. The steady-state condition is reached at $540\ \text{fs}$	26
Fig.2-17. Calculated η as a function of the normalized absorption coefficient. Dashed line shows η , derived by analytical model, and circle and solid line represent η , using FDTD and TMM, respectively	29
Fig.2-18. Schematic diagram of RCE-HgCdTe detector	30
Fig.2-19. Optical field distribution in a RCE-MCT photodetector. with absorption.....	31
Fig.2-20. The energy distribution inside the cavity as a function of time with absorption.....	31
Fig.3-1. Longitudinal schematic diagram of experimental sample.....	35
Fig.3-2. Photograph of the experimental setup.....	35
Fig.3-3. Transmission spectrum shift vs. temperature on sample as a function of wavelength	36

Fig.3-4. Contour plot of the transmission of the sample with change in the refractive index of GaAs and AlAs	38
Fig.3-5. Refractive indices of AlAs and GaAs as a function of temperature	39
Fig.3-6. Refractive index of $\text{Al}_x\text{Ga}_{1-x}\text{As}$ as a function of wavelength and temperature ...	40
Fig.3-7. Refractive index of $\text{Al}_x\text{Ga}_{1-x}\text{As}$ obtained by equation (3-3) at 0.6328 μm and 700°C. Circles represent the data obtained by Kawai <i>et al.</i> [24]	42
Fig.4-1. Light propagation through the structure of QWIP <i>without</i> a grating	49
Fig.4-2. Light propagation through the structure of QWIP <i>with</i> a grating	50
Fig.4-3. Light propagation through the structure of C-QWIP with 45° oblique sidewalls.....	50
Fig.4-4. Definition of the parameters describing the geometry of a lamellar grating (after reference [26])	54
Fig.4-5. Schematic diagram of the grating-coupled quantum well infrared photodetector.....	62
Fig.4-6. Schematic diagram of the grating-coupled quantum well infrared photodetector with an AlAs layer	62
Fig.4-7. Schematic diagram of the proposed grating-coupled RCE-QWIP.....	63
Fig.4-8. Numerical and FDTD simulation results of quantum efficiency as a function of wavelength in the grating-coupled QWIP and the grating-coupled QWIP with an AlAs layer	66
Fig.4-9. Quantum efficiency as a function of wavelength in RCE-QWIP	66
Fig.4-10. Quantum efficiency degradation in terms of angle of incidence	68

Fig.4-11. Time to reach steady-state in three different cases; the grating-coupled QWIP, the grating-coupled QWIP with an AlAs layer, and the grating-coupled RCE-QWIP	69
Fig.5-1. Proposed schematic diagram of RCE-CQWIP.....	73
Fig.5-2. Quantum efficiency as a function of wavelength in C-QWIP structure	76
Fig.5-3. Quantum efficiency vs thickness of bottom GaAs layer.....	76
Fig.5-4. The comparison of quantum efficiency between C-QWIP and RCE-CQWIP structure.....	77
Fig.5-5. Dependence of angle of incidence for C-QWIP and RCE-CQWIP	77
Fig.5-6. Ray diagram of incident light at different angle in the C-QWIP structure	78
Fig.6-1. A regular assembly of thin parallel plates.....	81
Fig.6-2. Schematic diagram of a form birefringence layer.....	84
Fig.6-3. Phase retardation between TE- and TM- polarized light as a function of a normalized thickness rectangular-shaped grating of 50% duty cycle using second-order EMT	86
Fig.6-4. Phase retardation between TE- and TM- polarized light as a function of a rectangular-shaped grating duty cycle with $d/\lambda = 1.0$ and Λ/λ as a parameter using second-order EMT.....	87
Fig.6-5. Geometry of dielectric surface-relief grating	88
Fig.6-6. Simulated phase retardation as a function of wavelength using RCWA	93
Fig.6-7. Simulated TE and TM transmission as a function of wavelength using RCWA	93
Fig.6-8. Phase retardation between TE and TM polarized light as a function of a grating duty cycle.....	96

Fig.6-9. Phase retardation as a function of grating thickness	96
Fig.6-10. Phase retardation as a function of wavelength at $d = 2.2 \mu\text{m}$	97
Fig.6-11. Phase retardation as a function of angle of incidence at $d = 2.2 \mu\text{m}$	97
Fig.6-12. Schematic diagram of RCE-CQWIP using form birefringence technique	98
Fig.6-13. Quantum efficiency vs. thickness of epoxy	99
Fig.6-14. Quantum efficiency in terms of depth of a form birefringence layer.....	100
Fig.6-15. Quantum efficiency as a function of wavelength.....	101
Fig.6-16. The dependence of quantum efficiency on the angle of incidence	102
Fig.6-17. The diffraction efficiencies of the transmitted waves for a form birefringence layer.....	102

LIST OF TABLES

Table 3-1. Comparison of refractive index at room temperature and cryogenic temperature in terms of Al mole fraction calculated using equation (3-3).....41

LIST OF SYMBOLS

α_{p-r} = Absorption coefficient in p-region

η = Quantum efficiency

Λ = Grating period

F_f = Fill factor

F = Finess

ϵ = Dielectric constants

μ = Permeabilities

ϵ_r = Relative permittivity

σ = Conductivity

α_T = Thermal expansion coefficient

T_m = Material temperature

\Re = Reflected power

\Im = Transmitted power

δ_{ij} = Kronecker delta

\mathbf{p} = Dipole moment

\mathbf{e} = Polarization

W = Electronic transition

H' = Interaction Hamiltonian

$\Psi_h(z)$ = Hole envelope function

$\Psi_e(z)$ = Electron envelope function

$u_v(\mathbf{r})$ = Valence band atomic basis state

$u_c(\mathbf{r})$ = Conduction band atomic basis state

γ_h = Relative strength of transition

S_p^r = Scattering matrix elements

T^s = Overall transfer matrix

Γ = Intrinsic impedance

c_n^r = Channel mode amplitudes

LIST OF ABBREVIATIONS

ABCs: Absorbing Boundary Conditions

C - QWIP: Corrugated - Quantum Well Infrared Photodetector

CT: Cadmium Telluride

DBR: Distributed Bragg Reflector

EM: ElectroMagnetic

EMT: Effective Medium Theory

FDTD: Finite Difference Time Domain

MBE: Molecular Beam Epitaxy

MCT: Mercury Cadmium Telluride

MEM: Modal Expansion Method

MQW: Multi-Quantum Well

MSM: Metal - Semiconductor - Metal

NA: Numerical Aperture

PML: Perfectly Matched Layer

Q: Quality Factor

QE: Quantum Efficiency

QWIP: Quantum Well Infrared Photodetector

RCE - CQWIP: Resonant Cavity Enhanced - Corrugated Quantum Well Infrared

Photodetector

RCE: Resonant Cavity Enhanced

RCWA: Rigorous Coupled Wave Analysis

SMM: Scattering Matrix Method

SWE: Standing Wave Effect

TE: Transverse Electric

TIR: Total Internal Reflection

TM: Transverse Magnetic

TMM: Transfer Matrix Method

OVERVIEW OF DISSERTATION

Chapter	Overview	Contribution	
		Journal	Conference
1. Introduction	A novel RCE photodetector is studied in this dissertation that is expected to improve the quantum efficiency (QE). This can be achieved by utilizing a resonant cavity around the active region. The photons make multiple passes across the active region, improving the probability of absorption.	-	-
2. Review of related research	The related research is reviewed and some of the problems are introduced. As a solution to the problems, TMM and FDTD for the RCE structure are developed in term of the transfer matrix and finite difference, respectively.	- Optics Express (2004)	- GLPS (2004)
3. Determination of temperature-dependent refractive index of $\text{Al}_x\text{Ga}_{1-x}\text{As}$ material	The temperature-dependent Sellmeier equation for refractive index of $\text{Al}_x\text{Ga}_{1-x}\text{As}$ material is derived. This modified equation is useful especially when the structure is involved with temperature.	- Optics Letters (2006) ¹	- CLEO/Europe (2005)
4. Grating-coupled quantum well infrared photodetector (QWIP)	An analysis of quantum well infrared photodetector (QWIP) is presented. The proposed design of resonant cavity enhanced (RCE)-QWIP is also discussed as a promising device to enhance the QE. FDTD is used as a simulation tool. Near unity of QE is possible to achieve using RCE approach.	-	- Liquid Crystals in Optics & Photonics (2005)
5. Resonant cavity enhanced (RCE) corrugated quantum well infrared photodetectors (C-QWIP)	RCE-corrugated quantum well infrared photodetector (C-QWIP) is examined. FDTD simulation results show that 12% enhancement of QE over the standard C-QWIP can be achieved. Dependence of QE on the angle of incidence is also discussed.	-	- APS Joint Spring Meeting (2005)
6. RCE-CQWIP with a form birefringence layer	The RCE-CQWIP with a form birefringence layer is designed and simulated. Simulation results for the form birefringence layer and for the RCE-CQWIP are demonstrated using EMT/RCWA and the FDTD methods, respectively. FDTD simulation results show that QE of 68% with a form birefringence layer can be achieved using the novel design approach. Dependence of QE on the angle of incidence is also discussed.	- Applied Optics (2006) ²	- IEEE-nano (2006) ³
7. Conclusions	Enhancement of QE in general photodetector, QWIP, and C-QWIP using RCE approach is demonstrated.	-	-

1. Submitted for publication, 2. Accepted for publication, 3. Accepted for presentation.

* Other presentations: Ohio Optics Consortium (2003, 2004), Electro-Optics Student Seminar (2005), Great Lakes Photonics Symposium (GLPS-2006).

CHAPTER I

INTRODUCTION

Quantum efficiency (QE) is a key parameter in photodetectors that determines a variety of performance factors such as efficiency, noise and detectivity. The efficiency of conventional photodetectors is adversely affected by reflective losses, absorption outside the active regions, and transmission through the active region. In most cases, the photons only make a single pass across the active region. In order to increase efficiency, the active layer has to be made thicker, which increases the carrier transit time and reduces the detection speed. On the other hand, resonant cavity enhanced (RCE) photodetectors can have QE close to unity even for very thin active regions. This can be achieved by utilizing a resonant cavity around the active region. Photons make multiple passes across the thin active region, which improves the probability of absorption. The focus of this dissertation is to apply the RCE concept to novel detector structures to enhance their quantum efficiencies.

As a first step in this study, a finite difference time domain (FDTD) method and a transfer matrix method (TMM) has been developed to carry out a rigorous analysis of RCE structures. These are powerful tools for the analysis of most resonant cavity

structures. TMM is conducted at steady state, while FDTD can capture the transients in the device. As a result, FDTD was chosen as the simulation tool for the bulk of this research effort.

In order to carry out accurate simulations, it is important to know the refractive indices of the various layers in the device, including their temperature dependency. Thus, a temperature-dependent Sellmeier equation is derived to predict the accurate refractive index of materials used in photodetectors, especially the quantum well infrared photodetectors (QWIP) base on GaAs.

Both grating-coupled quantum well infrared photodetector (QWIP) and corrugated quantum well infrared photodetector (C-QWIP) are simulated using the FDTD method, and the results are compared with previously published results. Although these have been proven as viable infrared detectors, due to their low QE, they still lag behind mercury cadmium telluride (HgCdTe) detectors in market capture. Hence, the RCE approach is applied to the QWIP and C-QWIP devices to enhance their QE. These structures are referred to as RCE-QWIP and RCE-CQWIP, respectively.

This dissertation is organized as follows. In Section II, the prior research is reviewed and some of the current problems are introduced. As a solution to some of these problems, TMM and FDTD for the RCE structures are developed and numerical simulations are carried out. Then results of the TMM and FDTD are compared to the analysis done by Kishino *et al.* The temperature-dependent Sellmeier equation for refractive index is

derived in section III. This modified equation is useful especially when the structure is likely to undergo large temperature changes, as in the case with QWIP devices which are typically operated at cryogenic temperatures. In section IV, the analysis of quantum well infrared photodetector (QWIP) is presented. The proposed design of RCE-QWIP is also discussed as a promising device to enhance the QE. The proposed RCE-CQWIP is discussed in section V. Section VI is devoted to the analysis of RCE-CQWIP with a form birefringence layer, whose main purpose is to overcome the polarization selection rule of quantum well sub-band transitions. Finally, conclusions and recommendations for future work are given in section VII.

CHAPTER II

REVIEW OF RELATED RESEARCH

2.1 Introduction

In this chapter, the definition of quantum efficiency (QE) for standard photodetector and RCE photodetector is briefly reviewed. Due to the electromagnetic resonance in RCE photodetectors, they naturally exhibit a greater angular and wavelength sensitivity compared to non-RCE type detectors. Hence, the performance RCE photodetectors may be measured by its QE, and the numerical aperture (angle of acceptance). There have been several methods proposed to calculate these parameters. These methods are described and are compared with the approaches taken which are based on the transfer matrix method (TMM) and a finite difference time domain (FDTD). First, it is worth comparing the QE of a conventional photodetector with that of an RCE photodetector to explicitly quantify the benefit of using the RCE approach.

2.2 Quantum efficiency of photodetectors

QE is one of the key parameters used to characterize the performance of photodetectors. It is the fraction of optical power absorbed in the depletion region compared to the total power incident on the detector [1]. A distinction could be made between internal QE and external QE. The internal QE refers to the number of electron hole pairs generated per *absorbed* photon, while the external QE refers to the number of electron hole pairs generated per *incident* photon. The internal QE is a function of the quality of the semiconductor material and its growth conditions. Since the device designer has little control over this, the internal QE is often taken as a given. The external QE is affected by the structure of the device and how photons are transported to the active region. Since the latter is the focus of this dissertation, the generic term QE will be used to refer to the external QE, and it will be assumed that the internal QE is unity.

QE is directly proportional to detectivity, which can be written as

$$D^* = \frac{\sqrt{A\Delta f}}{NEP} = \frac{\eta q \lambda \sqrt{A\Delta f}}{h c i_{rms}} (cmHz^{1/2}W^{-1}) \quad (2-1)$$

where D^* is the detectivity (called D-star), A is the area, Δf is the effective noise bandwidth, NEP is the noise equivalent power, η is the QE, q is the charge of an electron, and i_{rms} is the RMS noise current. D^* is a commonly used figure of merit to quantify the noise and efficiency of a photodetectors in a single lumped parameter. Thus this relationship indicates that the higher the quantum efficiency, the better the performance of detector.

2.2.1 Conventional photodetectors

Fig. 2-1 shows the schematic diagram of conventional photodetector without a resonant cavity. As can be seen, reflection at the surface reduces the incident power by R , leaving $(1-R)P_0$ to enter the detector. The transmitted light must then pass through the p -region, whose absorption coefficient, α_{p-r} , is essentially identical to the bulk attenuation coefficient for the semiconductor material.

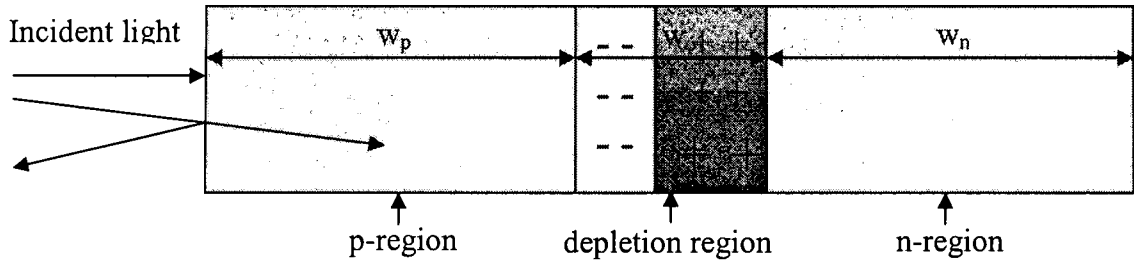


Fig. 2-1. Schematic diagram of a conventional junction photodetector (after reference [1]).

Thus, the amount of power reaching the active region is

$$p(w_p) = p_0(1 - R)e^{-\alpha_{p-r}w_p}, \quad (2-2)$$

The active region will absorb part of the light, reducing the power by $\exp(-\alpha w)$. The fraction of power absorbed by the active region is then $[1 - \exp(-\alpha w)]$. Combining all terms, we get an expression for the quantum efficiency

$$\eta = (1 - R)e^{-\alpha_{p-r}w_p}[1 - e^{-\alpha w}]. \quad (2-3)$$

Assuming that $R = 0.7$ and $\alpha w = 0.1$, then the QE is only 2.85 percent due to reflective loss, absorption in non-useful regions, and the absorption in the active region.

In practice, α_{p-r} ($\sim 5-10 \text{ cm}^{-1}$) can be ignored since it can be made negligible compared to α ($\sim 10^4 \text{ cm}^{-1}$) by utilizing a heterostructure with a higher bandgap for the p-side.

2.2.2 RCE photodetectors

Kishino *et al.* [2] presented an analytical formulation for the performance of RCE photodetectors in 1991, which is the basis of the description presented here. A generalized RCE photodetector structure is given in Fig. 2-2. In practice, the end mirrors are made of a number of dielectric layers, which are capable of providing the desired reflection through Bragg diffraction. The active layer, where absorption occurs, is placed between the two mirror structures and is defined by its thickness d and absorption coefficient, α . The separations between the active layer and the top and the bottom mirrors respectively are indicated by L_1 and L_2 .

The absorption coefficient outside the active region is denoted by α_{ex} . The field reflection coefficients of the top and the bottom mirrors are $r_1 e^{j\psi_1}$ and $r_2 e^{j\psi_2}$, respectively, where ψ_1 and ψ_2 denotes phase shifts due to the light penetration into the Bragg mirrors.

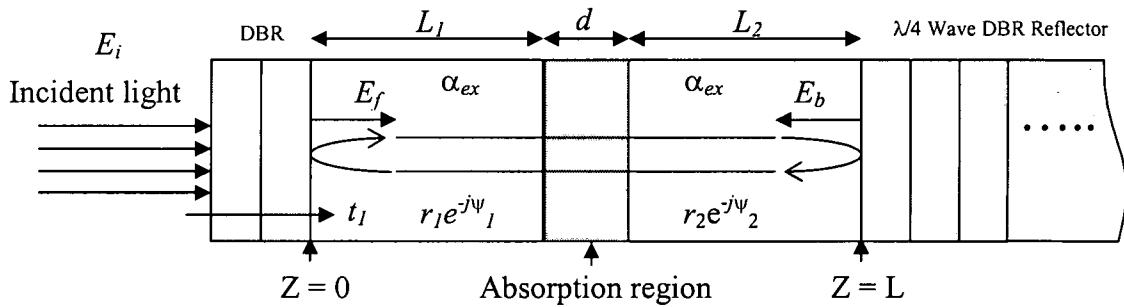


Fig. 2-2. Analytical model of a RCE photodetector (after reference [2]).

The transmitted component of the incident field component equals $t_1 \cdot E_i$. Inside the cavity, the forward traveling field E_f is composed of this transmitted field and the result of feedback from the internal mirrors. Therefore, E_f is the sum of the transmitted field and the feedback after a round trip in the cavity:

$$E_f = t_1 E_i + r_1 r_2 e^{-\alpha d - \alpha_{ex}(L_1 + L_2)} e^{-j(2\beta L + \psi_1 + \psi_2)} E_f \quad (2-4)$$

Solving for E_f gives

$$E_f = \frac{t_1}{1 - r_1 r_2 e^{-\alpha d - \alpha_{ex}(L_1 + L_2)} e^{-j(2\beta L + \psi_1 + \psi_2)}} E_i \quad (2-5)$$

The backward traveling wave is found by propagating E_f through the detector region:

$$E_b = r_2 e^{-\alpha d / 2} e^{-(\alpha_{ex} / 2)(L_1 + L_2)} e^{-j(\beta L + \psi_2)} E_f \quad (2-6)$$

The average circulating optical power inside the resonant cavity is given by

$$p_s = \frac{n}{2\eta_0} |E_s|^2 \quad (s = f \text{ or } b) \quad (2-7)$$

where η_0 and n are the vacuum characteristic impedance of electromagnetic waves and the refractive index of the detector material, respectively.

In this case, the light power absorbed in the active layer (P_l) can be obtained from the incident power P_i in the form:

$$\begin{aligned} p_l &= (p_f e^{-\alpha_{ex} L_1} + p_b e^{-\alpha_{ex} L_2}) (1 - e^{-\alpha d}) \\ &= \frac{(1 - r_1^2)(e^{-\alpha_{ex} L_1} + r_2^2 e^{-\alpha_{ex} L_2} e^{-\alpha_c L})(1 - e^{-\alpha d})}{1 - 2r_1 r_2 e^{-\alpha_c L} \cos(2\beta L + \psi_1 + \psi_2) + (r_1 r_2)^2 e^{-2\alpha_c L}} \times P_i \end{aligned} \quad (2-8)$$

Under the assumption that all the photo-generated carriers contribute to the detector current (i.e., internal quantum efficiency is 100%), η is the ratio of the absorbed power to the incident optical power, i. e., $\eta = P_l / P_i$.

Hence:

$$\eta = \left\{ \frac{(1 + R_2 e^{-\alpha d})}{1 - 2\sqrt{R_1 R_2} e^{-\alpha d} \cos(2\beta L + \psi_1 + \psi_2) + R_1 R_2 e^{-2\alpha d}} \right\} (1 - R_1)(1 - e^{-\alpha d}). \quad (2-9)$$

where $R_1 = r_1^2$, $R_2 = r_2^2$ and α_{ex} can be neglected because the material around the active layer can be designed to have very low absorption ($\alpha_{ex} \sim 5-10 \text{ cm}^{-1}$) compared to the active layer ($\alpha \sim 10^4 \text{ cm}^{-1}$) by using heterostructures.

It can be seen from equation (2-9) that η is a function of wavelength. The value of η peaks when the incident wavelength coincides with the cavity resonance wavelength. The peak η can be derived by imposing the resonant condition in the above equation, i. e., $2\beta L + \psi_1 + \psi_2 = 2m\pi$ ($m=1,2,3,\dots$).

$$\eta_{\max} = \left\{ \frac{(1 + R_2 e^{-\alpha d})}{(1 - \sqrt{R_1 R_2} e^{-\alpha d})^2} \right\} (1 - R_1)(1 - e^{-\alpha d}). \quad (2-10)$$

From these two equations, QE can be calculated as a function of the normalized absorption coefficient αd and incident wavelength λ_0 .

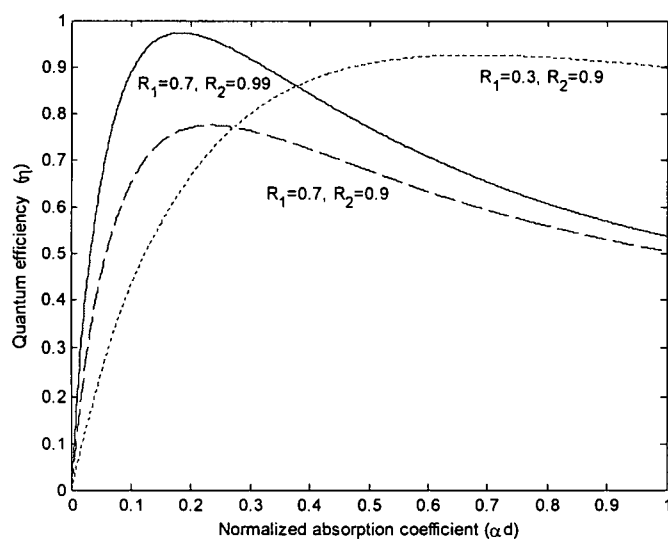


Fig. 2-3. Quantum efficiency as a function of the normalized absorption coefficient for $\lambda = 900\text{nm}$ at different values of R_1 and R_2 (equation (2-10)).

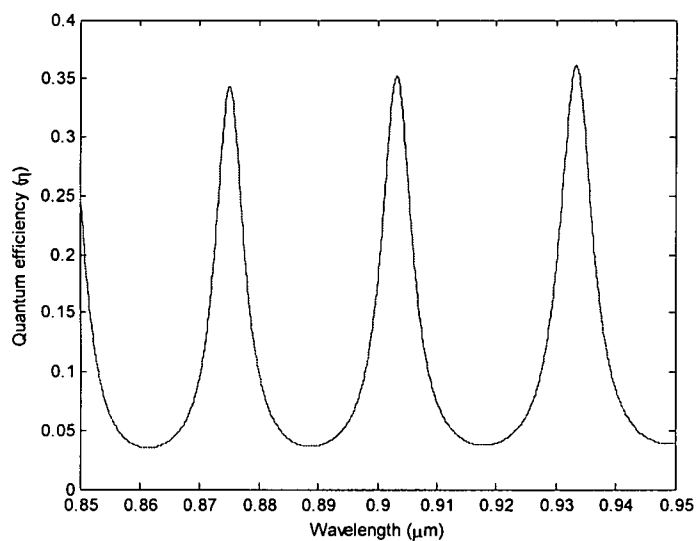


Fig. 2-4. Wavelength dependence of quantum efficiency of RCE detectors for $R_1 = 0.3$ and $R_2 = 0.99$ (equation (2-9)).

Fig. 2-3 represents the maximum QE in terms of the normalized absorption coefficient αd at different values of R_1 and R_2 . It can be seen that the highest QE can be achieved when R_1 and R_2 are 0.7 and 0.99, respectively. The wavelength dependence of QE for $R_1 = 0.3$ and $R_2 = 0.99$ is shown in Fig. 2-4.

In the analysis of Kishino *et al* [2], they made assumption ignoring the standing wave effect (SWE), which it will be distinguished as the confinement factor effect, and treated the SWE separately. Many of the papers [3-6] published since 1991 cite the formula directly and treated the SWE separately. SWE and the resonance are in fact inseparable. Treating them separately has resulted in much confusion in its understanding. In addition, the prior treatment also ignores the reflection at the various interfaces within the RCE structure, except at the top and bottom reflectors.

Here is an example considering the standing wave effect in an MSM (metal-semiconductor-metal) RCE photodetector (see Figs. 2-5, 2-6). Notice that these graphs are depicted as a function of channel thickness, which corresponds to the thickness of active layer. Although analysis of MSM RCE photodetector is a more precise method than the former treatment in Ref [2], it still does not consider the refractive index variation across all the layers. This may be a minor effect, as the refractive index difference between the layers is quite small. However, a self-consistent method that includes the reflection at all boundaries is important for studying the effects of one-dimensional and two-dimensional grating structures.

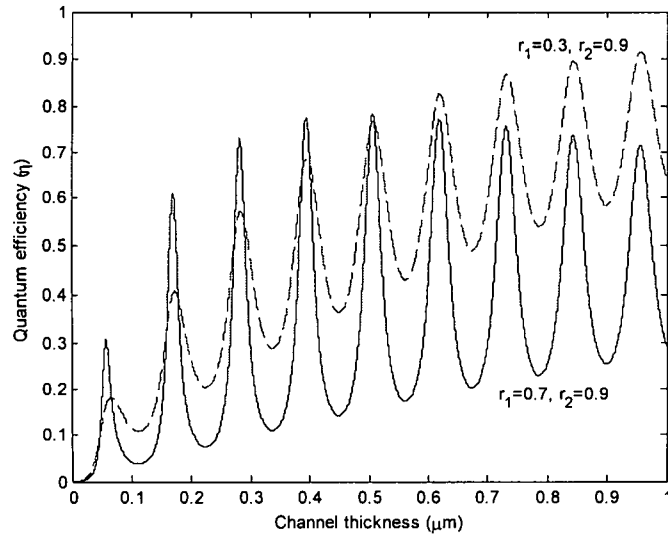


Fig. 2-5. Quantum efficiency versus channel thickness dependence for $\lambda_1 = 820\text{nm}$ for reflectivities $r_1 = 0.7$ and $r_1 = 0.3$ (after reference [4]).

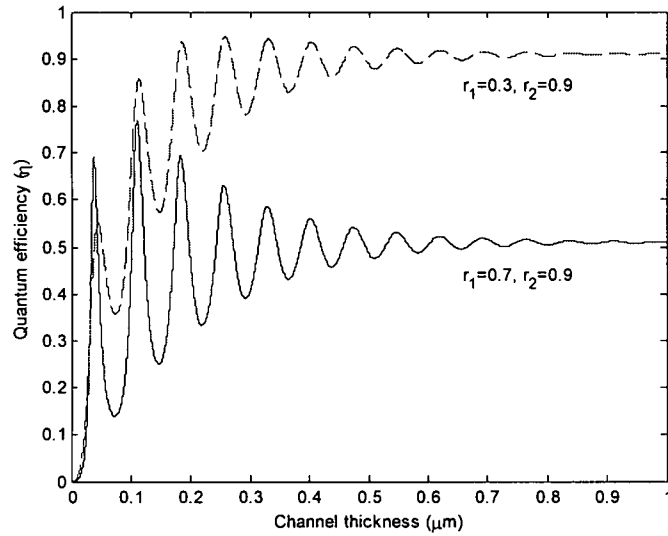


Fig. 2-6. Quantum efficiency versus channel thickness dependence for $\lambda_2 = 532\text{nm}$ and for reflectivities $r_1 = 0.7$ and $r_1 = 0.3$ (after reference [4]).

For this purpose, the transfer matrix method (TMM) [7] for the rigorous analysis of RCE structure has been developed. The TMM is a flexible, versatile and accurate method for the analysis of periodic structure such as RCE photodetectors and it is also useful for studying the standing wave effect and the refractive index changes across boundaries. As a comparative technique, the FDTD method is also developed, and the results are discussed in terms of not only accuracy and scope of validity but also simplicity and insightfulness. Compared to the analytical model presented in [2] (hereafter referred to as the analytical model), these methods lead to qualitatively similar but more accurate and insightful results. The FDTD approach is an efficient way to visualize how the field inside the cavity propagates and builds in intensity as a function of time and space.

2.3 Angle dependence of quantum efficiency

All the analysis done so far is based on normal incidence. This can be easily expanded to the general case by replacing β with $\beta \cos \theta$ in the equations. Here, θ is related to the angle of incidence θ_i by Snell's law, $n \sin \theta = \sin \theta_i$. The resonant wavelength will also become shifted, since the optical path lengths increase with θ . The new resonance wavelength condition becomes $2\beta L \cos \theta + \psi_1(\theta) + \psi_2(\theta) = 2m\pi$. At small θ_i , the wavelength shift $\Delta\lambda$ can be approximated as [8]:

$$|\Delta\lambda| \sim \frac{1}{2} \left(\frac{\theta_i}{n} \right)^2 \lambda, \quad (2-11)$$

Returning to the normal incidence case (2-9) and inserting the angular dependence of η as a function of F , λ , L , n_{eff} , and n gives

$$\frac{\Delta\eta}{\eta} = \frac{\eta_p - \eta}{\eta} = \left[\frac{2n_{eff}(L + L_{eff,1} + L_{eff,2})}{\lambda} F \left(\frac{\theta_i}{n} \right)^2 \right]^2. \quad (2-12)$$

where $L_{eff,i}$ are the effective optical lengths of the mirrors, n_{eff} is the effective refractive index, and F is the finesse, which measures the wavelength selectivity of the cavity.

Equation (2-12) indicates that η is most sensitive to the angle of incidence in a high F cavity at shorter λ . In the general case, the angular dependence of the detector performance is not so large to present significant alignment difficulties. We will demonstrate this for RCE using our TMM formulation. Below 5° , η degrades by less than 1%, even for a very high F cavity at $1 \mu\text{m}$. For lower F and longer λ , the angular constraints can be relaxed while maintaining the benefits of RCE (Fig. 2-7). However, the angle dependence of η can be a significant problem for very small area RCE photodetectors, in which case a large NA (numerical aperture) optical coupling lens or objective is required.

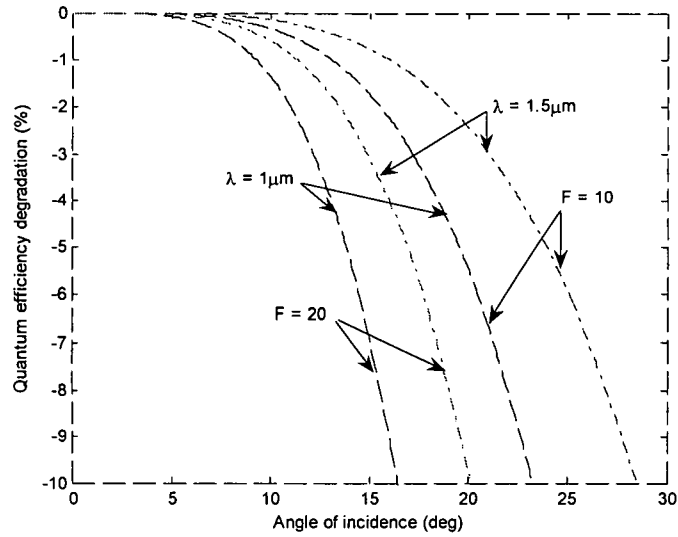


Fig. 2-7. Degradation of η for off-angle incidence at $\lambda = 1.0$ and $1.5 \mu\text{m}$ for $F = 10$ and 20 (equation (2-12)).

2.4 Transfer Matrix Method (TMM)

The transfer matrix method (TMM) is a powerful tool for the analysis of periodic structures. The TMM has been used to represent the solution of the coupled mode equations by a 2×2 transfer matrix, which relates the forward-and backward-propagating field amplitudes [9]. Periodic and aperiodic structures can be analyzed effectively by this method. The grating structure is divided into a number of uniform layers, which have an analytic transfer matrix. The transfer matrix for the entire structure can be obtained by multiplying the individual transfer matrices together [10]. It should be noted that this method is simply a numerical method for solving the coupled mode equations. However, unlike the coupled mode equations, TMM can be handle large index differences across

the interfaces, and the structure does not have to be periodic. In this section, the TMM and its application to RCE grating-assisted photodetectors are discussed.

2.4.1 Formulation of the quantum efficiency for RCE photodetectors using TMM

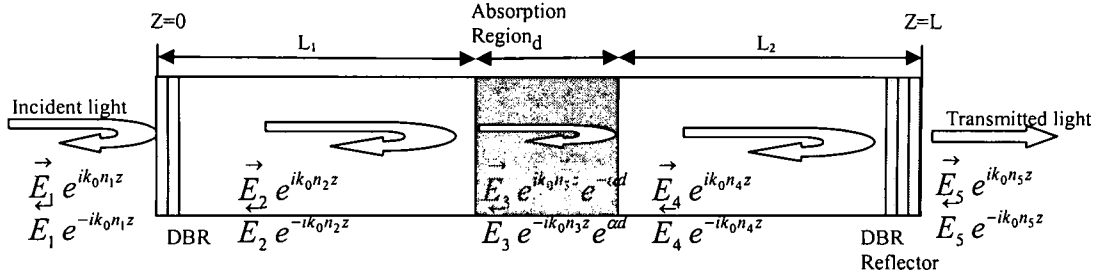


Fig. 2-8. Analytical model of a RCE photodetector using TMM

As shown in the above figure, the structures consists of the propagation element and interface elements. The direction of propagation is assumed to be the z-axis. For simplicity only the TE modes are considered in this analysis. Since the electric field at every point is a superposition of forward and backward propagating waves,,

$$E(z) = \vec{E}_m e^{jk_0(n'_m + n''_m)z} + \vec{E}_m e^{-jk_0(n'_m + n''_m)z} \quad (2-13)$$

where \vec{E}_m and \vec{E}_m denotes the electrical field traveling to the right and left, respectively.

The variables \vec{E}_m and \vec{E}_m represent the values of the wave amplitudes at the input of the m th layer. The wave amplitudes at the output are \vec{E}_m and \vec{E}_m . In a practical detector

design, the layers surrounding the active layer can be designed to have very low absorption by using heterostructures. Therefore the input and output can be related as:

$$\begin{bmatrix} \vec{E}_m' \\ \vec{E}_m' \end{bmatrix} = \begin{bmatrix} e^{jk_o n z} & 0 \\ 0 & e^{-jk_o n z} \end{bmatrix} \begin{bmatrix} \vec{E}_m \\ \vec{E}_m \end{bmatrix} = M \begin{bmatrix} \vec{E}_m \\ \vec{E}_m \end{bmatrix} \quad (2-14)$$

When the detectors are illuminated at normal incidence, the discontinuous boundary condition yields another transfer matrix of the form

$$\begin{bmatrix} \vec{E}_{m+1}' \\ \vec{E}_{m+1}' \end{bmatrix} = \begin{bmatrix} \frac{1}{t_m} & \frac{r_m}{t_m} \\ \frac{r_m}{t_m} & \frac{1}{t_m} \end{bmatrix} \begin{bmatrix} \vec{E}_m' \\ \vec{E}_m' \end{bmatrix} = N \begin{bmatrix} \vec{E}_m' \\ \vec{E}_m' \end{bmatrix} \quad (2-15)$$

where r_m and t_m are the reflection and transmission coefficients at the interface between the $(m-1)$ th layer and the m th layer. These reflection and transmission coefficients are defined as follows in the case of TE modes.

$$r_m = \frac{n_m - n_{m-1}}{n_m + n_{m-1}} \quad t_m = \frac{2n_m}{n_m + n_{m-1}} \quad (2-16)$$

The total transfer matrix of the whole structure can be expressed by simple matrix multiplication in the order as shown below

$$\begin{bmatrix} \vec{E}_{out}' \\ \vec{E}_{out}' \end{bmatrix} = N_n \times M_{n-1} \times N_{n-1} \times M_{n-2} \times \cdots \times N_1 \times M_1 \begin{bmatrix} \vec{E}_{in}' \\ \vec{E}_{in}' \end{bmatrix} \quad (2-17)$$

$$\begin{bmatrix} \vec{E}_{out} \\ \vec{E}_{out} \end{bmatrix} = \begin{bmatrix} T_{11} & T_{12} \\ T_{21} & T_{22} \end{bmatrix} \begin{bmatrix} \vec{E}_{in} \\ \vec{E}_{in} \end{bmatrix} = T \begin{bmatrix} \vec{E}_{in} \\ \vec{E}_{in} \end{bmatrix} \quad (2-18)$$

The reflectance and transmission under normal incidence are given by [11]

$$\mathfrak{R} = \left| \frac{\vec{E}_{in}^{\leftarrow}}{\vec{E}_{in}^{\rightarrow}} \right|^2, \quad \mathfrak{T} = \frac{n_{out}}{n_{in}} \left| \frac{\vec{E}_{out}^{\rightarrow}}{\vec{E}_{in}^{\rightarrow}} \right|^2 \quad (2-19)$$

It is also required that electric field from the exit side $\vec{E}_{out}^{\leftarrow}$ must vanish since no power is injected from the opposite side. Thus equation (2-18) becomes

$$\begin{bmatrix} \vec{E}_{out} \\ 0 \end{bmatrix} = \begin{bmatrix} T_{11} & T_{12} \\ T_{21} & T_{22} \end{bmatrix} \begin{bmatrix} \vec{E}_{in} \\ \vec{E}_{in} \end{bmatrix} \quad (2-20)$$

After simple mathematical manipulation, the reflectance and transmission can be written in terms of the matrix:

$$\mathfrak{R} = \left| \frac{T_{21}}{T_{22}} \right|^2, \quad \mathfrak{T} = \frac{n_{out}}{n_{in}} \left| \frac{T_{11}T_{22} - T_{12}T_{21}}{T_{22}} \right|^2 \quad (2-21)$$

The external quantum efficiency of the detector is the ratio of photon absorption that results in a photocurrent compared to the incident photons. The internal quantum efficiency will be assumed to be 100%. If we assume only the active layer absorbs light, the external quantum efficiency can be written as [12]

$$\eta = 1 - \mathfrak{R} - \mathfrak{T} \quad (2-22)$$

where \mathfrak{R} and \mathfrak{T} are the reflected and transmitted powers, respectively. Since \mathfrak{R} and \mathfrak{T} contain information about the entire RCE structure, including the active region and DBR layers, this expression can be used for predicting the performance of the detector.

2.4.2 Results and discussion

Once the all parameters are known, the QE can be easily calculated as a function of normalized absorption coefficient αd using TMM. As mentioned before, the QE has an oscillatory nature due to optical interference inside the cavity [13]. Fig. 2-9 shows QE versus normalized absorption coefficient αd at the resonant wavelengths. The analysis of Kishino *et al.* is compared with this approach to verify that the results are generally consistent with the former treatment, except for the oscillatory nature of the curve. It is believed that confinement factor governs the absorption in the active region and it affects QE as the thickness of absorption region changes. Besides, the small difference between the two curves arises due to the reflection to meet the boundary condition at each layer. Wavelength dependence of QE for RCE detectors is depicted in Fig. 2-10. It is almost identical to Fig. 2-4, which validates the transfer matrix approach.

The analysis for the RCE MSM photodetector is plotted in Figs. 2-11, -12. These results are also consistent with the analysis derived by Gvozdic *et al.* [13]. Therefore, TMM can be confidently used for analyzing periodic and aperiodic RCE photodetector structures.

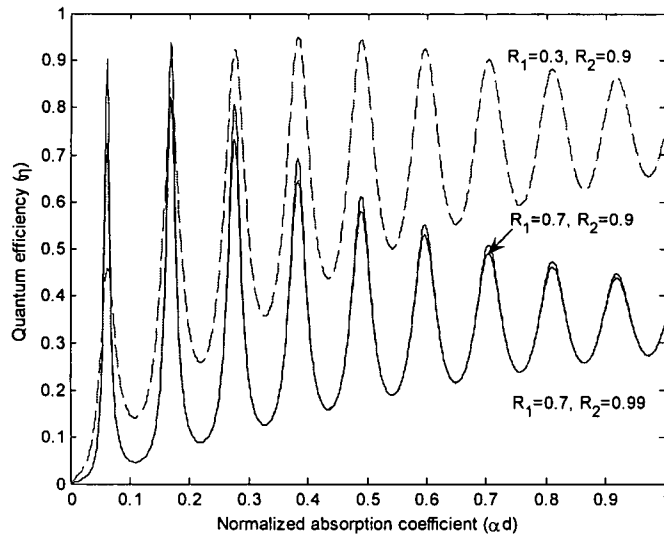


Fig. 2-9. Calculated quantum efficiency as a function of the normalized absorption coefficient for $\lambda = 900\text{nm}$ at different values of R_1 and R_2 using TMM.

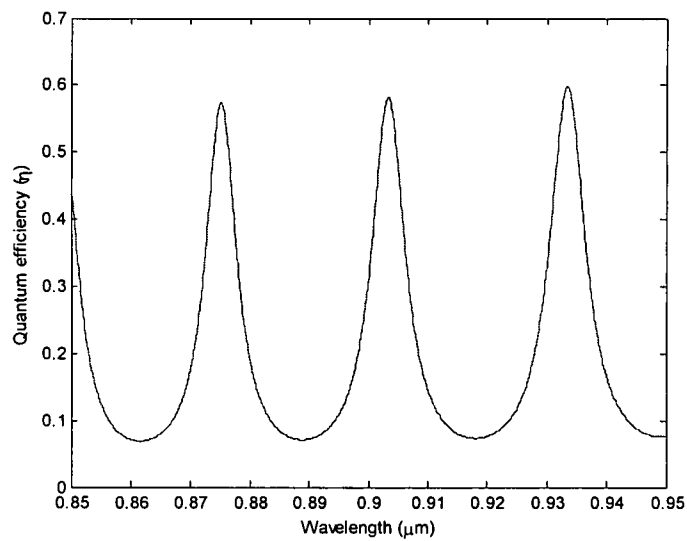


Fig. 2-10. Wavelength dependence of quantum efficiency for RCE detectors for $R_1 = 0.3$ and $R_2 = 0.99$ using TMM

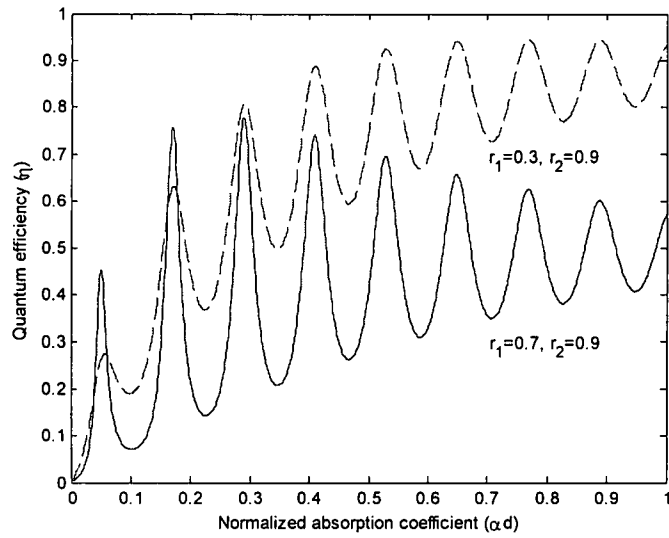


Fig. 2-11. Quantum efficiency versus channel thickness dependence for $\lambda_1 = 820\text{nm}$ and for reflectivities $r_1 = 0.7$ and $r_1 = 0.3$ by using TMM.

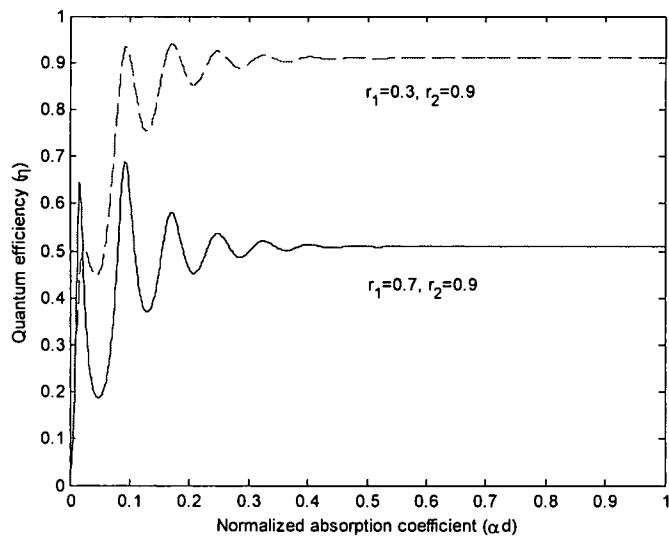


Fig. 2-12. Quantum efficiency versus channel thickness dependence for $\lambda_2 = 532\text{nm}$ and for reflectivities $r_1 = 0.7$ and $r_1 = 0.3$ by using TMM.

The dependence of QE on incident angle is shown in Fig. 2-13. Below 5°, η degrades by less than 1% at a wavelength of 1 μm . This result is also consistent with the expression derived by Kishino *et al.* [2] in the limiting case of small angles of incidence. As described before, some differences arise at large incidence angles due to the reflection at each boundary.

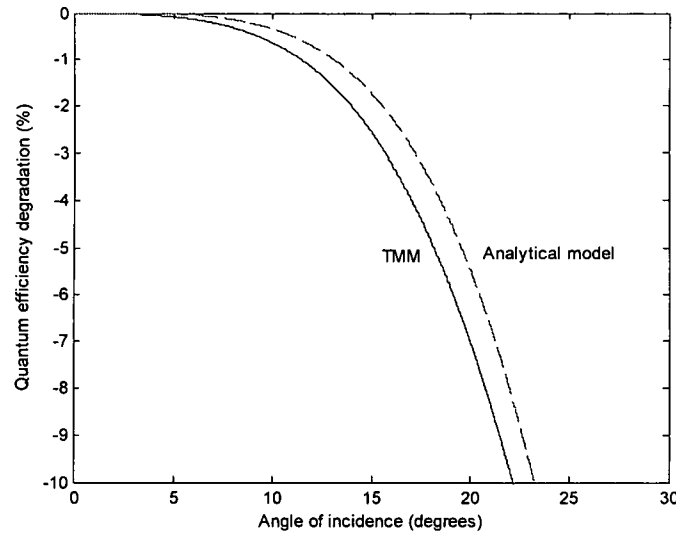


Fig. 2-13. Dependence of QE on incident angle at wavelength of 1 μm for $F=10$. Dashed line shows efficiency decrease $\Delta\eta/\eta$ derived by Kishino *et al.*[2] and solid line represents $\Delta\eta/\eta$ using TMM.

2.5 Finite Difference Time Domain (FDTD)

2.5.1 Formulation of the FDTD method

FDTD is a fully-numerical technique that has the least number of approximations compared to any other simulation technique in photonics. In free space, the time-

dependent Maxwell's curl equations can be written in term of E and H in three dimensions. For simplicity, a one-dimensional problem with electric and magnetic field components, E_x and H_y , propagating along the z -direction will be considered through a RCE structure shown in Fig. 2-8. Since this structure contains an absorptive region, the Maxwell's curl equations in a more general form should be used, by including the conductivity to represent the loss term such as:

$$\epsilon_r \epsilon_0 \frac{\partial E}{\partial t} = \nabla \times H - J \quad (2-23)$$

$$\frac{\partial H}{\partial t} = -\frac{1}{\mu_0} \nabla \times E. \quad (2-24)$$

where $J_x = \sigma E_x$. Here ϵ_r and σ denote the relative permittivity and the conductivity, respectively. Taking the finite differences for both the temporal and spatial derivatives, the above equations can be expressed as [14]

$$E_x^{n+1/2}(i) = \left[\frac{1 - \frac{\sigma \Delta t}{2\epsilon_r \epsilon_0}}{1 + \frac{\sigma \Delta t}{2\epsilon_r \epsilon_0}} \right] E_x^{n-1/2}(i) - \left[\frac{\frac{\Delta t}{\epsilon_r \epsilon_0 \Delta z}}{1 + \frac{\sigma \Delta t}{2\epsilon_r \epsilon_0}} \right] [H_y^n(i+1/2) - H_y^n(i-1/2)], \quad (2-25)$$

$$H_y^{n+1}(i+1/2) = H_y^n(i+1/2) - \frac{\Delta t}{\mu_0 \Delta z} [E_x^{n+1/2}(i+1) - E_x^{n+1/2}(i)], \quad (2-26)$$

In these equations, n in the superscripts actually means a time $t = \Delta t \cdot n$. And i in parentheses represent distance $z = \Delta z \cdot i$. In order to consider the conductivity, which contributes the absorption, we use the following relationship [15]:

$$\alpha = \frac{\omega}{c_0} \sqrt{\frac{\epsilon_r}{2}} \left[\sqrt{1 + \left(\frac{\sigma}{\omega \epsilon_0 \epsilon_r} \right)^2} - 1 \right]^{1/2} (Np/m). \quad (2-27)$$

2.5.2 Results and discussion

2.5.2.1 Optical field distribution in GaAs/ $\text{In}_{0.2}\text{Ga}_{0.8}\text{As}$ detector

The FDTD method can be used to obtain the optical field distribution in a RCE photodetector as a function of time without deriving any extra formulae. Figs. 2-14, -15 show the cavity field distribution in the case with no absorption and in the case with absorption, respectively, at a wavelength of $0.9\ \mu\text{m}$. There is a great deal of field enhancement inside the resonant cavity in case (2-14) while the enhancement is weaker in case (2-15). In this simulation, the active region was assumed to be $\text{In}_{0.2}\text{Ga}_{0.8}\text{As}$ and the surrounding layer was assumed to be GaAs. The indices of these regions are 3.5 and 3.52, respectively. The top and bottom mirrors are AlAs/GaAs DBR stacks designed for $0.9\ \mu\text{m}$. The index of refraction of AlAs and GaAs are 2.97 and 3.5, respectively.

Fig. 2-16 shows the energy distribution inside the cavity as a function of time. It can be seen that the steady-state condition is reached at around $540\ \text{fs}$. This build-up time is an important factor in RCE photodetectors designed for high-speed operations. Although $540\ \text{fs}$ corresponds to the THz region of operation, in practice, carrier lifetimes will limit the speed of operation to the GHz range. Nevertheless, unlike the standard photodetectors, which have extremely small photon lifetimes, RCE detectors have an upper limit to their frequency of operation determined by the cavity build-up time. Thus far in the literature,

the time required to build the optical field inside the cavity to steady state has been calculated using a simple cavity model as [8]

$$\tau_p = \frac{\tau_{RT}}{Loss}. \quad (2-28)$$

where τ_{RT} is the time required for photons to make one round-trip in the optical cavity, and $Loss$ is the total decay during this trip. For this structure, the cavity length of $2 \mu\text{m}$ results in $\tau_{RT} \approx 48 \text{ fs}$ and $Loss \approx 0.53$ using typical parameters. Hence the photon lifetime becomes 90 fs . This lifetime is significantly smaller than the 540 fs obtained from FDTD. This is mainly due to the fact that equation (2-28) does not consider the propagation time through the DBR stacks. Equation (2-28) treats the DBR stacks as a single reflector with lumped phase shifts at either end. An analytical formulation for the field build-up inside a distributed structure is not trivial which the FDTD is able to handle quite easily and accurately.

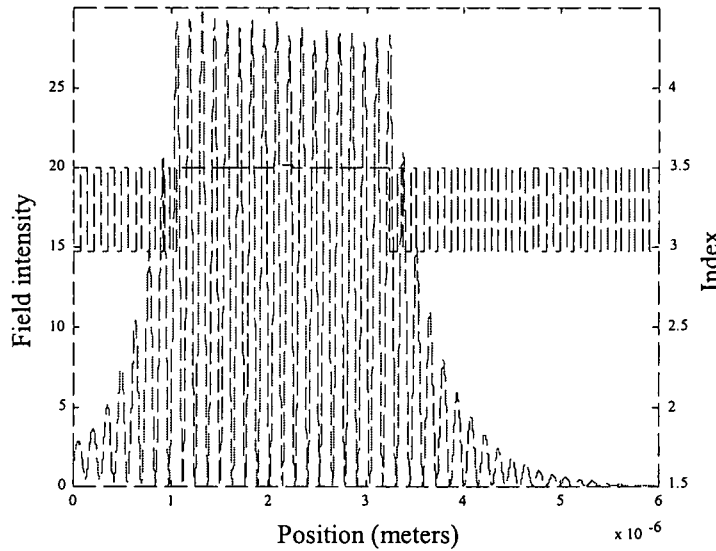


Fig. 2-14. Optical field distribution in a RCE photodetector with no absorption.

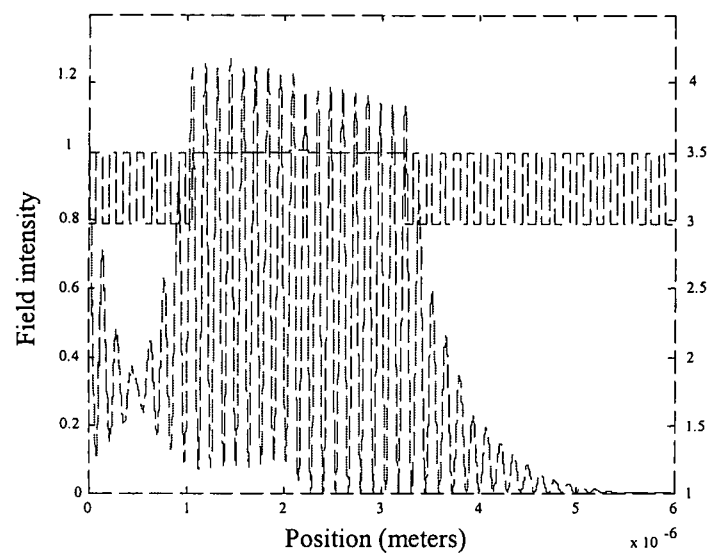


Fig. 2-15. Optical field distribution in a RCE photodetector. with absorption.

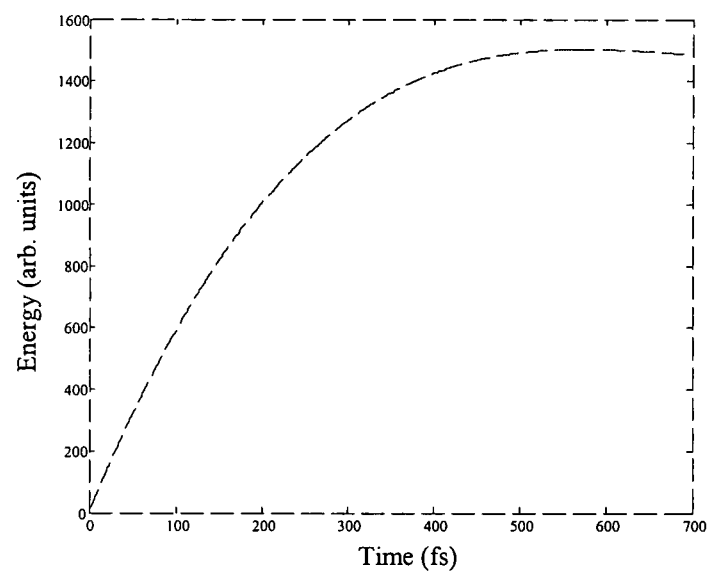


Fig. 2-16. The energy distribution inside the cavity as a function of time with absorption.
The steady-state condition is reached at 540 fs.

2.5.2.2 Quantum efficiency in GaAs/In_{0.2}Ga_{0.8}As detector

Kishino *et al.* [2] presented a detailed analysis showing a near unity QE in a RCE photodetector. In their derivation, the standing wave effect was accounted for as an after-the-fact effect to include the interference between the forward and backward waves. The power absorbed in the absorption region (P_l) was shown to be related to the incident power P_i as shown in equation (2-8), where P_f and P_b are forward and backward traveling wave respectively inside the structure. The absorption region is defined by an absorption coefficient (α) and thickness (d). L_1 and L_2 refer to the separations between the absorption region and the top and bottom mirrors respectively. The absorption coefficient of the material around the absorption region is expressed as α_{ex} . With these assumptions, they were able to produce a simple equation at the resonant condition, i.e., $2\beta L + \Psi_1 + \Psi_2 = 2m\pi$ ($m = 1, 2, 3\dots$). However, this treatment is not self-consistent because they accounted for the standing wave effect later in a phenomenological way.

An alternative way would be to calculate the total electric field first and then interpret the absorbed power from the field distribution. This approach will ensure that the standing wave effect is included self-consistently without introducing it afterwards.

Another important aspect is that the analytical formulae ignored the distributed nature of the refractive index changes across each layer. The amplitude and phase of the DBR reflector was lumped into a single parameter such as R_1 and R_2 . In practice, the index of

refraction of the absorption region is different from the index of refraction of the surrounding regions. Even though this may be a small difference, it is still desirable to include this for self-consistency, especially for a numerical implementation. In addition, the amplitude and phase of the reflection from the DBR stacks are a function of wavelength, which is not accounted for in the analytical model. One of the advantages of the FDTD method is that the device does not have to conform to an analytically describable structure. It is simple to develop but powerful for almost any configuration. It should be pointed out that a one-dimensional FDTD is not nearly as time-consuming or CPU-intensive as their three-dimensional counter-parts, and is ideally suited for the analysis of simple RCE structures.

The FDTD simulation results are now compared with the analytical model and the transfer matrix method shown in preceding section. Most of the results from the FDTD are consistent with the analytical model except for the oscillations shown in Fig. 2-20. Notice that the FDTD and the TMM results agree almost exactly for the QE. This difference between the analytical model and the FDTD arises from the standing wave effect. It should be noted that we have a different maximum QE compared to the analytical model at the same normalized absorption coefficient in both cases. For instance, one can achieve less than 20% QE when the normalized absorption coefficient is 0.17 while the analytical model predicts more than 90% as in Fig. 2-17. This clearly demonstrates that one has to be careful in choosing the optimum thickness in order to get maximum QE for a given structure.

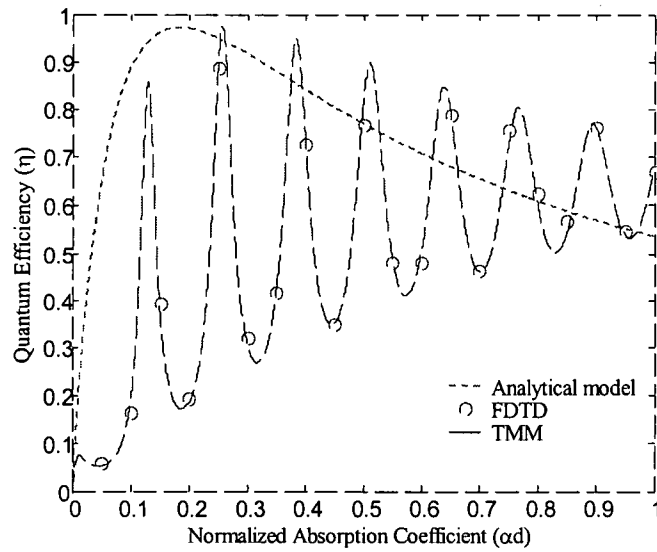


Fig. 2-17. Calculated η as a function of the normalized absorption coefficient. Dashed line shows η , derived by analytical model, and circle and solid line represent η , using FDTD and TMM, respectively.

In addition, the small difference in the envelope in Fig. 2-17 is attributed to the refractive index change between the absorption and the surrounding regions, which the FDTD and the TMM can capture quite accurately. Comparing the three different simulations, it can be concluded that the refractive index of each layer mainly determines the local maxima position of the envelope, that is, it shifts the curve slightly.

2.5.2.3 MCT detector using FDTD method

In the preceding section, the optical distribution and QE in GaAs/ $\text{In}_{0.2}\text{Ga}_{0.8}\text{As}$ -based detector were discussed. In this section another implementation using the RCE approach on Mercury Cadmium Telluride (MCT)-based detector is presented. Fig. 2-18 shows the schematic diagram for MCT with DBR stacks on both sides.

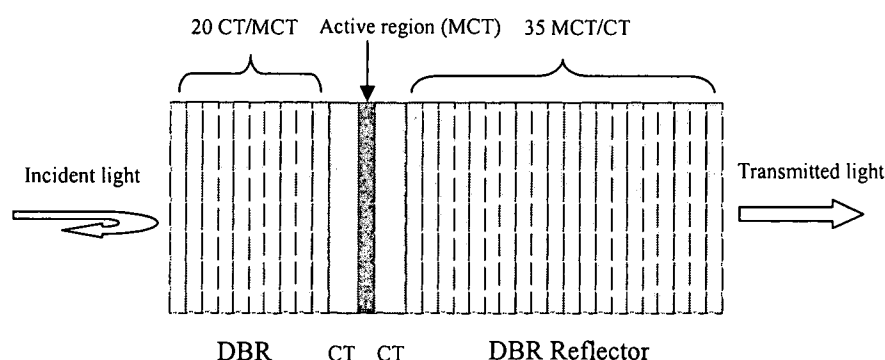


Fig. 2-18. Schematic diagram of RCE-HgCdTe detector

Again, the FDTD method is used to obtain the optical field distribution in this cavity. Fig. 2-19 shows the position dependent cavity field distribution with absorption at a wavelength of $4\text{ }\mu\text{m}$. In this simulation, cadmium telluride (CT) for the surrounding regions and MCT for the absorption region has been used. The indices of these regions are 2.681 and 3.2095, respectively. The top and bottom mirrors are MCT/CT DBR stacks designed for $4\text{ }\mu\text{m}$. The index of refraction of MCT and CT are 2.9224 and 2.681, respectively. Fig. 2-20 shows the energy distribution inside the cavity as a function of time. It can be seen that the steady-state condition is reached at around 5300 fs . Unlike the previous case, it takes a much longer time to reach the steady-state condition due to the fact that actual size of the structure is larger than the previous GaAs/ $\text{In}_{0.2}\text{Ga}_{0.8}\text{As}$ detector. Furthermore, since this device operates at $\lambda = 4\text{ }\mu\text{m}$, each layer of the DBR stacks are thicker to meet the resonant cavity condition, which is $d = \lambda / (4n)$.

The simulation of this MCT structure was conducted in collaboration with Prof. Ghosh's group at University of Illinois at Chicago. The purpose was to improve the operating

temperature of the RCE-MCT detector partly from increasing the QE. In general, MCT detectors operate at about 77 °K.

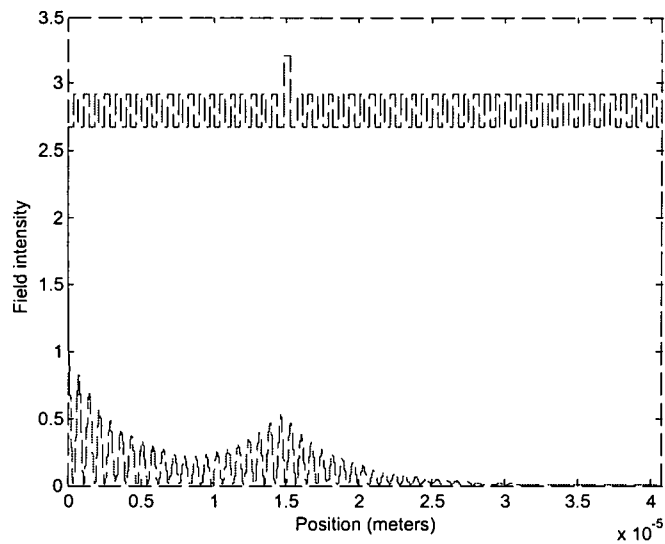


Fig. 2-19. Optical field distribution in a RCE-MCT photodetector. with absorption.

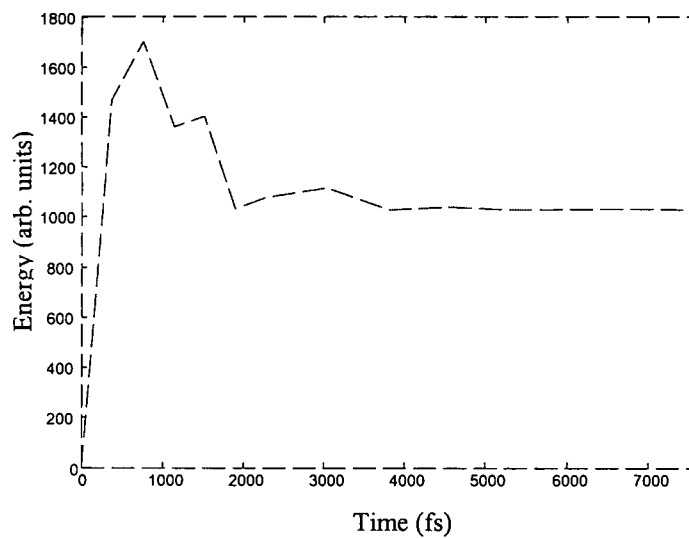


Fig. 2-20. The energy distribution inside the cavity as a function of time with absorption.

2.6 Conclusion

In this chapter, a review of related research is presented, and the minor difficulties in interpretation due to some inconsistencies in the formulations are discussed. So the analysis tools such as FDTD and TMM have been developed to capture the all missing considerations, for instance SWE and refractive index across the layer, in order to analyze these structures more rigorously.

The FDTD and TMM are demonstrated to be excellent tools since these methods lead to comparatively similar but more accurate and insightful results. Besides, FDTD approach, especially the one-dimensional model, is an efficient way to visualize how the field inside the cavity propagates and builds in intensity as a function of time and space.

Based on these analyses, the FDTD method is finally selected as the primary simulation tool for the work described in the following chapters.

CHAPTER III

DETERMINATION OF TEMPERATURE-DEPENDENT REFRACTIVE INDEX OF $\text{Al}_x\text{Ga}_{1-x}\text{As}$ MATERIAL

3.1 Introduction

The refractive index n is one of the most important parameters in the design of waveguides, modulators, detectors and lasers. The empirical Sellmeier equation is the most often-used model for predicting the refractive index as a function of wavelength. Its main advantage is that it is convenient and simple to use. However, it is only valid at room temperature. There are several instances when a temperature-dependent Sellmeier equation would be desirable, especially in structures that undergo large temperature changes [16-20].

In this chapter, a temperature-dependent Sellmeier equation for $\text{Al}_x\text{Ga}_{1-x}\text{As}$ is presented. $\text{Al}_x\text{Ga}_{1-x}\text{As}$ is a ternary alloy that is lattice matched to GaAs over the entire composition range, and as a result, it is the most common alloy used in semiconductor optoelectronic devices. By varying the aluminum mole fraction x , one can optimize the refractive index profiles for a variety of design purposes. Not only does aluminum mole fraction change

the refractive index, but temperature also plays an important role. Thus, it would be very useful to model the refractive index of $\text{Al}_x\text{Ga}_{1-x}\text{As}$ as a function of temperature. This would be useful for in-situ monitoring of the refractive index of materials while they are being grown in a molecular beam epitaxy (MBE) chamber. It is also important to know this behavior in photodetectors such as QWIP or C-QWIP structures because they typically operate at cryogenic temperatures.

Hence, an empirical Sellmeier equation for $\text{Al}_x\text{Ga}_{1-x}\text{As}$ has been used to model the experimental data. The results enable one to calculate the index dispersion for $\text{Al}_x\text{Ga}_{1-x}\text{As}$ alloys as a function of composition x , wavelength and temperature.

3.2 Experimental setup

Layer composition of the experimental sample is depicted in Fig. 3-1. It consists of 18 pairs of GaAs/AlAs in the top DBR stack and 22 pairs of GaAs/AlAs in the bottom DBR stack to achieve the resonant structure. Maximum field enhancement occurs inside the cavity when the incident field meets the resonance condition. Although this is not strictly a photodetector structure, the only difference is the electronic bandgap of the cavity region. It can be turned into an RCE photodetector by replacing the GaAs layer in the cavity with a lower bandgap InGaAs layer to induce optical absorption.

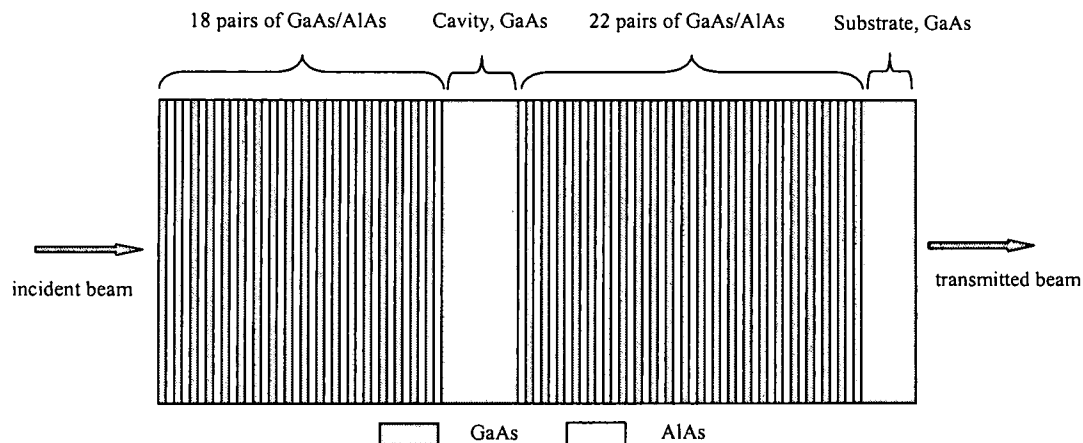


Fig. 3-1. Longitudinal schematic diagram of experimental sample.

A 1550 nm tunable diode laser source (Agilent 8164A) and a germanium photodetector model FDG05 for detecting the transmitted beam were used in this experiment. The sample is mounted on the thermocouple and the temperature is controlled by an Omega-CN7600 controller. The data from the detector is analyzed by a Tektronix TDS 620B spectrometer to get the transmission spectra. The actual experimental setup is shown in Fig. 3-2.

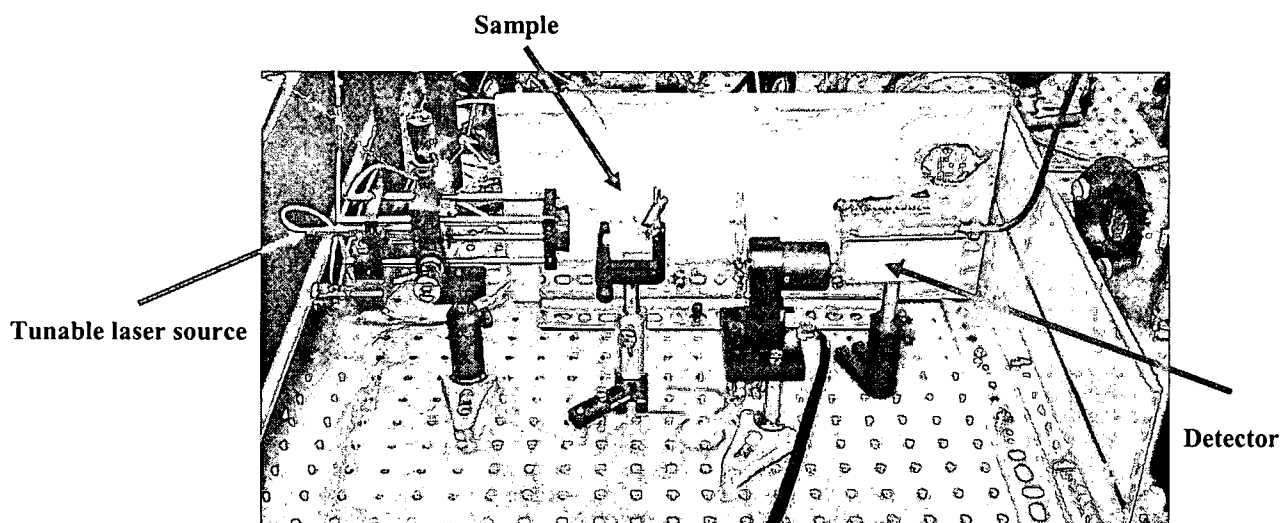


Fig. 3-2. Photograph of the experimental setup.

The measurement shows that the maximum peak in the transmission spectrum shifts to the right as temperature was increased. From this, a thermo-optic coefficient dn/dT for GaAs and AlAs can be determined. These measured results are depicted in Fig. 3-3. Since the resonant condition is $\lambda / 4n$, the refractive index can be deduced once the wavelength of the resonant peak is measured.

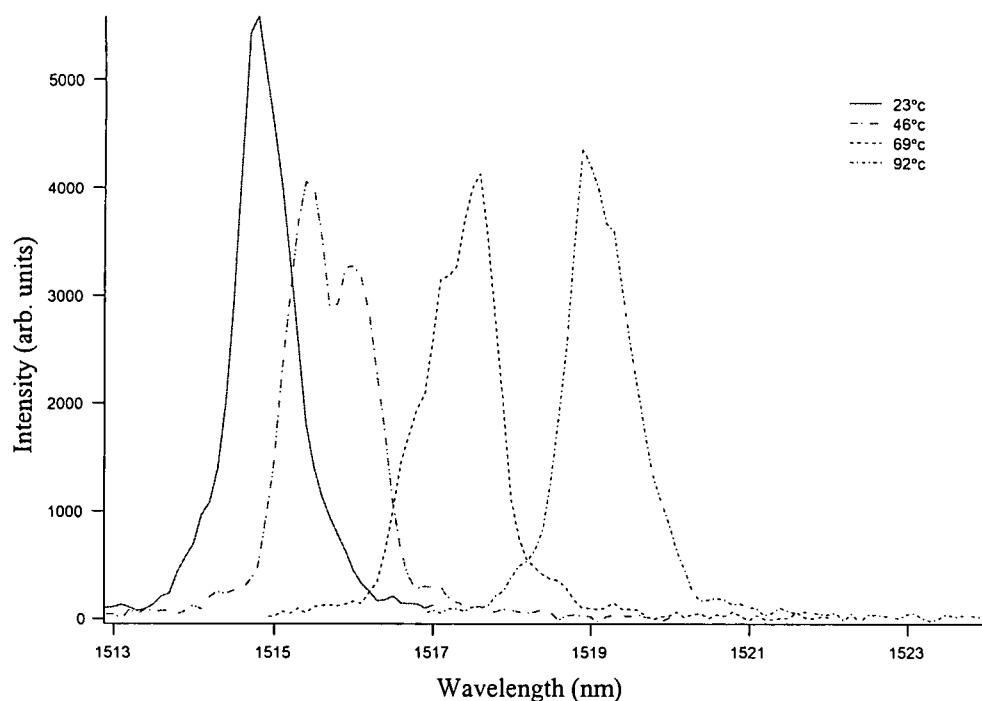


Fig. 3-3. Transmission spectrum shift vs. temperature on sample as a function of wavelength.

3.3 Results and discussion

The Sellmeier equation is normally used for calculating the refractive index of GaAs and AlAs at room temperature. These refractive indices are used as the reference as compared to the next value of the refractive index with temperature dependence. In deriving the new equation, the empirical Sellmeier equation for $\text{Al}_x\text{Ga}_{1-x}\text{As}$ material at room temperature is first used, which is written as [21]

$$n^2(x, \lambda) = 10.906 - 2.92x + \frac{0.97501}{\lambda^2 - C} - 0.002467(1.41x + 1)\lambda^2 \quad (3-1)$$

where $C = (0.52886 - 0.735x)^2$ for $x \leq 0.36$

$C = (0.30386 - 0.105x)^2$ for $x \geq 0.36$ and λ is the wavelength in vacuum.

If the coefficient of thermal expansion α_T is assumed to be linear with temperature, then the length at a temperature T_m is given by [22]

$$L_T = L_0[1 + \alpha_T(T_m - 26^\circ\text{C})] \quad (3-2)$$

where L_0 is the length at 26°C , T_m is the material temperature, and α_T is the thermal expansion coefficient, given as $6.4 \times 10^{-6}/^\circ\text{C}$, $5.2 \times 10^{-6}/^\circ\text{C}$ for GaAs and AlAs, respectively [23].

The data from the experiment resulted in a thermo-optic coefficient dn/dT of $2.04 \times 10^{-4}/^\circ\text{C}$ and $1.74 \times 10^{-4}/^\circ\text{C}$ for GaAs and AlAs respectively in the $1.46 \sim 1.58 \mu\text{m}$ wavelength and for temperatures between 26 and 86°C . Fig. 3-4 is the contour plot of the

transmission of the sample at $dT = 10^\circ\text{C}$. From the figure it can be clearly seen that a maximum transmission exists at the change in the refractive index dn (GaAs) = 2.04×10^{-3} and dn (AlAs) = 1.74×10^{-3} , respectively. The tolerable error can be $\pm 1 \times 10^{-6}/^\circ\text{C}$ for GaAs and $\pm 2.5 \times 10^{-7}/^\circ\text{C}$ for AlAs.

Note that the thermo-optic coefficient can be positive or negative depending on the particular material and wavelength. As temperature increases, the density of a material will become smaller due to thermal expansion, which will cause the refractive index to become smaller. On the other hand, semiconductor bandgaps generally shrink with increasing temperature, which will cause an increase in refractive index. The overall thermo-optic coefficient can therefore be positive or negative depending on the strengths of these competing effects. In this case, it was found that the thermo-optics coefficients for GaAs and AlAs are positive rather than negative.

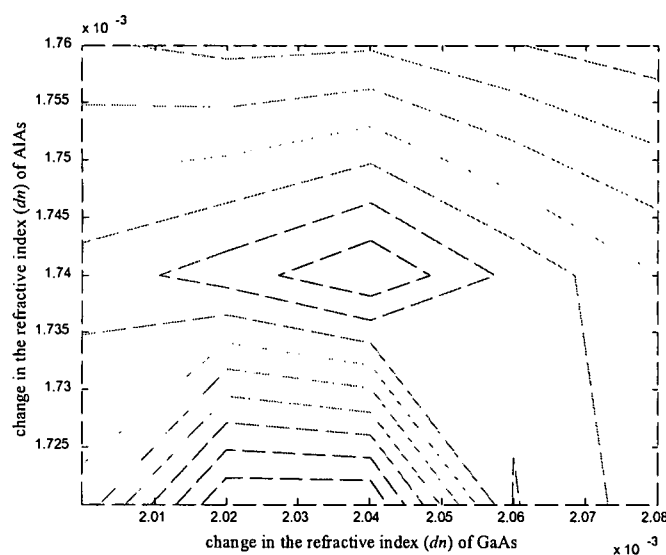


Fig. 3-4. Contour plot of the transmission of the sample with change in the refractive index of GaAs and AlAs.

Refractive indices of GaAs and AlAs versus temperature are shown in Fig. 3-5. This plot is constructed using the data from the TMM and our experimental results for dn/dT .

Considering the thermal expansion of the material and thermo-optic coefficient from the experimental data, the new empirical Sellmeier equation with temperature dependence is derived, which can be written as

$$n(x, \lambda, T) = [10.906 - 2.92x + \frac{0.97501}{\lambda^2 + C} - 0.002467(1.41x + 1)\lambda^2]^{1/2} + [(T - 26^\circ\text{C})(2.04 - 0.3x) \times 10^{-4} / ^\circ\text{C}] \quad (3-3)$$

The term in the second bracket represents the temperature-dependent Sellmeier coefficient, and the other parameters are the mole fraction x , wavelength λ , and temperature T .

The linear temperature dependence in equation (3-3) is justified by the measured results shown in Fig. 3-5 where the refractive indices of GaAs and AlAs with temperature are observed to be linear.

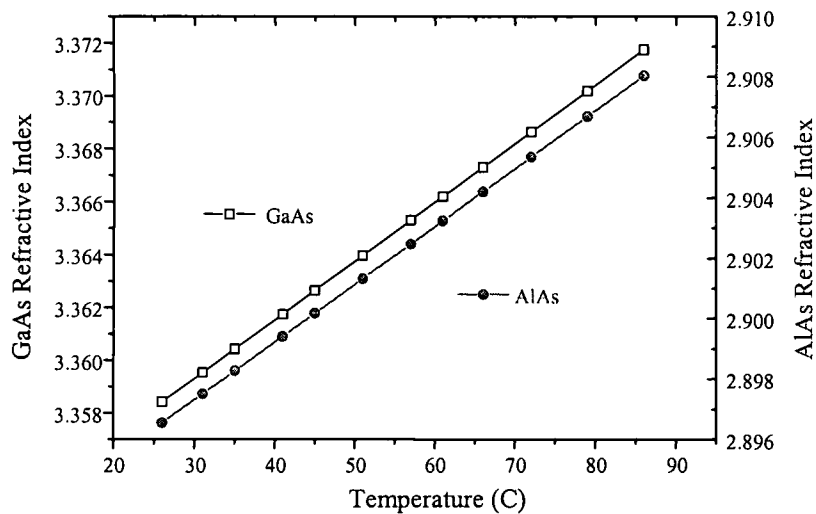


Fig. 3-5. Refractive indices of AlAs and GaAs as a function of temperature.

The variation of refractive index of $\text{Al}_x\text{Ga}_{1-x}\text{As}$ as a function of aluminum mole fraction x , wavelength λ , and temperature T as predicted by equation (3-3) is plotted in Fig. 3-6. As evident in Fig. 3-6, the refractive index increases slightly as temperature goes up and as the wavelength comes down.

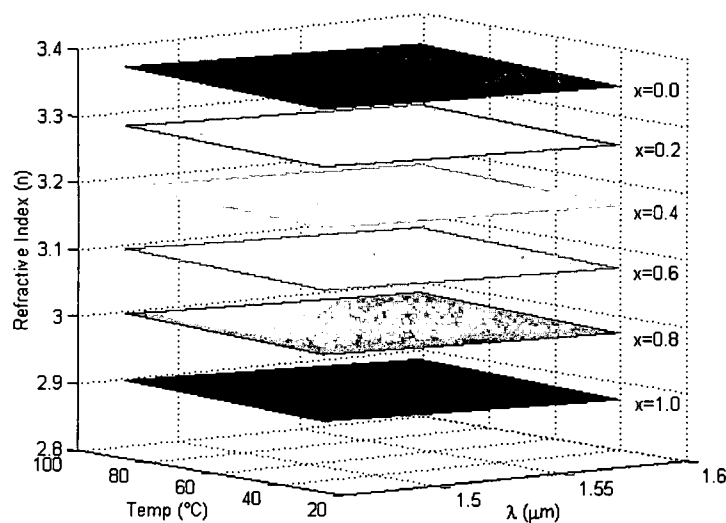


Fig. 3-6. Refractive index of $\text{Al}_x\text{Ga}_{1-x}\text{As}$ as a function of wavelength and temperature.

The experiment was conducted in the range of $1.46 \sim 1.58 \mu\text{m}$ and $26 \sim 86^\circ\text{C}$ so the modified Sellmeier equation given here is valid only in those ranges. However, it could be applied to other wavelengths and temperatures as well because the refractive index varies almost linearly with wavelength.

Table 1 shows the comparison of refractive index at $\lambda = 8.25 \mu\text{m}$ between room temperature (300 K) and 77 K, which is a temperature typically used in long-wave IR detectors, predicted by the modified Sellmeier equation derived here. The refractive

index of $\text{Al}_x\text{Ga}_{1-x}\text{As}$ was assumed to be linear and was extrapolated down to 77 K. It is quite possible that this linearity may not be strictly valid, but this aspect was not explored further in this dissertation.

Al mole fraction	300 K	77 K
0.0	3.279	3.234
0.1	3.231	3.186
0.2	3.181	3.137
0.3	3.131	3.088
0.4	3.081	3.038
0.5	3.029	2.987
0.6	2.976	2.935
0.7	2.923	2.882
0.8	2.868	2.828
0.9	2.813	2.773
1.0	2.756	2.717

Table 3-1. Comparison of refractive index at room temperature and cryogenic temperature in terms of Al mole fraction calculated using equation (3-3).

In order to verify the validity of new Sellmeier equation, the data obtained from equation (3-3) is compared with experimental data measured by Kawai *et al.* [24]. It can be seen in Fig. 3-7 that the new Sellmeier equation for $\text{Al}_x\text{Ga}_{1-x}\text{As}$ can be used not only in the range of $1.46 \sim 1.58 \mu\text{m}$ and at temperature of $26 \sim 86^\circ\text{C}$, but also at other wavelength ranges and temperatures except for wavelengths whose photon energy falls above the GaAs electronic bandgap. It is worth noting that the Sellmeier equation for GaAs is not very accurate above the bandgap. This explains the discrepancy in the figure shown below.

The small difference between the two curves is due to the absorption coefficient of $\text{Al}_x\text{Ga}_{1-x}\text{As}$ used in Ref [24].

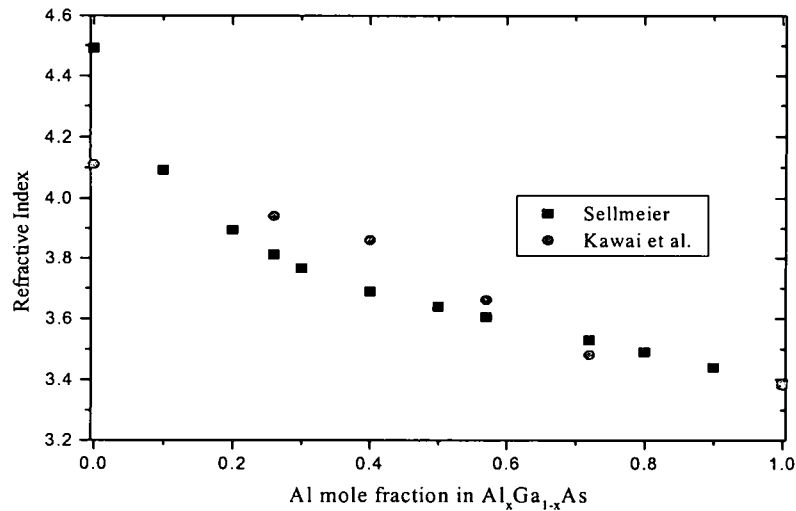


Fig. 3-7. Refractive index of $\text{Al}_x\text{Ga}_{1-x}\text{As}$ obtained by equation (3-3) at $0.6328 \mu\text{m}$ and 700°C . Circles represent the data obtained by Kawai *et al.* [24].

3.4 Conclusion

In this chapter, the temperature dependence of the refractive index of GaAs and AlAs in the wavelength range of $1.46 \sim 1.58 \mu\text{m}$ was measured. It is shown that the refractive index varies almost linearly with temperature in this range. From these results, the temperature-dependent Sellmeier equation for $\text{Al}_x\text{Ga}_{1-x}\text{As}$ can be developed. Since the refractive index varies almost linearly with temperature, this new equation can be applied

to the other wavelengths and temperature ranges as well. The measured temperature uncertainty was assumed to be no more than ± 1 °C.

Although $\text{Al}_x\text{Ga}_{1-x}\text{As}$ is a fairly mature semiconductor material in optoelectronics, it is somewhat strange that a temperature-dependent refractive index model for $\text{Al}_x\text{Ga}_{1-x}\text{As}$ has not been previously determined. This simple method would be useful in a variety of fields, especially where the devices undergo large temperature shifts.

CHAPTER IV

GRATING-COUPLED QUANTUM WELL INFRARED PHOTODETECTOR (QWIP)

4.1 Introduction

Quantum well infrared photodetectors (QWIPs) are an excellent candidate for imaging in the 3-5 μm and 8-12 μm range. QWIPs can be fabricated from alloys such as GaAs and AlGaAs and can be tuned to absorb a wide range of the infrared spectrum.

Although QWIPs have been demonstrated for IR applications, the polarization selection rule of intersubband transitions places a limit on the maximum quantum efficiency that can be achieved. In other words, QWIPs can only absorb light with whose electric field polarization perpendicular to the active layer. If the incident light is normal to the structure, as would be the case in a conventional photodetector application, no absorption will take place in the device because all the electric field in the incident radiation will be parallel to the quantum wells. Hence, QWIPs require a coupling mechanism to at least partially rotate the polarization of the incoming radiation.

Coupling mechanism such as random-reflectors [25], lamellar and crossed (doubly periodic) gratings [26], and linear grating [27] can be used to change the direction of propagation of the light and thus alleviate this problem.

The external quantum efficiency (QE) of these devices is limited primarily by the coupling mechanism used to scatter the light normal to the absorbing quantum wells. The QE is defined as the ratio of photon absorption that results in a photocurrent compared to the total incident photons. It is proportionally related with the specific detectivity D^* : The higher the QE, the better the performance of the detector. Even though the grating-coupled QWIPs have been demonstrated with QE of around 30%, they generally do not scale well to smaller geometries because the diffraction efficiency from gratings falls precipitously as the overall size of the gratings gets smaller. Hence the grating coupled approach is not favored in high density focal plane arrays where smaller detectors are typically required.

In this chapter, a resonant cavity enhanced (RCE) QWIP is proposed, with the goal of increasing the QE. As already verified in [28], the RCE structure produces a field enhancement around the active layers that increases the QE of the QWIP. The same effects are verified in the grating-coupled QWIP structure with distributed Bragg reflector (DBR) on both sides. In this way, multiple passes of light through active region can be possible until it gets absorbed completely.

4.2 Polarization selection rule

4.2.1 Dipole matrix element

The rate of electronic transitions W from an initial state $|i\rangle$ to a final state $|f\rangle$ under the influence of an electromagnetic field of frequency ω is given, by Fermi's golden rule, as

$$W = \frac{2\pi}{h} \left| \langle f | H' | i \rangle \right|^2 \Delta(E_f - E_i - \hbar\omega) f(E_i) [1 - f(E_f)] \quad (4-1)$$

where $f(E)$ is the Fermi-Dirac probability that the state at E is occupied and H' the interaction Hamiltonian. The Hamiltonian varies like $\mathbf{p} \cdot \mathbf{e}$ in the electric dipole approximation where \mathbf{p} is dipole moment and \mathbf{e} is the polarization.

The optical intensity can be written as

$$I(x) = I(0) e^{-\alpha(\hbar\omega)x} \quad (4-2)$$

where $\alpha(\hbar\omega)$ is the absorption coefficient of the semiconductor, which is the rate of energy loss per unit length in the propagation direction.

Substituting for H' into the absorption coefficient,

$$\alpha(\hbar\omega) = \frac{\beta}{\omega} \sum_{i,f} \left| \langle f | \mathbf{p} \cdot \mathbf{e} | i \rangle \right|^2 \Delta(E_f - E_i - \hbar\omega) [f(E_i) - f(E_f)] \quad (4-3)$$

where β is a sample-dependent optical constant. Equation (4-3) explains that the absorption spectrum can be derived if all states $|i\rangle$ and $|f\rangle$ through the electronic band structure are known. The most important factor in equation (4-3) is dipole matrix element.

Calculation of $\alpha(\hbar\omega)$ consists of summing the dipole matrix elements for all electron-hole transitions, subband-subband and excitonic contributions [29].

In a quantum well, the independent hole and electron state wavefunctions have the form

$$\langle \mathbf{r} / i \rangle = \exp(i\mathbf{k}_{\parallel} \cdot \mathbf{r}_{\parallel}) u_v(\mathbf{r}) \Psi_h(z), \quad \langle \mathbf{r} / f \rangle = \exp(i\mathbf{k}_{\parallel} \cdot \mathbf{r}_{\parallel}) u_c(\mathbf{r}) \Psi_e(z) \quad (4-4)$$

with $u_v(\mathbf{r})$ and $u_c(\mathbf{r})$ the valence and conduction band atomic basis state, respectively.

Here $\Psi_h(z)$ and $\Psi_e(z)$ are the hole and electron envelope function, respectively. In general the matrix element of the photon absorption process is given by [30]

$$\langle f | \mathbf{p} \cdot \mathbf{e} | i \rangle = \left[\langle u_c | \mathbf{p} \cdot \mathbf{e} | u_v \rangle \langle \Psi_e | \Psi_h \rangle + \langle u_c | u_v \rangle \langle \Psi_e | \mathbf{p} \cdot \mathbf{e} | \Psi_h \rangle \right] \delta(\mathbf{k}_{\parallel,e} - \mathbf{k}_{\parallel,h}) \quad (4-5)$$

which yields the selection rules for optical transitions. Conservation of in-plane wavevector \mathbf{k}_{\parallel} is required for optical transitions.

In the case of direct *interband* transitions, the second term of the above expression becomes zero, because at the same point in the Brillouin zone, the periodic functions in two different bands are orthogonal. In contrast, for the *intraband* transitions, which is the case one is interested in, the first term vanishes because of the fact that the Hamiltonian used to obtain Ψ_e and Ψ_h is Hermitian.

Substituting for the matrix element into the expression for the absorption coefficient in equation (4-3) and summing over \mathbf{k} states, the absorption coefficient can be written as

$$\alpha(\hbar\omega) = \frac{\beta}{\omega} \sum_{m,n} \gamma_h \left| \langle \Psi_{e,n} | \mathbf{p} \cdot \mathbf{e} | \Psi_{h,m} \rangle \right|^2 \theta(\hbar\omega - E_g - E_n - E_m) \quad (4-6)$$

where γ_h is the relative strength of the transition. According to equation (4-6), the matrix element of the interaction vanishes ($\mathbf{p} \cdot \mathbf{e} = 0$) when the incoming light contains no polarization parallel to \mathbf{p} . This imposes practical limitation on input coupling schemes of infrared photodetector, which mainly rely on intraband transitions.

4.2.2 The oscillator strength

The integrated absorption strength in QWIP can be written as [31]

$$\int_0^\infty \alpha(\nu) d\nu = \left(\frac{\rho_c N_w e^2 h f}{4 \epsilon_0 m^* c n} \right) \left(\frac{\sin^2 \theta}{\cos^2 \theta} \right), \quad (4-7)$$

where $\rho_c = N_D L_w$ is the two-dimensional density of carriers in the well, N_D is the three-dimensional carrier density, N_w is the number of doped wells, n is the index of refraction, θ is the angle between the direction of the optical beam and the surface normal, and f is the oscillator strength. This oscillator strength of the corresponding transition, often defined as the strength of optical transition, is given as [32]

$$f \equiv \frac{2m_e \omega}{\hbar^2} \langle z \rangle^2. \quad (4-8)$$

where m_e is the free-electron mass and z is the direction normal to the quantum well. From Eqs. (4-7) and (4-8), it is evident that the optical electric field must have a component parallel to z in order to induce an intersubband absorption since the oscillator strength only has a component along z . And also normal incident radiation, for example $\theta = 0$ in Eq. 4-7, will not be absorbed.

4.3 Vector diagram of light propagation in different structures

According to the polarization selection rule described in the previous section, propagating waves must have a component perpendicular to the QW layers in order to be absorbed. Under normal incidence, there is no way of getting waves that are perpendicular to the QW layers if TE and TM waves are defined to have the H field and E field along the z direction, and to propagate y direction (see Fig. 4-1).

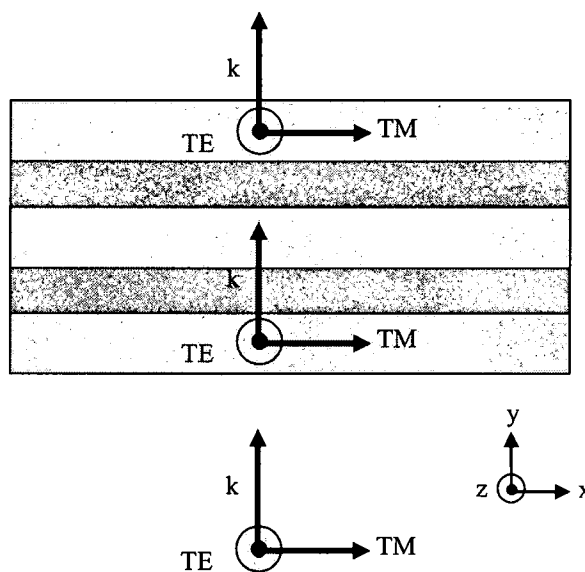


Fig. 4-1. Light propagation through the structure of QWIP *without* a grating.

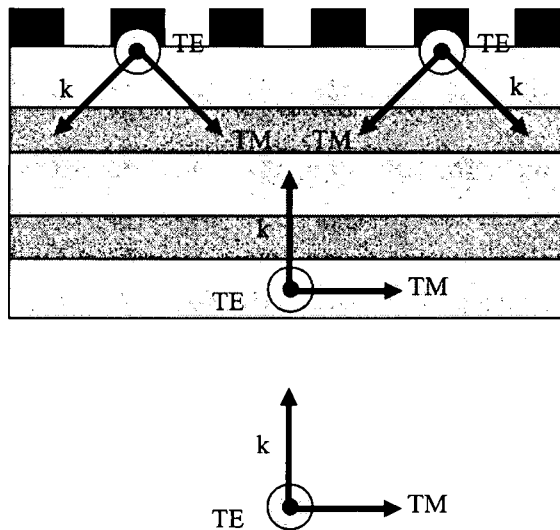


Fig. 4-2. Light propagation through the structure of QWIP *with* a grating.

However, TE and TM waves can be decoupled by the lamellar grating shown in Fig. 4-2. In this implementation, the TM waves have a component perpendicular to the active layer and will be absorbed. The TE waves will remain unabsorbed.

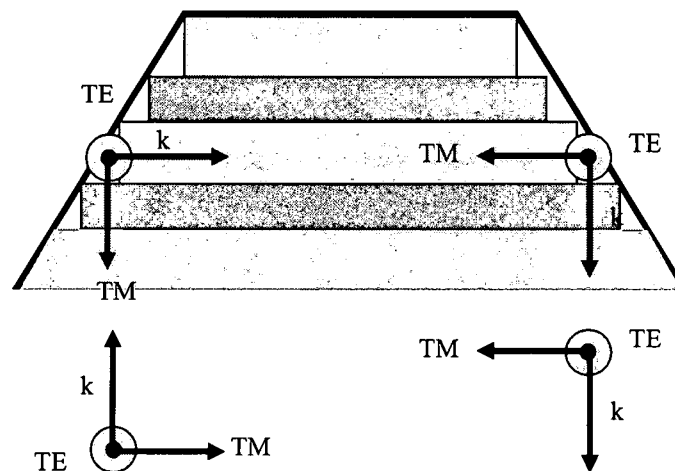


Fig. 4-3. Light propagation through the structure of C-QWIP with 45° oblique sidewalls.

The C-QWIP structure does not use a grating to rotate the field polarization. Instead, an oblique sidewall is used to redirect the light into the active region. When the incident light strikes the sidewall, the reflected TM waves will rotate their polarization to have a component perpendicular to QW layers while the TE waves will still remain parallel. Hence partial absorption will take place while the beam is traveling between the two oblique sidewalls.

4.4 Theory

The derivation presented in this section is based on the comprehensive analysis done by Andersson *et al.* [26] of the grating-coupled QWIP. In their work, they utilized the modal expansion method (MEM) [33] for the rigorous analysis of the diffraction properties of the gratings. The grating scattering matrix method (SMM) and TMM were used in the QW structure to obtain the QE in three different cases: lamella grating, crossed grating with box-shaped cavities, and crossed grating with cylindrical cavities. For brevity, the theoretical formulations in this section are limited to lamella grating only.

4.4.1 Scattering matrix of the lamellar grating

As described before, it is sufficient to consider only the TM waves since only they give rise to QW absorption due to the polarization selection rule.

The scattering matrix can be written as [26]

$$S = [S_p^r], \quad (4-9)$$

where the elements S_p^r denote the ratio of the p th-order scattered wave amplitude to the r th-order incident wave amplitude. The indexing is done as follows: The radiation to be detected which enters from the GaAs substrate and the corresponding wave with the same propagation angle, but with opposite propagation direction, are labeled zeroth order. The latter type of wave arises from diffraction from the grating as well as from multiple reflections in the epilayer interfaces. Waves with the same propagation angle as the grating orders -1 (-first order) and 1 (first order) are labelled, and so forth.

In the free half-space above the grating the TM plane waves can be written (expressed as the E field in the x - z plane, see Fig. 4-4) as

$$R_p(x, y) = (1/\sqrt{D}) \exp[j(\alpha_p x + \beta_p y)] \hat{x}, \quad (4-10)$$

with

$$\alpha_p = \alpha_0 + (2\pi p / D), \quad (4-11a)$$

$$\alpha_0 = k \sin(\theta), \quad (4-11b)$$

$$\beta_p = \sqrt{k^2 - \alpha_p^2}, \quad (4-11c)$$

where D is the grating constant, θ the angle of incidence, and the wave vector $k = 2\pi / \lambda$, λ being the wavelength in the material. p is the grating order: ($= \dots -1, 0, 1, \dots$) and \hat{x} signifies a unit vector.

The TM channel modal functions can be written

$$N_n(x, y) = M_n(x) \sin[\mu_n(y + h)], \quad (4-12)$$

with

$$M_n(x) = \sqrt{[(2 - \delta_{n0})/d]} \cos(n\pi x/d) \hat{x}, \quad (4-13a)$$

$$\mu_n = \sqrt{k^2 - (n\pi/d)^2}. \quad (4-13b)$$

where d is the channel width, h is the channel depth, δ_{ij} is the Kronecker delta, and the channel mode index is $n = 0, 1, \dots$.

The elements of the scattering matrix become

$$S_p^r = -\delta_{rp} + \sum_{n=0}^{\infty} c_n^r I_n^p \sin(\mu_n h). \quad (4-14)$$

The channel mode amplitudes c_n^r can be found from

$$\sum_{N=0}^{\infty} C_{Nn} c_N^r = D_n^r, \quad (4-15)$$

where

$$C_{Nn} = \sin(\mu_N h) Q_{Nn} + j(k/\mu_N) \cos(\mu_N h) \delta_{Nn}, \quad (4-16a)$$

$$D_n^r = 2(k/\beta_r) \overline{I_n^0}. \quad (4-16b)$$

Q_{Nn} can be written

$$Q_{Nn} = \sum_{p=-\infty}^{\infty} \frac{k}{\beta_p} I_N^p \overline{I_n^p}, \quad (4-17)$$

where the overbar indicates the complex conjugates. I_n^p is a scalar product of the type

$$I_n^p = \int_0^D \overline{R_p(x,0)} M_n(x) dx, \quad (4-18)$$

Finally one can get,

$$I_n^p = \left[\frac{(2 - \delta_{n0})}{dD} \right]^{1/2} \frac{j\alpha_p}{[(\alpha_p)^2 - (n\pi/d)^2]} \left[(-1)^n \exp(-j\alpha_p d) - 1 \right]. \quad (4-19)$$

From the manipulation steps (equations (4-10)-(4-19)), it was found that there is a mistake on the integration of equation (4-18) in the published results [26]. It would be correct if the integration limits were 0 to D . However, the result shown in equation (4-19) is for the integration from 0 to d . See the Fig. 4-4 below for the geometry of lamellar grating.

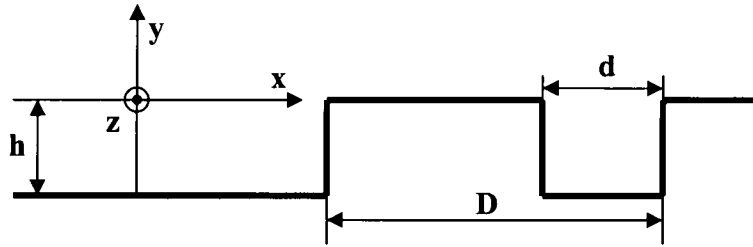


Fig. 4-4. Definition of the parameters describing the geometry of a lamellar grating (after reference [26]).

If one follows the integration given in the paper, one end up with different results. Assume that $\overline{I_n^0}$ is needed to calculate D_n^r , which equals to $2(k/\beta_r)\overline{I_n^0}$ shown in equation (4-16b). In the case of $p = 0$ from $\overline{I_n^0}$, α_p which can be expressed as $\alpha_p = \alpha_0 + (2\pi p/D)$, where $\alpha_0 = k \sin(\theta)$, should always be zero in normal incidence

when θ equals to zero. If α_p is zero, then $\overline{I_n^0}$ is zero from equation (4-19). Hence it is impossible to calculate D_n' in this case. Therefore the integration limit has to be from 0 to D , which is the period of the grating.

Therefore, the equation (4-19) was modified in order to interpret the formulation correctly. The solution to the integration is as follows:

$$I_n^p = \left[\frac{(2 - \delta_{n0})}{dD} \right]^{1/2} \frac{j\alpha_p}{[(\alpha_p)^2 - (n\pi/d)^2]} \left\{ \left[\cos\left(Dn\frac{\pi}{d}\right) + jn\pi \sin\left(Dn\frac{\pi}{d}\right) \frac{1}{\alpha_p d} \right] \exp(-j\alpha_p D) - 1 \right\} \quad (4-20)$$

In order to make the calculations manageable, only six waves (three incident and three scattered waves) are included in the scattering matrix with orders $p, r = -1, 0, 1$. This is a reasonable approximation near the first-order cutoff where $\lambda = D$. In equation (4-17) truncations according to $p = -3$ through $+3$ are made, and the channel orders $n = 0-5$ are included throughout.

4.4.2 Transfer matrices and the coupling of the grating to the MQW structure

As shown in Chapter 2, TMM can be used for the modeling of the optical properties of the epilayers including the multi-QW structure. Overall transfer matrices T^s can be written

$$T^s = \begin{bmatrix} T_{11}^s & T_{12}^s \\ T_{21}^s & T_{22}^s \end{bmatrix}. \quad (4-21)$$

The superscript s includes all relevant parameters needed for the definition of the plane waves: angle of propagation, TE or TM mode, etc. T^s acts on two-wave vectors of the type $(c_-^s, c_+^s)'$, where c_-^s denotes the wave amplitude of plane waves propagating towards the grating (negative y direction), and c_+^s propagation from the grating (positive y direction), (t = transpose). Transfer matrices of a layer sequence are obtained by successive multiplication of the matrices of the corresponding individual layers. One distinguishes between reflection matrices that describe the transfer through an interface, and bulk transfer matrices that model the transfer through a bulk layer. Absorption is taken care of by using a complex refractive index. Since infrared absorption in the QW layers is anisotropic, a different refractive index for TE and TM mode is utilized.

From the grating scattering matrix and the transfer matrices of the MQW structure, the entire wave pattern in the structure may be calculated as follows: The incident and scattered wave amplitude vector, respectively, close to a lamellar grating, become, for orders -1, 0, 1

$$\mathbf{c}_- = (c_-^{-1}, c_-^0, c_-^1)', \quad (4-22a)$$

$$\mathbf{c}_+ = (c_+^{-1}, c_+^0, c_+^1)', \quad (4-22b)$$

It can then be shown that

$$\mathbf{c}_- = \text{inv}(M) \cdot \mathbf{d}_-, \quad (4-23a)$$

$$\mathbf{c}_+ = S \cdot \mathbf{c}_-, \quad (4-23b)$$

where S is the grating scattering matrix, \mathbf{d}_- a wave amplitude vector of the incident radiation in the GaAs substrate, and inv denotes matrix inverse. If the radiation enters only through the zeroth order, which is normally the case,

$$\mathbf{d}_- = (0, 1, 0)'. \quad (4-24)$$

The elements of the matrix M can be written

$$M_{ij} = \delta_{rp}(T_{11})_p + S_p^r(T_{12})_p \quad (4-25)$$

for lamellar gratings. Column index j refers to incident reflection (order r) whereas row index i refers to scattered reflection (order p). T_{11} and T_{12} are matrix elements of the transfer matrix which pertains to the entire detector structure including all epilayers, for the reflection of order p .

When \mathbf{c}_- and \mathbf{c}_+ are known, the wave amplitude at any point in the epistructure may be calculated by letting the transfer matrices T_p^s act on the two-wave vectors $(c_-^s, c_+^s)'$, where s denotes the order number and polarization. From the amplitudes, the radiation power density in a direction perpendicular to the epilayers can be found by the calculation of Poynting's vector, and from this the quantum efficiency is easily extracted as will be discussed below.

4.4.3 Calculation of quantum efficiency

The quantum efficiency is found from the Poynting vector. The power density in the y direction becomes

$$I_y = \frac{1}{2} \text{Re}(\mathbf{E} \times \mathbf{H}^*)_y, \quad (4-26)$$

where \mathbf{E} and \mathbf{H} are the electric- and magnetic-field intensity, respectively (* indicates the complex conjugate). It can be shown that the power density at the point $y = y_0$, corresponding to the two-wave vector $(c_-^s, c_+^s)^t$ assuming unity intensity of the radiation incident along the zeroth direction, becomes for TM mode

$$I_{y0}^s = \text{Re}[k / \beta^s (|c_+^s|^2 - |c_-^s|^2)] + 2 \text{Im}(k / \beta^s) \text{Im}(c_-^s c_+^{s*}), \quad (4-27)$$

where β^s is the y component of the wave k vector. The total power density I_{y0}^{tot} is found by adding the contributions of all two-wave vectors: $I_{y0}^{tot} = \sum_s I_{y0}^s$.

The QE η , which is the amount absorbed in a slice containing the QWs and confined between $y = y1$ and $y = y2$ is finally obtained by

$$\eta = I_{y2}^{tot} - I_{y1}^{tot}. \quad (4-28)$$

4.4.4 FDTD method in 2-dimensions

The FDTD formulation in 1-dimension was described in section 2.4.1. To deal with a QWIP structure, a 2-dimensional FDTD method needs to be implemented to separately treat the TE and TM modes

In 2-dimensions, Maxwell's equation can be written as

$$\frac{\partial \tilde{D}}{\partial t} = \frac{1}{\sqrt{\epsilon_0 \mu_0}} \nabla \times H, \quad (4-29a)$$

$$\tilde{D}(\omega) = \epsilon_r^*(\omega) \cdot \tilde{E}(\omega), \quad (4-29b)$$

$$\frac{\partial H}{\partial t} = -\frac{1}{\sqrt{\epsilon_0 \mu_0}} \nabla \times \tilde{E}. \quad (4-29c)$$

Since the primary interest is in TM modes, equations (4-29) are now reduced to

$$\frac{\partial D_z}{\partial t} = \frac{1}{\sqrt{\epsilon_0 \mu_0}} \left(\frac{\partial H_y}{\partial x} - \frac{\partial H_x}{\partial y} \right), \quad (4-30a)$$

$$D_z(\omega) = \epsilon_r^*(\omega) \cdot E_z(\omega), \quad (4-30b)$$

$$\frac{\partial H_x}{\partial t} = -\frac{1}{\sqrt{\epsilon_0 \mu_0}} \frac{\partial E_z}{\partial y}, \quad (4-30c)$$

$$\frac{\partial H_y}{\partial t} = \frac{1}{\sqrt{\epsilon_0 \mu_0}} \frac{\partial E_z}{\partial x}. \quad (4-30d)$$

Implementing a finite difference scheme for Eqs. (4-30a), (4-30c), and (4-30d) results in the following difference equations.

$$\begin{aligned} D_z^{n+1/2}(i, j) = D_z^{n-1/2}(i, j) &+ \frac{\Delta t}{\Delta x \sqrt{\epsilon_0 \mu_0}} \left(H_y^n(i+1/2, j) - H_y^n(i-1/2, j) \right) \\ &- \frac{\Delta t}{\Delta x \sqrt{\epsilon_0 \mu_0}} \left(H_x^n(i, j+1/2) - H_x^n(i, j-1/2) \right), \end{aligned} \quad (4-31a)$$

$$H_x^{n+1}(i, j+1/2) = H_x^n(i, j+1/2) - \frac{\Delta t}{\Delta x \sqrt{\epsilon_0 \mu_0}} \left(E_z^{n+1/2}(i, j+1) - E_z^{n+1/2}(i, j) \right), \quad (4-31b)$$

$$H_y^{n+1}(i+1/2, j) = H_y^n(i+1/2, j) + \frac{\Delta t}{\Delta x \sqrt{\epsilon_0 \mu_0}} (E_z^{n+1/2}(i+1, j) - E_z^{n+1/2}(i, j)). \quad (4-31c)$$

4.4.4.1 The perfectly matched layer (PML)

As the wave propagates outward, it will eventually come to the edge of the allowable computational space. Without a proper boundary condition, unphysical reflections would be generated that would send power back into the structure. There should be certain way to determine which one is the real wave and which one is the reflected junk. This is why absorbing boundary conditions (ABCs) have been an issue for as long as FDTD has been used. There have been numerous approaches to this problem [34, 35].

One of the most flexible and efficient ABCs is the perfectly matched layer (PML) developed by Berenger [36]. The basic idea is as follows; if a wave is propagating in medium 1 and it impinges upon medium 2, the amount of reflection is dictated by the intrinsic impedance of the two media

$$\Gamma = \frac{\eta_1 - \eta_2}{\eta_1 + \eta_2} \quad (4-32)$$

which are determined by the dielectric constants ϵ and permeabilities μ of the two media

$$\eta = \sqrt{\frac{\mu}{\epsilon}} \quad (4-33)$$

More detailed explanation of the PML can be found in reference [37].

4.5 Schematic diagram of the grating-coupled QWIP

Fig 4-5 shows the schematic diagram of grating-coupled QWIP structure. The structure is grown on a semi-insulating GaAs substrate with 100 μm thickness. It consists of 50 GaAs quantum wells with 5 nm thickness and 50 $\text{Al}_{0.25}\text{Ga}_{0.75}\text{As}$ barriers with 30nm thickness. GaAs contact layers with 0.5 μm thickness are located on both sides. Light is incident on the semi-insulating GaAs substrate of the detector.

4.6 Schematic diagram of the grating-coupled QWIP with a AlAs layer

In order to enhance the QE, an AlAs layer of thickness 3 μm is located below the bottom contact layer. This layer is referred to as a waveguide in the literature [26], created by the grating on one side of the multi-QW layers, and a thick AlAs on the other side. However, it is different from the conventional definition of dielectric waveguides. In order to avoid confusion, this structure will be called the grating-coupled QWIP with an AlAs layer hereafter. The purpose of using an AlAs layer in the grating-coupled QWIP is to make the light reflect back into the quantum well, increasing the probability of absorption. Fig. 4-6 shows the grating-coupled QWIP with an AlAs layer. It is identical to Fig. 4-5 except the AlAs layer on the top of the semi-insulating GaAs substrate.

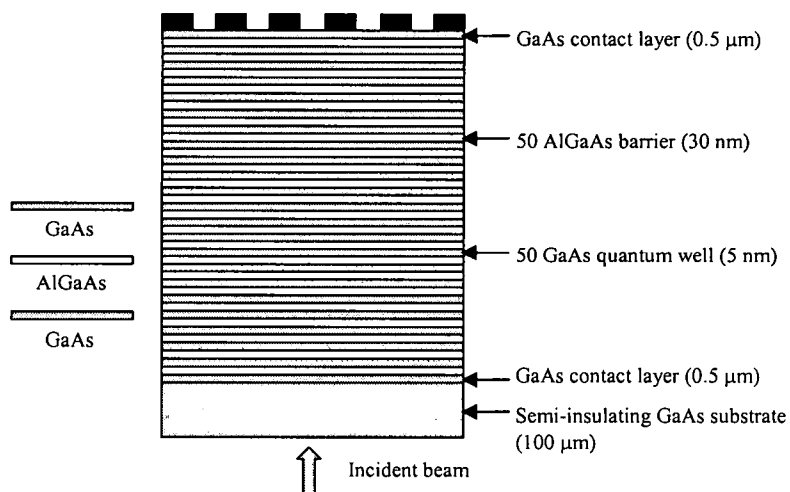


Fig. 4-5. Schematic diagram of the grating-coupled quantum well infrared photodetector.

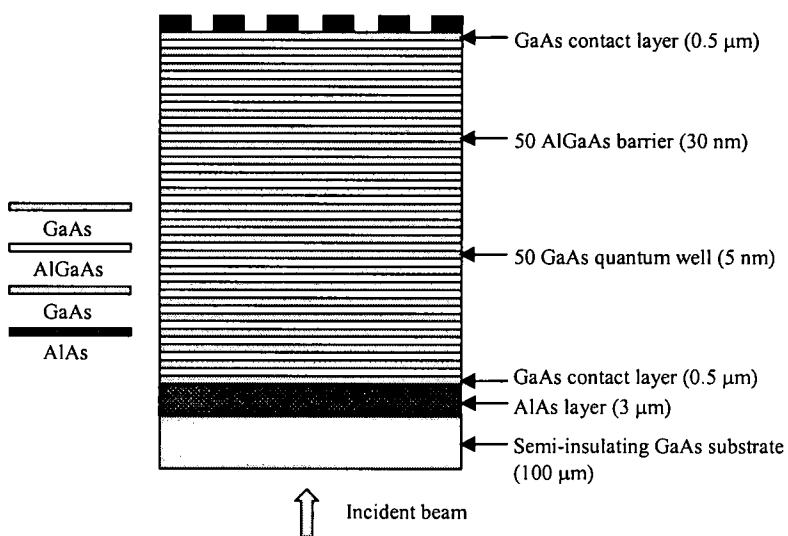


Fig. 4-6. Schematic diagram of the grating-coupled quantum well infrared photodetector with an AlAs layer.

4.7 Schematic diagram of the grating-coupled RCE-QWIP

The proposed schematic diagram of a grating-coupled RCE-QWIP is shown in Fig. 4-7. As can be seen from Fig. 4-7, two DBR stacks are located on top of the substrate and grating, respectively. The DBR stacks consist of GaAs and AlAs pairs. To create a high reflectivity, 10 pairs for the DBR are needed on top of the grating. 2 pairs of DBR stacks on the bottom of the contact layer are enough to create the resonant cavity in this case.

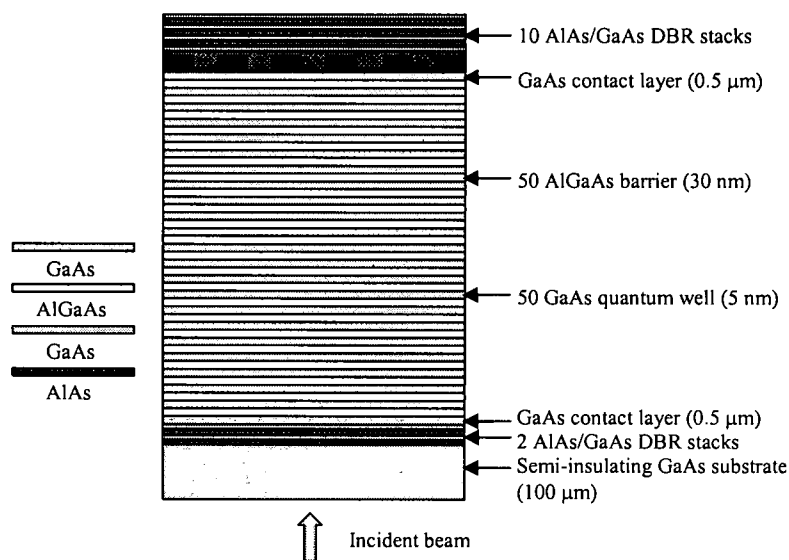


Fig. 4-7. Schematic diagram of the proposed grating-coupled RCE-QWIP.

4.8 Simulation results and discussion

4.8.1 Quantum efficiency at normal incidence

4.8.1.1 Numerical calculation

Based on the modified equation (4-20) from the previous section, the QW structure is calculated to deduce the QE. The same configurations specified in the paper [26] are used in this calculation. In order to calculate the refractive index for a doped contact layer, a Drude model is used. Since QW absorption takes place only if the electric field has a component perpendicular to the QW planes, the complex dielectric constant which is perpendicular to the QW planes is needed to obtain the refractive index for QW layers.

4.8.1.2 FDTD simulation

To compare with the calculation from the preceding section, a 2-dimensional FDTD method described in chapter II was used. The FDTD method is nothing but a solution to Maxwell's equations and does capture the all physical effects across the each layer accurately.

4.8.1.3 Result and discussion

The results of QE vs. wavelength for the grating-coupled QWIP and the grating-coupled QWIP with an AlAs layer are plotted in Fig. 4-8 using both numerical calculation and FDTD simulation. Note that the enhancement of QE in the grating-coupled QWIP with an AlAs layer becomes clear in both simulations. In the grating-coupled QWIP with an AlAs layer, lights reflect back into the quantum well at the boundary of GaAs and AlAs layers, increasing the probability of absorption. This light reflection can be created due to the large refractive index difference between GaAs and AlAs layers. The refractive indices for GaAs and AlAs as found from empirical Sellmeier equation [38] is used in the numerical and FDTD simulation reported in this section.

Although the grating-coupled QWIP with an AlAs layer has a high QE, it is still desirable to examine an alternative way for achieving higher performances. So the RCE concept to the grating-coupled QWIP is introduced as shown in Fig. 4-7 to make the light travel through the quantum well multiple times.

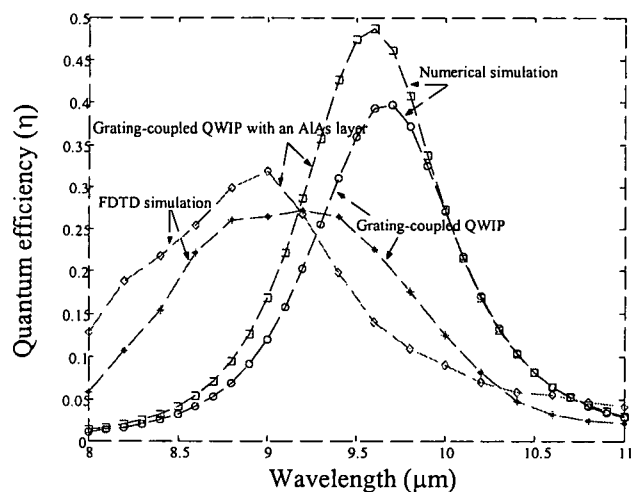


Fig. 4-8. Numerical and FDTD simulation results of quantum efficiency as a function of wavelength in the grating-coupled QWIP and the grating-coupled QWIP with a AlAs layer.

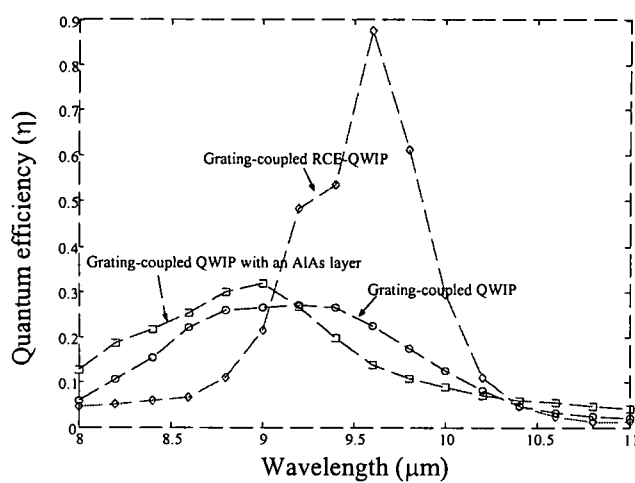


Fig. 4-9. Quantum efficiency as a function of wavelength in RCE-QWIP.

FDTD simulation results for the grating-coupled QWIP, the grating-coupled QWIP with an AlAs layer and for the grating-coupled RCE-QWIP are shown in Fig. 4-9. As can be seen, more than 50% QE can be achieved by using the RCE structure. Notice that the spectral bandwidth of the grating-coupled RCE-QWIP is much smaller than that of the grating-coupled QWIP and the grating-coupled QWIP with an AlAs layer due to the resonant cavity effect.

Note that the FDTD simulation includes all of the essential considerations such as the SWE and the refractive index profiles across every layer. All of the physical effects naturally emerge from the simulation without having to introduce them separately. It is also possible to predict the time constant when the structure reaches the steady-state condition. At a wavelength of 9.6 μm , the steady-state condition can be achieved at 3.63 ps in case of grating-coupled RCE-QWIP. More details of this aspect are explained in section 4.8.3 in this chapter.

Even though the RCE scheme provides high QE, there is a drawback of using this approach since the maximum value of QE occurs only at the desired wavelength, for example, 9.6 μm in this case. Furthermore, detectors operating in the long wavelength range have thick DBR pairs to meet the resonant cavity condition. Since it is optimized at $d = \lambda / 4n$, the thickness of each layer will be 0.87937 μm and 0.73407 μm for AlAs and GaAs, respectively at $\lambda = 9.6 \mu\text{m}$. These are very thick layers for growth using MBE or MOCVD.

4.8.2 Quantum efficiency as a function of angle of incidence

The dependence of quantum efficiency on the angle of incidence is shown in Fig. 4-10 for the grating-coupled QWIP, the grating-coupled QWIP with an AlAs layer and for the grating-coupled RCE-QWIP. It is found that QE is nearly constant up to 5 degrees in both cases of the grating-coupled QWIP and the grating-coupled QWIP with an AlAs layer; say a 10 degrees full cone angle of incidence. In the case of the grating-coupled RCE-QWIP, however, QE degrades dramatically, which is mostly constrained by the angle of incidence because of their use of DBR stacks on both sides. Nevertheless, one can still achieve the high enhancement of QE within small angle of incidence (i.e. below 4 degrees) in the grating-coupled RCE-QWIP.

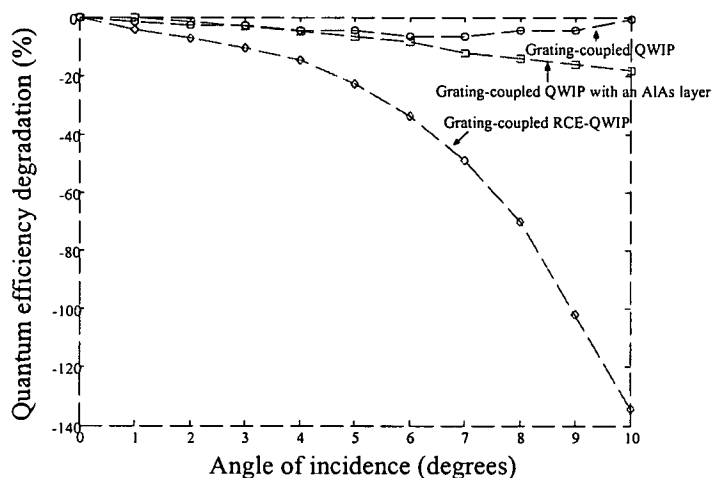


Fig. 4-10. Quantum efficiency degradation in terms of angle of incidence.

4.8.3 Steady-state analysis using FDTD

It is important to know how long it takes for the system reaches the steady-state condition. Unlike other methods, FDTD method is capable of providing this information since the simulation is performed in the time domain. Fig. 4-11 shows the time to reach steady-state as a function of wavelength in three different cases; the grating-coupled QWIP, the grating-coupled QWIP with an AlAs layer, and the grating-coupled RCE-QWIP. As can be seen, the RCE structure needs a longer time than the other two due to the DBR stacks located on both sides of the structure. Mean values of the grating-coupled QWIP, the grating-coupled QWIP with an AlAs layer, and the grating-coupled RCE-QWIP cases are 0.61 ps, 1.12 ps, and 3.98 ps, respectively.

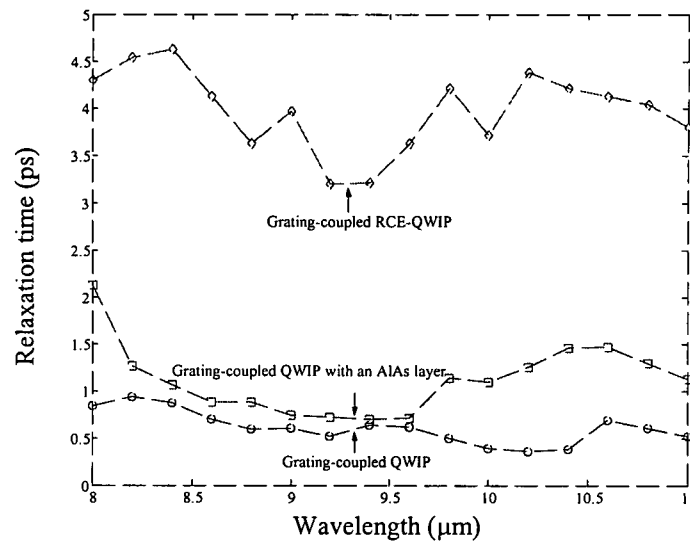


Fig. 4-11. Time to reach steady-state in three different cases; the grating-coupled QWIP, the grating-coupled QWIP with an AlAs layer, and the grating-coupled RCE-QWIP.

4.9 Conclusion

In this chapter, the improvement of QE using the RCE structure on existing grating-coupled QWIP has been demonstrated. It becomes clear that the enhancement of the QE is possible by introducing an AlAs layer on top of the GaAs substrate. This structure provides light reflection back into the quantum well at the boundary of GaAs and AlAs layers, increasing the probability of absorption. The QE can be further increased by the use of RCE approach due to multiple passes of photons through QW stacks. From the simulation results, the enhancement of the quantum efficiency in the grating-coupled RCE-QWIP is more than 50% over the grating-coupled QWIP with an AlAs layer.

Dependence of QE on the angle of incidence is also discussed. It is found that QE is nearly constant up to 5 degrees of incidence angle in both cases of the grating-coupled QWIP and the grating-coupled QWIP with an AlAs layer. QE, however, degraded dramatically in case of the grating-coupled RCE-QWIP due to constrain factor from the DBR stacks on both sides.

Finally, it is proven that RCE structure can be implemented successfully with a grating-coupled QWIP for the QE enhancement. FDTD method enables to analyze the QWIP structure accurately and to provide the analysis of steady-state condition.

CHAPTER V

RESONANT CAVITY ENHANCED (RCE) CORRUGATED QUANTUM WELL INFRARED PHOTODETECTORS (C-QWIP)

5.1 Introduction

The corrugated quantum well infrared photodetector (C-QWIP) [39-40] provides several advantages over the grating-coupled QWIP. Since it operates on reflection rather than diffraction, the corrugated coupling scheme is both pixel-size and wavelength-independent. As discussed in chapter 4, only light with electric field component perpendicular to the QW layers can be absorbed due to the dipole selection rule. To alleviate this problem, C-QWIP uses total internal reflection (TIR) to redirect the light into the QW detector. In this way, one can rotate the electric field component perpendicular to the layers for 50% of the incident unpolarized photons.

Even though the quantum efficiency of C-QWIP is higher than grating couplers, QWIPs in general lag behind competing technologies such as HgCdTe, which have nearly 100% efficiency because they do not utilize quantum wells and hence do not suffer from the polarization selection rule.

In this chapter, a novel design is presented that utilizes a resonant cavity for multiple passes of photons through the active region in order to increase the absorption probability and hence increase the QE and reduce the dark current. The simulation results for the RCE C-QWIP structure using multi-layer Bragg stacks as reflecting elements is presented.

The FDTD method in 2-dimensions [41] was used for the RCE-CQWIP simulation. As described in the preceding chapters, FDTD is a direct solution of Maxwell's curl equations, and it includes all of the essential considerations such as the standing wave effect and the refractive index profiles across every layer without any assumptions about the shape of these fields.

5.2 Schematic diagram of RCE-CQWIP

Fig. 5-1 illustrates the proposed schematic diagram of the RCE-CQWIP, which is a new design concept presented in this chapter. The upper part of the diagram is a standard C-QWIP structure, and the RCE-CQWIP is constructed by adding a distributed Bragg reflector (DBR) on the bottom.

In a C-QWIP design [39-40], the incident light reflects at the angled sidewalls and travels at a large oblique angle, allowing for efficient infrared absorption. However, it only makes one optical pass, which is one reason for the low QE in C-QWIPs

On the other hand, in the proposed RCE- CQWIP design, the incident light makes multiple passes across the active region, improving the probability of absorption, increasing the QE of the device. The transient effect in DBR RCE photodetectors is analyzed in [28], and in this chapter that concept is extended to RCE-CQWIPs.

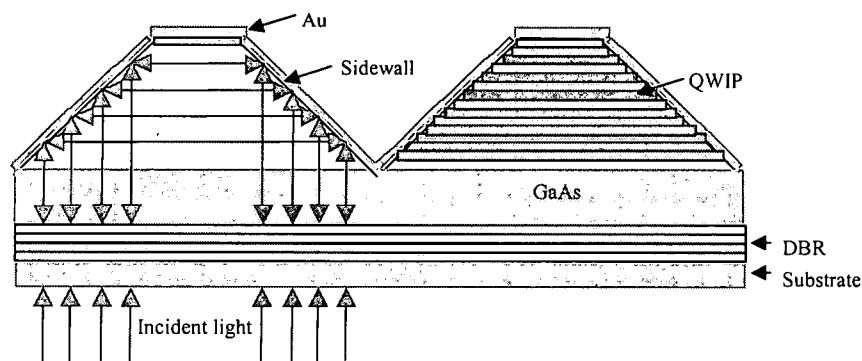


Fig. 5-1. Proposed schematic diagram of the RCE-CQWIP.

The DBR stacks for the RCE-CQWIP is composed of 3 pairs of GaAs/AlAs to create a resonance between the two top reflecting sidewalls, assuming that they reflect nearly 100% of light due to TIR. The refractive indices for AlAs and GaAs as found from ref. [38] and are used in the FDTD simulation reported in this section.

5.3 Simulation results and discussion

First, the standard C-QWIP structure is simulated to verify the quantum efficiency calculated in reference [42]. 29% QE was demonstrated at $\lambda = 8.25 \mu\text{m}$ with a corrugation period (pixel size) of $8 \mu\text{m}$ in C-QWIP structure. As is evident in Fig. 5-2, the simulation result from FDTD is in general agreement with the published analytical results previously. This verification step was done in order to validate the FDTD model, and to perform simulations on the proposed RCE-CQWIP structures with a greater degree of confidence.

As explained in previous chapters, RCE detectors have a greater sensitivity to incident wavelength than non-RCE detectors. Hence, the resonant wavelength needs to be determined before conducting a thorough simulation of QE. The RCE-CQWIP was simulated as a function of the thickness of the bottom GaAs layer (Fig. 5-3) so that the proper resonant condition is determined. The maximum QE is achieved when the thickness of bottom GaAs layer is $0.7 \mu\text{m}$. Simulation results for the RCE-CQWIP as well as C-QWIP are shown in Fig. 5-4. The quantum efficiency of the C-QWIP structure can be enhanced up to 12 % at $\lambda = 8.25 \mu\text{m}$ using of the proposed RCE-CQWIP structure.

Fig. 5-5 shows the dependence of QE on the angle of incidence for the standard C-QWIP and RCE-CQWIP. In this plot, we have defined the QE degradation as $(\eta_{\text{max}} - \eta)/\eta$ [8]. Interestingly, the standard C-QWIP shows an increase in QE up to 3 degrees. This can be explained by using a simple ray diagram shown in Fig. 5-6. Normal incidence is shown

by the solid line (1a). At small incident angles (dotted line (2a)), the QE is primarily determined by the absorption path length through the quantum wells. Since the absorption path length gets larger at larger incident angles, the QE starts to increase. The plane of incidence contains the TM wave vector, which is perpendicular to quantum well layers (see (5) in Fig. 5-6 for the definition of TE and TM polarizations). Beyond a certain incident angle (dashed line (3a)), the absorption length can no longer increase, and the QE becomes primarily determined by the extent of polarization perpendicular to the quantum wells. As a result, the QE starts to degrade. At even larger incident angles (dash-dot line (4a)), the photons are able to reflect back from the bottom substrate causing an increase in QE. In this simplified ray diagram, we have ignored the small changes in angles that can occur across the layers, i.e. substrate to barrier, barrier to quantum well, etc.

The RCE-CQWIP detector shows a slightly different behavior due to the angular constraints of the DBR stacks. It is found that QE remains nearly constant below 3 degrees because, unlike a planar interface, the incident angle changes direction when passing through the DBR stacks. Nevertheless, the RCE-CQWIP's behavior of QE vs incident angle is very similar to the standard C-QWIP, and that makes RCE-CQWIP a promising approach.

Dependence of QE on the angle of incidence for RCE-CQWIP shows a different behavior from the previous behavior shown in Fig. 4-10. In the C-QWIP structure, the sidewalls are used in place of the top DBR stacks, while the grating coupled QWIP uses DBR

stacks for both reflectors. The angular sensitivity is now diminished due to the sidewalls in the RCE-CQWIP.

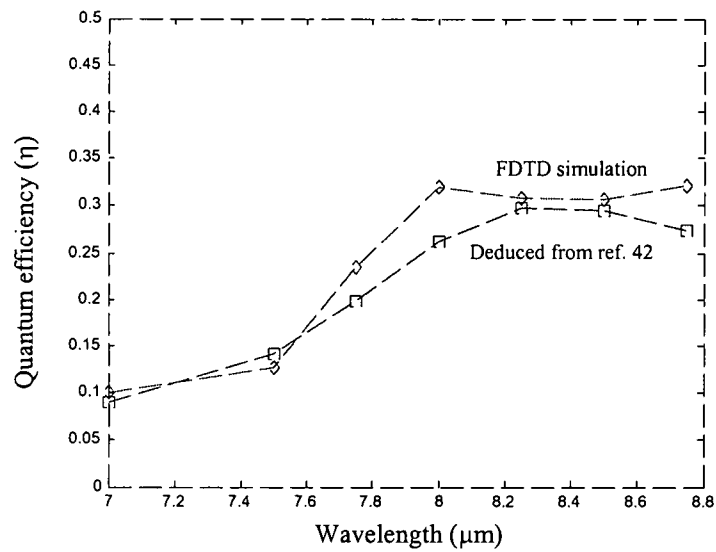


Fig. 5-2. Quantum efficiency as a function of wavelength in C-QWIP structure.

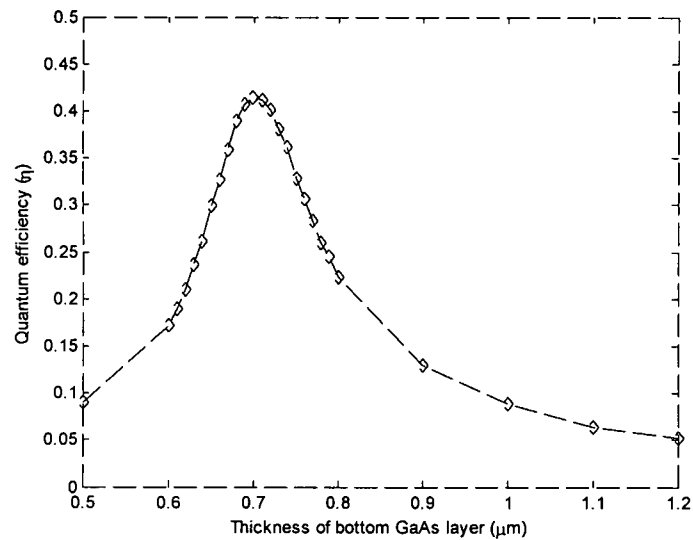


Fig. 5-3. Quantum efficiency vs thickness of bottom GaAs layer.

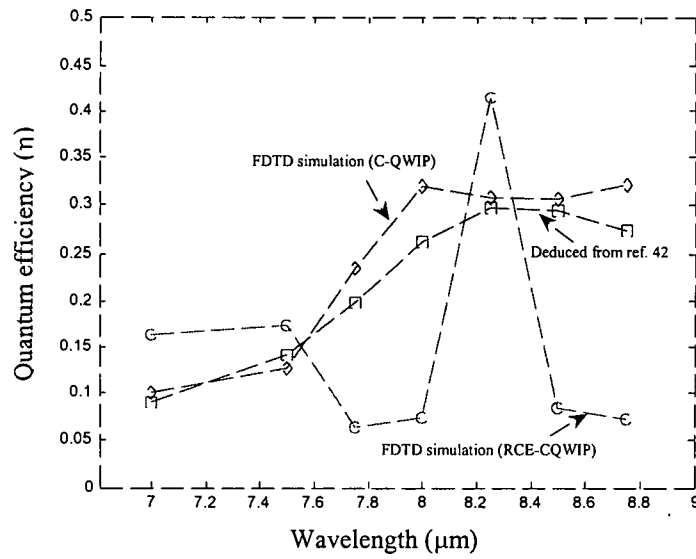


Fig. 5-4. The comparison of quantum efficiency between C-QWIP and RCE-CQWIP structure.

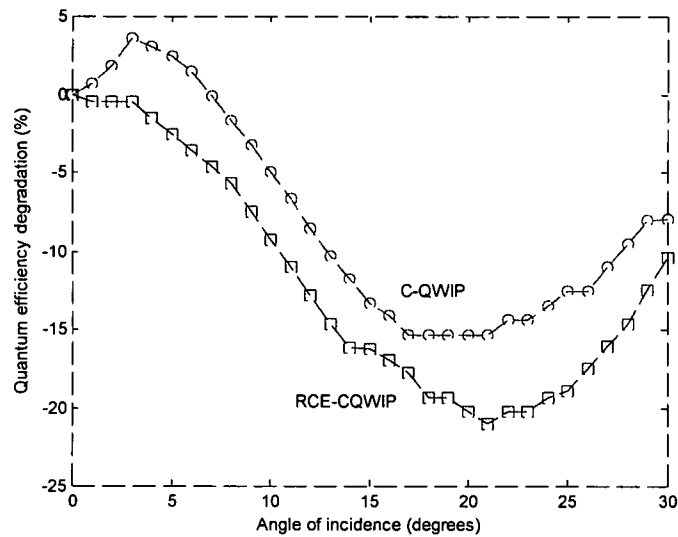


Fig. 5-5. Dependence of angle of incidence for C-QWIP and RCE-CQWIP.

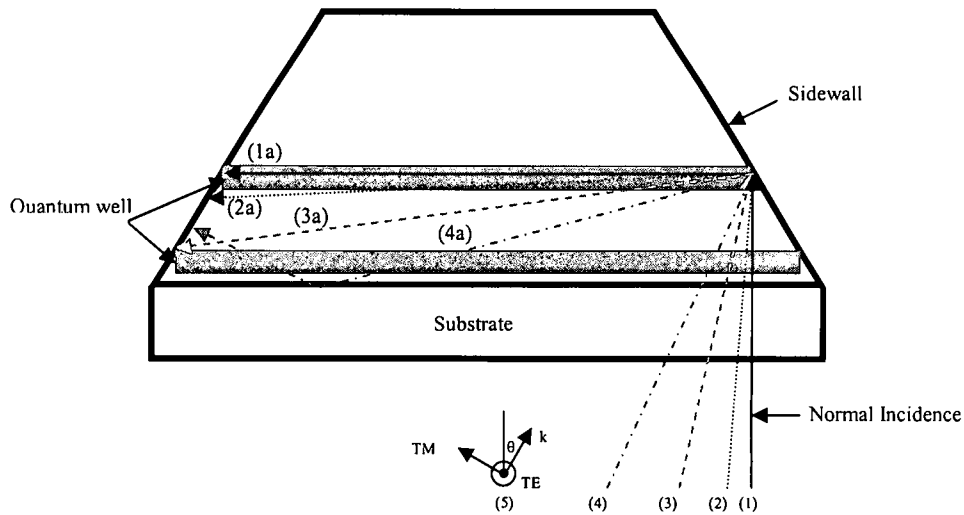


Fig. 5-6. Ray diagram of incident light at different angle in the C-QWIP structure.

5.4 Conclusion

A new concept of a resonant cavity C-QWIP (RCE-CQWIP) is introduced and simulated in this chapter. FDTD simulation results show that QE of 42% can be achieved using the novel design approach. Dependence of QE on the angle of incidence is also discussed. It was found that QE degrades by less than 1% for angles less than 3° in the RCE-CQWIP. This implies that the angular dependence of the detector performance is not too large to become a serious practical limitation, and the structure should be able to accommodate a range of focusing optics and F-numbers.

CHAPTER VI

RCE-CQWIP WITH A FORM BIREFRINGENCE LAYER

6.1 Introduction

In the previous chapter, a new design approach for the RCE-CQWIP structure was proposed and simulated using the FDTD method. 12% enhancement in QE was demonstrated for this structure. Despite this enhancement, the RCE-CQWIP still does not detect nearly half of optical power contained in the TE waves. Hence the maximum theoretical efficiency is limited to 50%, and practical values are often around 30% [42]. An innovative approach to overcome this limitation is proposed in this chapter. This is accomplished by introducing an integrated polarization rotating birefringence layer consisting of Ge and ZnS films. This structure enables the detection of the remaining 50% of the radiation by recycling the unabsorbed photons with a slightly rotated polarization on each round trip around the cavity.

In this chapter, the design of the form birefringence layer is investigated to extract the other 50% of the radiation contained in the TE mode. For the form birefringence

simulation, second-order effective medium theory (EMT) [43] and the rigorous coupled wave analysis (RCWA) [44] have been used.

6.2 Background of form birefringence

The birefringence properties of crystals are explained in terms of the anisotropic electrical properties of molecules of which the crystals are composed [7]. Birefringence may, however, arise from anisotropy on a scale much larger than molecular, namely when there is an ordered arrangement of similar particles of optically isotropic material whose size is large compared with the dimensions of the molecules, but small compared to the wavelength of light. This phenomenon is called form birefringence.

From optical measurements information may often be obtained about the submicroscopic particles that give rise to form birefringence. The principle will be explained by considering the somewhat idealized case of a regular assembly of particles that have the form of thin parallel plates. Let ϵ_1 be the dielectric constant of each plate and ϵ_2 the dielectric constant of the space between the plates. See Fig. 6-1 for a schematic diagram of this configuration.

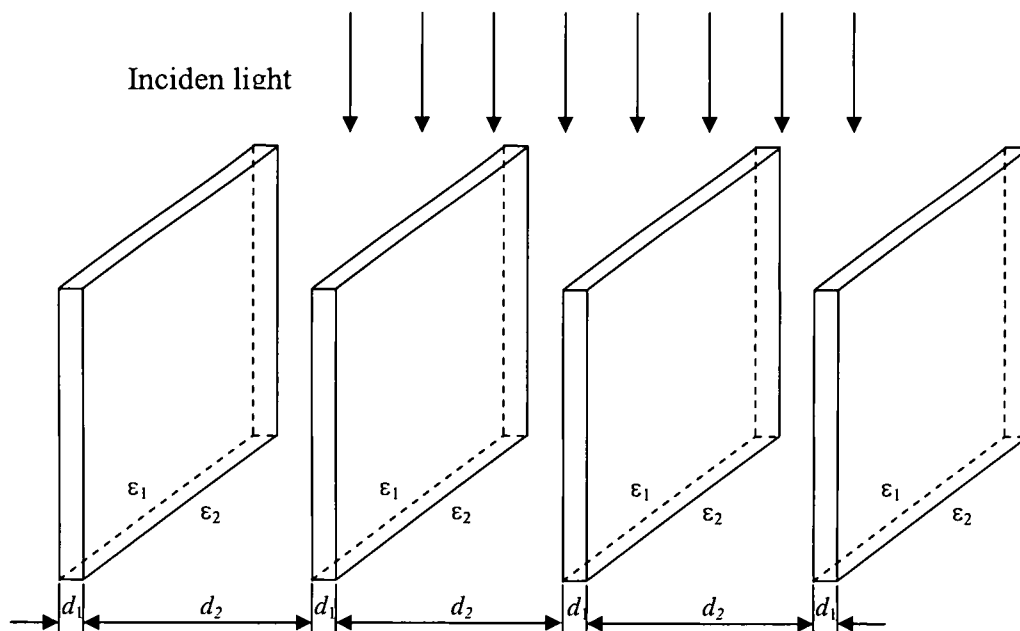


Fig. 6-1. A regular assembly of thin parallel plates.

Suppose first that a plane monochromatic wave is incident on the assembly from the top and assume that its electric vector is perpendicular to the plates. In this case, the normal component of the electric displacement must be continuous across a surface at which the properties of the medium change abruptly. Hence the electric displacement must have the same value D inside the plates and in the spaces. If E_1 and E_2 are the corresponding electric fields,

$$E_1 = \frac{D}{\epsilon_1}, \quad E_2 = \frac{D}{\epsilon_2}, \quad (6-1)$$

and the mean field E averaged over the total volume is

$$E = \frac{d_1 \frac{D}{\epsilon_1} + d_2 \frac{D}{\epsilon_2}}{d_1 + d_2}. \quad (6-2)$$

The effective dielectric constant ϵ_{\perp} is, therefore,

$$\epsilon_{\perp} = \frac{D}{E} = \frac{(d_1 + d_2)\epsilon_1\epsilon_2}{d_1\epsilon_2 + d_2\epsilon_1} = \frac{\epsilon_1\epsilon_2}{F_1\epsilon_2 + F_2\epsilon_1}, \quad (6-3)$$

where $F_1 = d_1/(d_1+d_2)$, $F_2 = d_2/(d_1+d_2) = 1-F_1$ are the fractions of the total volume occupied by the plates and by the surrounding medium respectively.

Suppose next that the incident field has its electric vector parallel to the plates. In this case the electric field will have the same value E inside the plates and in the spaces. The electric displacements in the two regions become

$$D_1 = \epsilon_1 E, \quad D_2 = \epsilon_2 E, \quad (6-4)$$

so that the mean electric displacement D is

$$D = \frac{d_1\epsilon_1 E + d_2\epsilon_2 E}{d_1 + d_2}. \quad (6-5)$$

Hence the effective dielectric constant ϵ_{\parallel} is now given by,

$$\epsilon_{\parallel} = \frac{D}{E} = \frac{d_1\epsilon_1 + d_2\epsilon_2}{d_1 + d_2} = F_1\epsilon_1 + F_2\epsilon_2, \quad (6-6)$$

Since the effective dielectric constant is the same for all directions parallel to the plates, but different for directions normal to the plates, the assembly behaves as a uniaxial crystal with its optic axis perpendicular to the plane of the plates. The difference $\epsilon_{\parallel} - \epsilon_{\perp}$ is always positive, since according to (6-3) and (6-6),

$$\epsilon_{\parallel} - \epsilon_{\perp} = \frac{F_1 F_2 (\epsilon_1 - \epsilon_2)^2}{F_1 \epsilon_2 + F_2 \epsilon_1} \geq 0. \quad (6-7)$$

The ordinary wave has its electric vector perpendicular to the optic axis, i.e. parallel to the plane of the plates. Equation (6-7) implies that the assembly always behaves like a negative uniaxial crystal. In terms of refractive indices the last equation may be written as

$$n_e^2 - n_o^2 = -\frac{F_1 F_2 (n_1^2 - n_2^2)^2}{F_1 n_2^2 + F_2 n_1^2}. \quad (6-8)$$

For assemblies of particles of less idealized forms the calculations are naturally more complicated.

A case of considerable practical interest is that of an assembly of parallel and similar thin cylindrical rods. It was shown by Wiener [45] that if the rods occupy a small fraction of the total volume ($F_1 \ll 1$), one has, in place of (6-8),

$$n_e^2 - n_o^2 = \frac{F_1 F_2 (n_1^2 - n_2^2)^2}{(1 + F_1) n_2^2 + F_2 n_1^2}. \quad (6-9)$$

Such an assembly therefore behaves as a positive uniaxial crystal, with its optic axis parallel to the axes of the rods.

To distinguish between form birefringence and intrinsic birefringence of the material of the particles, the refractive index n_2 of the medium is varied; the form birefringence will disappear when $n_2 = n_1$, while intrinsic birefringence will be unaffected by a variation of n_2 .

6.3 Schematic diagram of a form birefringence layer

Ge and ZnS were chosen for the layer structure because of their low absorption coefficients in the long wave-infrared region, and the relative ease with which they can be deposited. The refractive indices of Ge and ZnS as found in Refs. [46] and [47] respectively, were used in the EMT and RCWA calculations reported in this chapter. As shown in Fig. 6-2, these parameters include the grating period, Λ , fill factor, $F_f = a/\Lambda$, and thickness, d .

The extent of the polarization rotation depends on the index contrast between the TE and TM waves, which in turn depends on the index contrast between the two materials (Ge and ZnS) that make up the form birefringence layer. For this application, a phase retardation of 45 degrees over the 8 to 12 μm wavelength range is desired. After each round trip around the cavity, the net phase retardation will be 90 degrees, which will transform the TE into TM and vice versa. The 45 degree phase retardation is not critical to the design. Smaller phase retardations can be made up for by a larger number of round trips around the cavity.

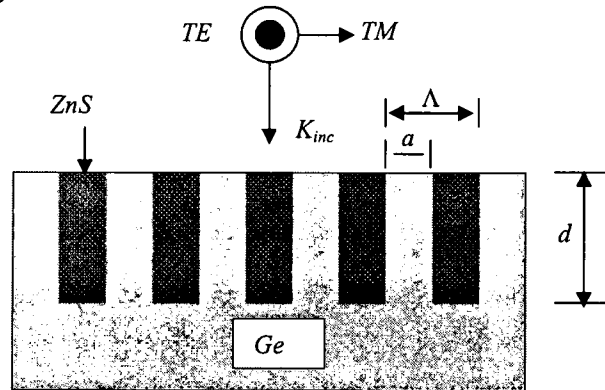


Fig. 6-2. Schematic diagram of a form birefringence layer.

6.4 Second-order effective medium theory (EMT)

As mentioned in section 6.2, the effective refractive indices n_{\parallel} and n_{\perp} for the TE and TM polarizations are

$$n_{\parallel} = [Fn_1^2 + (1-F)n_2^2]^{1/2}, \quad (6-10a)$$

$$n_{\perp} = [Fn_1^{-2} + (1-F)n_2^{-2}]^{-1/2}. \quad (6-10b)$$

where F is the duty cycle of the grating and n_1 and n_2 are the refractive indices of the two materials composing the grating. This is the so called zero-order effective medium theory (EMT). However, for a more accurate analysis, the second-order EMT developed by Rytov [43] is introduced. According to the second-order EMT, the effective refractive indices n_{\parallel} and n_{\perp} can be written as

$$n_{\parallel}^{(2)} = \left[n_{\parallel}^2 + \frac{1}{3} \left(\frac{\Lambda}{\lambda} \right)^2 \pi^2 F^2 (1-F)^2 (n_2^2 - n_1^2)^2 \right]^{1/2}, \quad (6-11a)$$

$$n_{\perp}^{(2)} = \left[n_{\perp}^2 + \frac{1}{3} \left(\frac{\Lambda}{\lambda} \right)^2 \pi^2 F^2 (1-F)^2 \left(\frac{1}{n_2^2} - \frac{1}{n_1^2} \right)^2 n_{\parallel}^2 n_{\perp}^6 \right]^{1/2}. \quad (6-11b)$$

where Λ is the grating period and λ is the wavelength of the incident wave.

With the simple model of multiple reflections between the two boundaries of a homogeneous layer and the Fresnel formulas for transmission and reflection coefficients at the superstrate-layer and layer-substrate interfaces, the phase retardation between the transmitted TE and TM polarizations in normal incidence is found as [48]

$$\Delta\psi = \arg \left[n_{\parallel} (n_1 + n_2) \cos \left(\frac{2\pi}{\lambda} n_{\parallel} d \right) + j (n_1 n_2 + n_{\parallel}^2) \sin \left(\frac{2\pi}{\lambda} n_{\parallel} d \right) \right] - \arg \left[n_{\perp} (n_1 + n_2) \cos \left(\frac{2\pi}{\lambda} n_{\perp} d \right) + j (n_1 n_2 + n_{\perp}^2) \sin \left(\frac{2\pi}{\lambda} n_{\perp} d \right) \right]. \quad (6-12)$$

where j is the imaginary unit.

To validate the above methods, simulations using EMT were performed. Figs. 6-3, -4 show the phase retardation as a function of grating thickness and duty cycle. These are exactly the same as Fig. 4 (a) and Fig. 5 (a) from Ref. [49]. This simulation was performed to validate and confirm the model before conducting simulations on the proposed work.

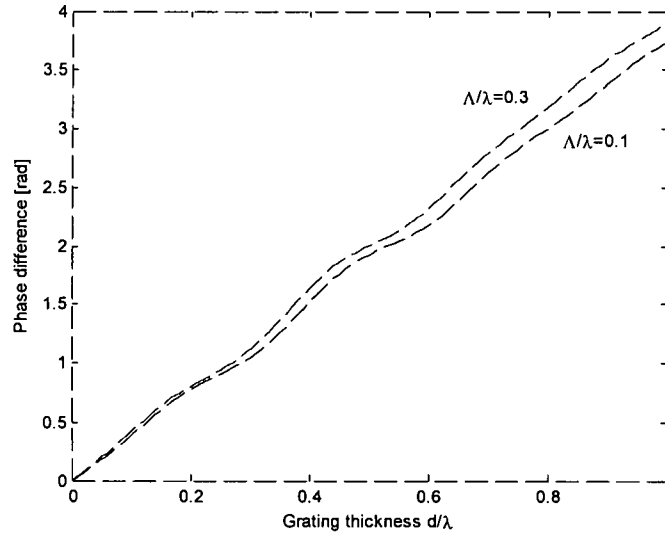


Fig. 6-3. Phase retardation between TE- and TM- polarized light as a function of a normalized thickness rectangular-shaped grating of 50% duty cycle using second-order EMT.

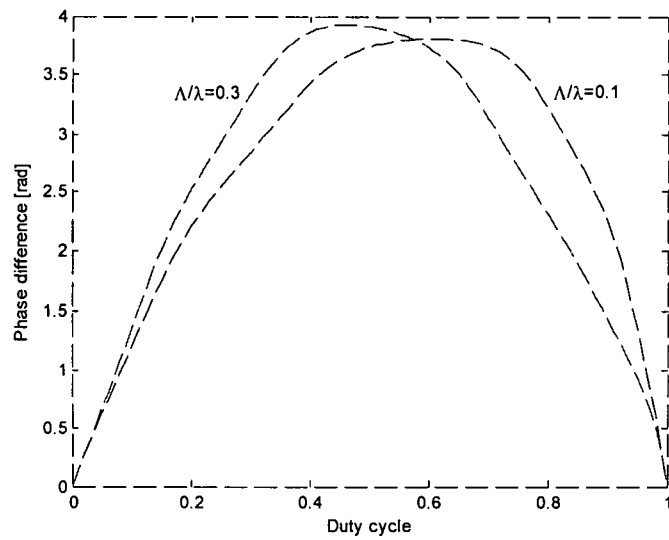


Fig. 6-4. Phase retardation between TE- and TM- polarized light as a function of a rectangular-shaped grating duty cycle with $d/\lambda = 1.0$ and Λ/λ as a parameter using second-order EMT.

6.5 Rigorous coupled wave analysis (RCWA)

The rigorous coupled wave analysis (RCWA) for a dielectric surface-relief (or corrugated) gratings was first introduced by Moharam *et al.*[50] in 1982. It has been used to analyze the diffraction properties of TE polarized light in lossless surface-relief gratings. A schematic diagram for the dielectric surface-relief grating diffraction is depicted in Fig. 6-5.

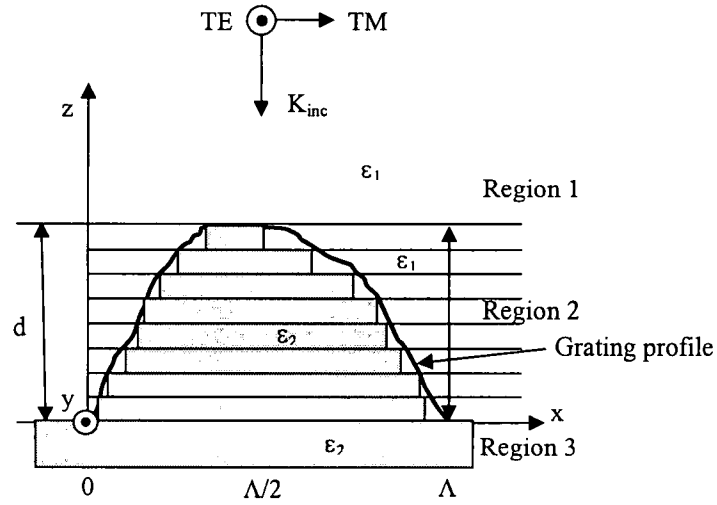


Fig. 6-5. Geometry of dielectric surface-relief grating.

The periodic structure produces forward-diffracted waves and backward-diffracted waves. Region 1 is a homogeneous dielectric with a relative permittivity of ϵ_1 . In the same way, region 3 is homogeneous with a relative permittivity of ϵ_2 . Region 2 is a grating region, and consists of a periodic distribution of both types of dielectrics. The boundary between the ϵ_1 and ϵ_2 in region 2 can be written as

$$z = F(x) = F(x + \Lambda), \quad (6-13)$$

where Λ is the grating period. The function $F(x)$ thus represents the grating-surface profile.

The total electric field in region 1 is the sum of the incident and the backward-traveling waves, and may be expressed as

$$E_1 = \exp(-j\mathbf{k}_1 \cdot \mathbf{r}) + \sum_{i=-\infty}^{\infty} R_i \exp(-j\mathbf{k}_{1i} \cdot \mathbf{r}), \quad (6-14)$$

where $j = (-1)^{1/2}$, \mathbf{k}_1 is the incident-field wave vector of magnitude, $k_1 = 2\pi(\epsilon_1)^{1/2} / \lambda$, λ is the free-space wavelength, and $\mathbf{r} = x\hat{x} + y\hat{y} + z\hat{z}$, with $\hat{}$ denoting a unit vector. R_i is the normalized amplitude of the i th reflected wave in region 1 with wave vector \mathbf{k}_{1i} . Likewise, the normalized total electric field in region 3 is

$$E_3 = \sum_{i=-\infty}^{\infty} T_i \exp[-j\mathbf{k}_{3i} \cdot (\mathbf{r} - d\hat{z})], \quad (6-15)$$

where T_i is the normalized amplitude of the i th transmitted wave into region 3 with wave vector \mathbf{k}_{3i} and d is the groove depth. The quantities \mathbf{k}_{1i} and \mathbf{k}_{3i} are determined below by using the phase-matching requirement.

The region 2, which is grating region, is divided into N thin planar-grating slabs perpendicular to the z axis. Then the rigorous coupled-wave analysis that has been developed for planar gratings is applied to each slab grating [51]. If the individual planar gratings are sufficiently thin, any grating profile can be analyzed to an arbitrary level of accuracy. The n th slab within region 2 as shown in Fig. 6-5 will consist of a periodic distribution of ϵ_1 and ϵ_2 dielectrics. The relative permittivity for the n th slab grating is periodic,

$$\epsilon_n(x, z_n) = \epsilon_n(x + \Lambda, z_n), \quad (6-16a)$$

and may be expanded in a Fourier series as

$$\epsilon_n(x, z_n) = \epsilon_1 + (\epsilon_2 - \epsilon_1) \sum_{h=-\infty}^{\infty} \tilde{\epsilon}_{h,n} \exp(jhKx), \quad (6-16b)$$

where z_n is the z coordinate of the n th slab, h is the harmonic index, K is the magnitude of the grating vector and $\tilde{\varepsilon}_{h,n}$ are the normalized complex harmonic amplitude coefficients given by

$$\tilde{\varepsilon}_{h,n} = \left(\frac{1}{\Lambda} \right) \int_0^\Lambda f(x, z_n) \exp(-jhKx) dx, \quad (6-17)$$

where the function $f(x, z_n)$ is equal to either zero or unity, depending on whether, for a particular value of x , the grating relative permittivity is ε_1 or ε_2 , respectively.

The fields inside each grating slab are expanded in terms of the space harmonics of the fields in the periodic structure. These space harmonics inside the grating correspond to diffracted orders outside the grating. Thus the partial fields inside the modulated medium are visualized as diffracted waves that progress through the planar slab and couple energy back and forth between each other as they progress. In the coupled-wave approach the total field is thus expressed as

$$E_{2,n} = \sum_{i=-\infty}^{\infty} S_{i,n}(z) \exp(-j\sigma_{i,n} \cdot \mathbf{r}), \quad (6-18)$$

where i is the space-harmonic index (index) and $S_{i,n}(z)$ are the space-harmonic field amplitudes. As a result of the Floquet theorem, the diffracted wave vectors inside the n th grating, $\sigma_{i,n}$, may be represented by

$$\sigma_{i,n} = \mathbf{k}_{2,n} - i\mathbf{K}, \quad (6-19)$$

where $\mathbf{K} = K\hat{x}$ and $\mathbf{k}_{2,n}$ is the wave vector of the zero-order ($i = 0$) refracted wave having a magnitude of $k_{2,n} = 2\pi(\varepsilon_{0,n})^{1/2} / \lambda$, and $\varepsilon_{0,n}$ is the average relative permittivity for the n th slab grating.

Each i th diffracted field in regions 1 and 3 must be phase matched to the i th space-harmonic field inside each n th slab grating. Thus

$$\mathbf{k}_{1i} \cdot \hat{\mathbf{x}} = (\mathbf{k}_{2,n} - i\mathbf{K}) \cdot \hat{\mathbf{x}} = \mathbf{k}_{3i} \cdot \hat{\mathbf{x}}, \quad (6-20)$$

for any i and n . In the homogeneous regions (1 and 3) the backward- and forward-diffracted waves have wave vectors with magnitudes

$$|\mathbf{k}_{1i}| = |\mathbf{k}_1| \quad \text{and} \quad |\mathbf{k}_{3i}| = |\mathbf{k}_3|, \quad (6-21)$$

where $k_3 = 2\pi(\epsilon_2)^{1/2} / \lambda$. Knowing the total amplitudes and the x components are then determined to be

$$\mathbf{k}_{1i} \cdot \hat{\mathbf{z}} = \left[|\mathbf{k}_1|^2 - (\mathbf{k}_{1i} \cdot \hat{\mathbf{x}})^2 \right]^{1/2}, \quad (6-22a)$$

$$\mathbf{k}_{3i} \cdot \hat{\mathbf{z}} = \left[|\mathbf{k}_3|^2 - (\mathbf{k}_{3i} \cdot \hat{\mathbf{x}})^2 \right]^{1/2}. \quad (6-22b)$$

Therefore the total fields in all regions may be rewritten as

$$E_1 = \exp\{-j[k_1(\sin\theta x + \cos\theta z)]\} + \sum_{i=-\infty}^{\infty} R_i \exp\{-j[(k_1 \sin\theta - iK)x - [k_1^2 - (k_1 \sin\theta - iK)^2]^{1/2} z]\}, \quad (6-23a)$$

$$E_{2,n} = \sum_{i=-\infty}^{\infty} S_{i,n}(z) \exp\{-j[(k_1 \sin\theta - iK)x + (k_{2,n}^2 - k_1^2 \sin^2\theta)^{1/2} z]\}, \quad (6-23b)$$

$$E_3 = \sum_{i=-\infty}^{\infty} T_i(z) \exp\{-j[(k_1 \sin\theta - iK)x + [k_3^2 - (k_1 \sin\theta - iK)^2]^{1/2} (z-d)]\}. \quad (6-23c)$$

where θ is the angle of incidence.

In region 2, the wave equation for TE polarized light

$$\nabla^2 E_{2,n} + k^2 \epsilon_n(x, z_n) E_{2,n} = 0, \quad (6-24)$$

must be satisfied for each n th slab grating. Substituting $\varepsilon_n(x, z_n)$ from Eq. (6-16b) and $E_{2,n}$ from Eq. (6-23b) into the wave equation, performing the indicated differentiations, and setting the coefficient of each exponential term equal to zero for nontrivial solutions yields the rigorous coupled-wave equations for the n th slab grating:

$$\begin{aligned} \frac{d^2 S_{i,n}(z)}{dz^2} - j2(k_{2,n}^2 - k_1^2 \sin^2 \theta)^{1/2} \frac{dS_{i,n}(z)}{dz} + K^2 i(m - i)S_{i,n}(z) \\ + k^2(\varepsilon_2 - \varepsilon_1) \sum_{h=1}^{\infty} [\tilde{\varepsilon}_{h,n} S_{i-h,n}(z) + \tilde{\varepsilon}_{h,n}^* S_{i+h,n}(z)] = 0. \end{aligned} \quad (6-25)$$

Eq. (6-25) is the rigorous coupled-wave equations. These form an infinite set of second-order coupled difference-differential equations. Each diffracted wave (i) is coupled to other diffracted waves through the harmonics of the grating ($i - h$ and $i + h$). The quantity m has been defined as

$$m = 2\Lambda \sqrt{\varepsilon_1} \sin \theta / \lambda. \quad (6-26)$$

This represents a Bragg condition if m is an integer.

The case of TM light polarization was treated in a similar manner, with the proper wave equation used for this polarization and the coupled-wave equations modified for the case of a surface-relief grating [52].

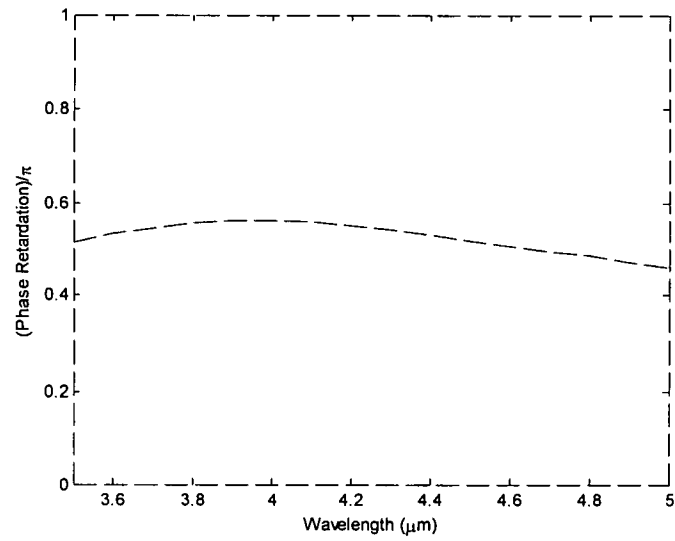


Fig. 6-6. Simulated phase retardation as a function of wavelength using RCWA.

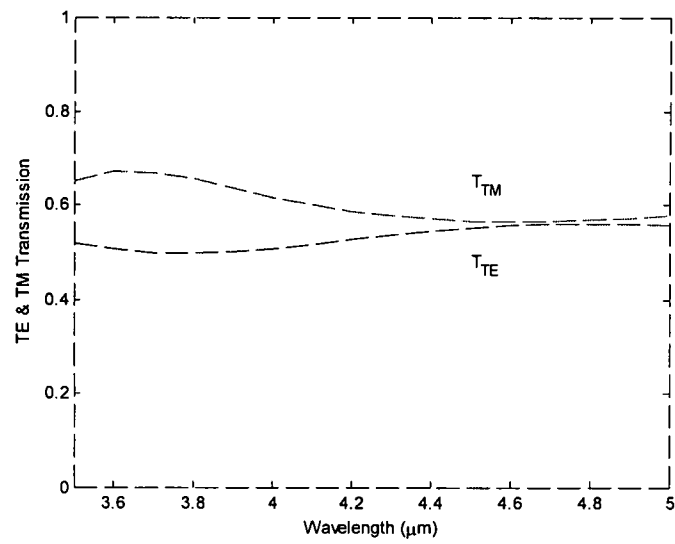


Fig. 6-7. Simulated TE and TM transmission as a function of wavelength using RCWA.

Again, to validate the above methods, simulations using RCWA was accomplished. Figs. 6-6, -7 show the phase retardation and TE & TM transmission coefficients as a function of wavelength. These are exactly same as the Fig. 5 (a), - (b) shown in Ref. [53]. Both EMT and RCWA methods have thus been validated and ready for use for the proposed device configuration.

6.6 Numerical simulation and comparison

A grating period of $1\text{ }\mu\text{m}$ was used for all simulations because that is the longest period that will not produce any higher order diffractions (losses). Only the zero-order diffraction will be present. Fig. 6-8 shows the phase retardation at $d = 2.2\text{ }\mu\text{m}$ as a function of the grating duty cycle. As it can be seen, the phase retardation for different duty cycles is not symmetrical, and its maximum value is located around 50% duty cycle in both EMT and RCWA cases. As a result, we chose 50% as the design duty cycle for all the following simulations.

The phase retardation as a function of the grating layer thickness at $\lambda = 8.25\text{ }\mu\text{m}$ with 50% duty cycle is shown in Fig. 6-9. It can be seen that a film thickness of $2.2\text{ }\mu\text{m}$ is required to achieve the desired phase retardation of 45 degrees. Fig. 6-10 depicts the phase retardation as a function of wavelength at $2.2\text{ }\mu\text{m}$ thickness with 50% duty cycle using EMT and RCWA methods. The phase retardation is around 18 degrees between $8\text{ }\mu\text{m}$ and $12\text{ }\mu\text{m}$ wavelengths for both EMT and RCWA methods. It should be mentioned

that the 45 degree phase retardation is required only in the case where a photon makes one round-trip around the cavity. If the photon is able to make more round-trips, smaller phase retardation would be sufficient. In other words, the required phase retardation depends on the quality factor (Q) of the resonator. However, a detailed analysis of cavity Q vs phase retardation was not been conducted for this work. Hence, for the purposes of this simulation, 45 degree phase retardation has been assumed.

Dependence on the angle of incidence of the form birefringence layer has also been simulated using EMT and RCWA. Fig. 6-11 depicts the phase retardation for the 50% duty cycle form birefringence layer at 2.2 μm thickness as a function of incident angle. As can be seen, the EMT and RCWA results follow the same functional behavior in that the phase retardation decreases for increasing incident angles. Nevertheless, the phase retardation remains almost a constant, i.e. less than 3% degradation in the range of 0° - 15° . This angular behavior needs to be accounted for in RCE-CQWIP designs when operating at larger angles of incidence. The angle of incidence would depend on the numerical aperture of the optics used in front of the detector.

Comparing the results shown in Figs. 6-8, -9, -10, and -11, it is observed that the values obtained by the EMT are always higher than those obtained by the RCWA. Although the RCWA method is generally believed to be more accurate, the average between EMT and RCWA is chosen as a reasonable estimate for the following simulations.

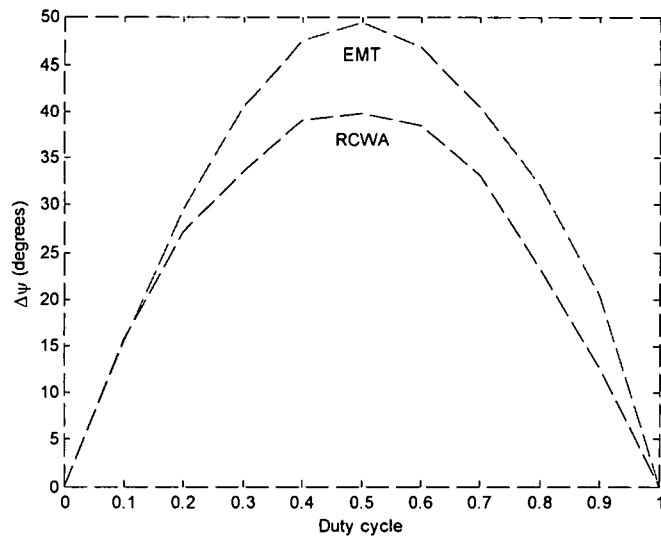


Fig. 6-8. Phase retardation between TE and TM polarized light as a function of a grating duty cycle.

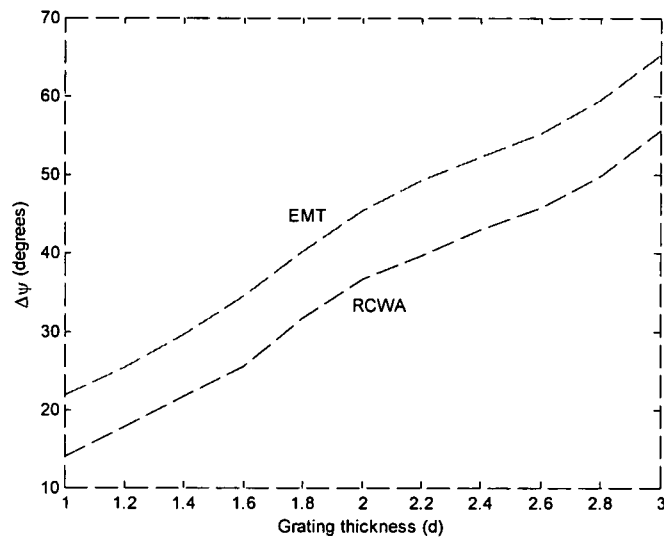


Fig. 6-9. Phase retardation as a function of grating thickness.

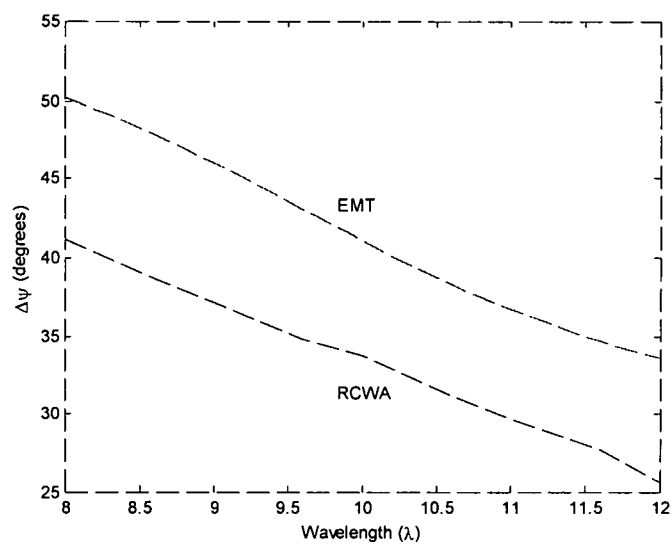


Fig. 6-10. Phase retardation as a function of wavelength at $d = 2.2 \mu\text{m}$.

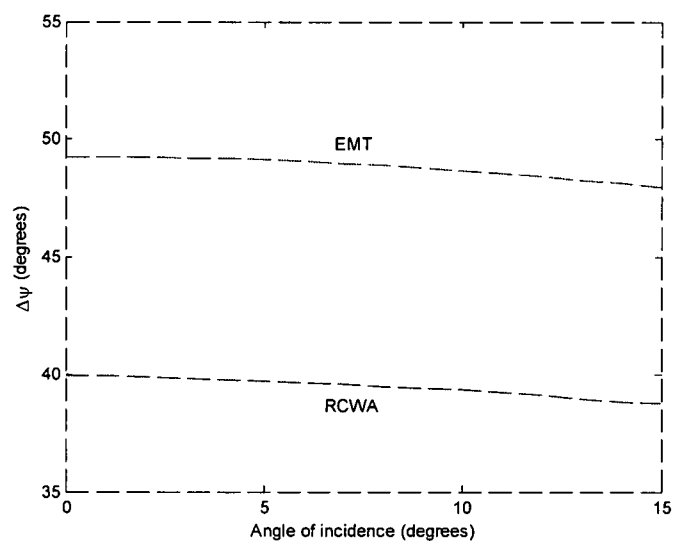


Fig. 6-11. Phase retardation as a function of angle of incidence at $d = 2.2 \mu\text{m}$.

6.7 Schematic diagram of RCE-CQWIP with a form birefringence layer

Fig. 6-12 illustrates the details of the schematic diagram of the proposed schematic diagram of RCE-CQWIP with a form birefringence layer. The structure is exactly the same as Fig. 5-1 except for this extra layer.

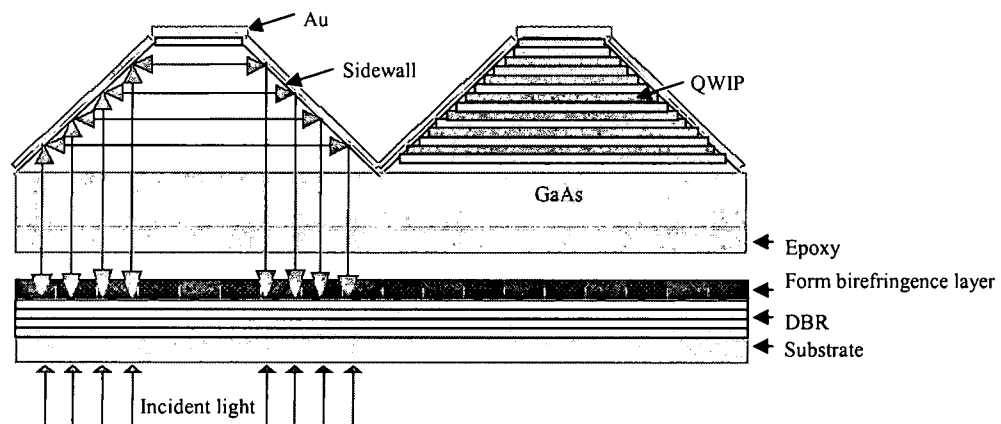


Fig. 6-12. Schematic diagram of RCE-CQWIP using form birefringence technique.

The DBR stacks for this device were designed with 2 pairs of Ge/ZnS to create the resonance along the upper sidewalls, assuming they reflect nearly 100% due to TIR. Again, the same refractive indices for Ge and ZnS as in section 6.3 were applied.

6.8 Simulation results and discussion

The resonant wavelength needs to be determined before conducting a detailed simulation of quantum efficiency. The RCE-CQWIP was simulated as a function of thickness of epoxy (Fig. 6-13) and depth of the form birefringence layer (Fig. 6-14) in a similar fashion to the previous chapter. The QE has a maximum value at 1.2 μm of the thickness of epoxy. With those parameters, the analysis could be continued assuming the cavity to be in a resonant condition.

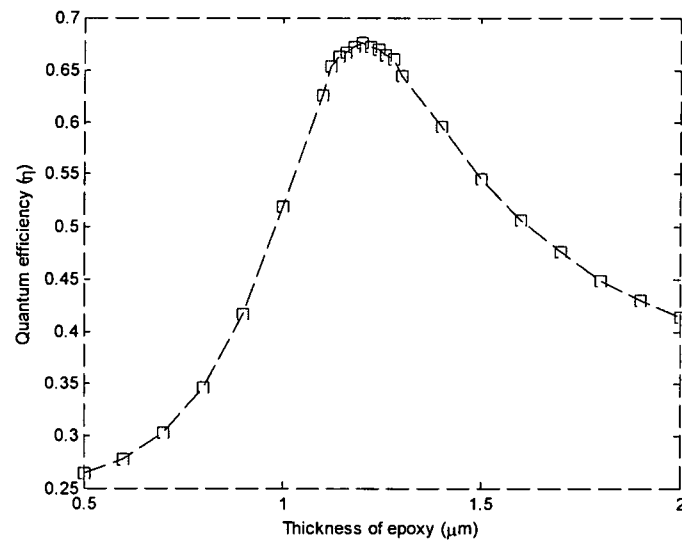


Fig. 6-13. Quantum efficiency vs. thickness of epoxy.

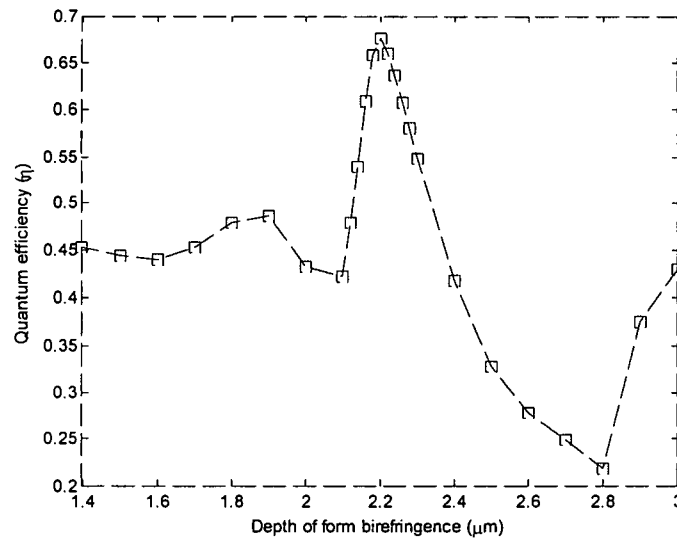


Fig. 6-14. Quantum efficiency in terms of depth of a form birefringence layer.

The calculated quantum efficiency as a function of wavelength in the C-QWIP and RCE-CQWIP with a form birefringence layer is shown in Fig. 6-15. It has a maximum value at $\lambda = 8.25 \mu\text{m}$ in both cases since the structures have been designed for that wavelength. However, the peak QE in RCE-CQWIP with a form birefringence layer is much higher than the peak value of C-QWIP. This demonstrates that the QE in RCE-CQWIP with a form birefringence layer has been enhanced up to 38% over the C-QWIP at the resonant wavelength.

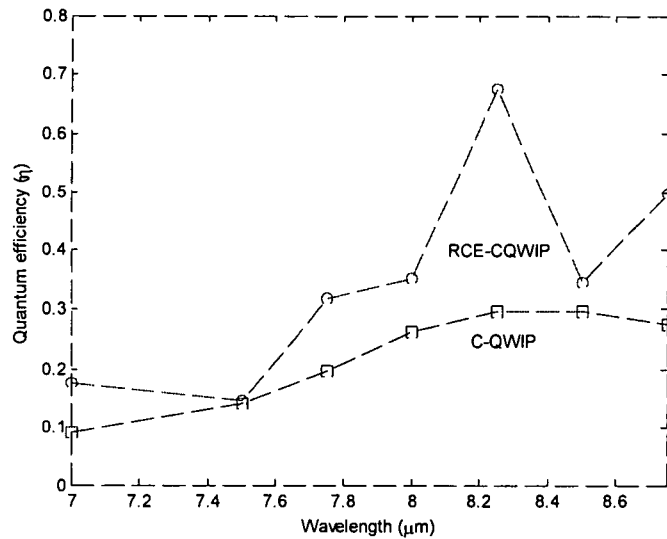


Fig. 6-15. Quantum efficiency as a function of wavelength.

As done previously with the RCE-CQWIP, it is important to also examine the angular dependency in RCE-CQWIP with a form birefringence layer. This is shown in Fig. 6-16. The inset in Fig. 6-16 shows the QE degradation for TE and TM waves. It was found that QE degrades by less than 1% when the angle is less than 4° . This implies that the angular dependence of the detector performance is not too large to become a serious practical limitation, and the structure should be able to accommodate a range of focusing optics and F-numbers. Notice also that the QE for TM waves increases with angle as discussed in section 5.3. One contribution to this behavior is due to the fact that the zero-order diffraction efficiency of TM waves increases as angle of incidence increases as shown in Fig 6-17. On the other hand, TE waves are not being absorbed even though they travel through the quantum wells at an angle since there is no electric field component perpendicular to the quantum well layers. TE waves, however, change the propagation

direction at the sidewalls; hence absorption starts to take place. In addition, the zero-order diffraction efficiency of TE waves decreases as evident in Fig. 6-17.

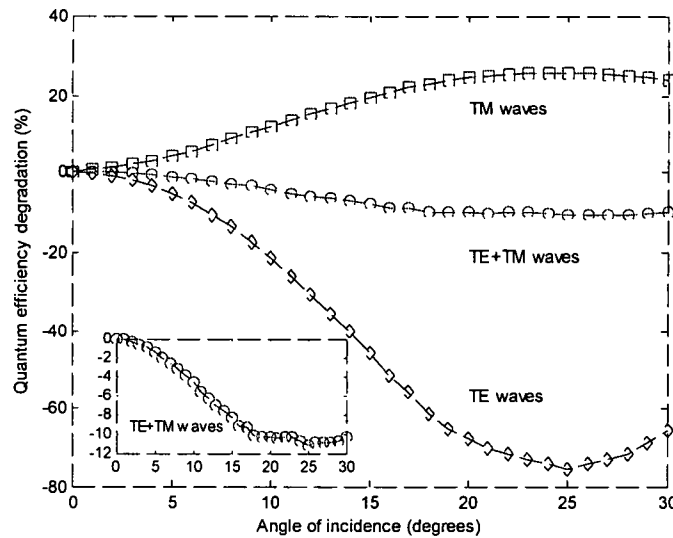


Fig. 6-16. The dependence of quantum efficiency on the angle of incidence.

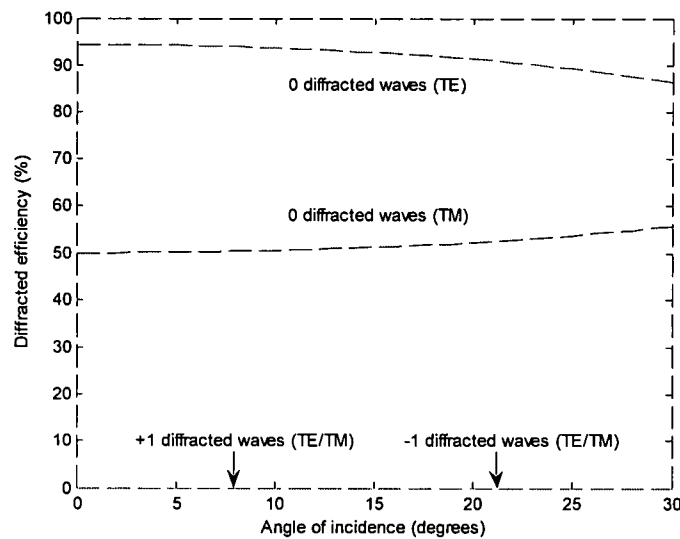


Fig. 6-17. The diffraction efficiencies of the transmitted waves for a form birefringence layer.

6.9 Conclusion

In this chapter, the RCE-CQWIP with a form birefringence layer was designed and simulated. Simulation results for the form birefringence layer and for the RCE-CQWIP are demonstrated using EMT/RCWA and the FDTD methods, respectively. A ZnS film thickness of 2.2 μm is required to achieve a phase retardation of 45 degrees. FDTD simulation results show that QE of 68% with a form birefringence layer can be achieved using this novel design approach.

Dependence of QE on the angle of incidence is also discussed. It was found that QE degrades by less than 1% for angles less than 4° in the RCE-CQWIP with a form birefringence layer. This implies that the angular dependence of the detector performance is not too large to become a serious practical limitation, and the structure should be able to accommodate a range of focusing optics and F-numbers.

CHAPTER VII

CONCLUSIONS

In this dissertation, the resonant cavity enhancement technique for improving the quantum efficiency (QE) of photodetectors, including QWIPs and C-QWIPs was studied. QE is the key parameter that determines the overall performance of a photodetector. Hence, an improvement in QE can result in better noise performance, higher speeds and allow the devices to be operated at higher temperatures with lower dark currents.

In chapter II, a review of related research was conducted. Numerical methods such as the finite difference time domain (FDTD) method and the transfer matrix method (TMM) have been developed to carry out a rigorous analysis of RCE structures. These are powerful tools for the analysis of most resonant cavity structures.

To validate these numerical methods, previously published analytical expressions for QE were confirmed using the FDTD and TMM approaches. There were minor discrepancies between the FDTD (also with TMM) results and the results reported in the literature. This is due to the more accurate consideration of the refractive indices at each layer in the FDTD method. The FDTD model was also developed to include the diffraction from the

grating, and was examined for its angular dependency. Due to the flexibility, accuracy and the least number of approximations contained in the formulation, the FDTD method was finally selected as the simulation tool for conducting the research presented in this dissertation.

A determination of temperature-dependent refractive index of $\text{Al}_x\text{Ga}_{1-x}\text{As}$ material is developed in chapter III. Although $\text{Al}_x\text{Ga}_{1-x}\text{As}$ is a well-matured material for optoelectronics, its temperature-dependent refractive indices are not well known. Experiments were performed in the range of $1.46 \sim 1.58 \mu\text{m}$ and $26 \sim 86^\circ\text{C}$ and a modified Sellmeier equation was derived in chapter III. This equation might also be applied to wavelengths and temperatures outside this range because the refractive index varies almost linearly with wavelength.

The grating-coupled quantum well infrared photodetector (QWIP) and the corrugated quantum well infrared photodetector (C-QWIP) were investigated in chapter IV and chapter V, respectively, and were simulated using FDTD method. Although QWIPs have potential use in infrared imaging, they still lag behind mercury cadmium telluride (HgCdTe) detectors primarily due to their low QE.

In order to increase QE, the RCE approach was extended to include both the QWIP and C-QWIP devices, which will be referred to as RCE-QWIP and RCE-CQWIP, respectively. FDTD simulations for both structures show that QE can be enhanced up to 60% and 38% in RCE-QWIP and in RCE-CQWIP, respectively.

Dependence of QE on the angle of incidence in the RCE photodetector, RCE-QWIP, RCE-CQWIP and RCE-CQWIP with a form birefringence layer is also analyzed. It was found that QE degrades by less than 1% for angles less than 5° , 3° , and 4° in RCE photodetector, RCE-CQWIP and RCE-CQWIP with a form birefringence layer, respectively. This implies that the angular dependence of the detector performance is not too large to become a serious practical limitation, and the structure should be able to accommodate a range of focusing optics and F-numbers.

RECOMMENDATIONS FOR FUTURE WORK

Although the analysis on the form birefringence layer in RCE-CQWIP has been completed using EMT and RCWA methods, the next step is to carry out the experimental research to evaluate its applicability. Experiments to validate the polarization rotation effect should not be too difficult to conduct and could be completed with a modest setup. An infrared emitter can be used as the light source, and transmitted light passing through a sample can be measured by pyro-electric detector along with a lock-in amplifier. The phase retardation between the TE and TM waves can be calculated by using the Jones Matrix methods. Fortunately, similar experiments on different materials and spectral range, mostly near the infrared band, have been reported. The Ge/ZnS thin films can be sputter deposited, and patterned using photo lithography, and eventually etched using a plasma reactor. The facilities to perform all these steps are currently available in our laboratory. It is anticipated that this work will be completed in the near future.

BIBLIOGRAPHY

- [1] C. R. Pollock, "Fundamentals of Optoelectronics," Irwin, 1995.
- [2] K. Kishino, M. S. Unlu, J. I. Chyi, J. Reed, L. Arsenault, H. Morkoc, "Resonant Cavity-Enhanced (RCE) Photodetectors," IEEE J. Quantum Electron. QE-27, No. 8 August 1991.
- [3] F. Y. Huang, A. Salvador, X. Gui, N. Teraguchi, and H. Morkoc, "Resonant-cavity GaAs/InGaAs/AlAs photodiodes with a periodic absorber structure," Appl. Phys. Lett. Vol. 63, No. 2, July 1993.
- [4] A. Srinivasan, S. Murtaza, J. C. Campbell, and B. G. Streetman, "High quantum efficiency dual wavelength resonant-cavity photodetector," Appl. Phys. Lett. Vol. 66, No. 5, January 1995.
- [5] B. Temelkuran, E. Ozbay, J. P. Kavanaugh, G. Tuttle, and K. M. Ho, "Resonant cavity enhanced detectors embedded in photonic crystals," Appl. Phys. Lett. Vol. 72, No. 19, May 1998.
- [6] Y. H. Zhang, H. T. Luo, and W. Z. Shen, "Study on the quantum efficiency of resonant cavity enhanced GaAs far-infrared detectors," J. Appl. Phys. Vol. 91, No. 9, May 2002.
- [7] M. Born, E. Wolf, Principles of Optics (Pergamon Press, Oxford, U. K., 1980).

- [8] M. S. Unlu, S. Strite, "Resonant cavity enhanced photonic devices," J. Appl. Phys., Vol. 78, No. 2, 15 July 1995.
- [9] M. Yamada, K. Sakuda, "Analysis of almost-periodic distributed feedback slab waveguides via fundamental matrix approach," Appl. Opt., Vol. 26, Aug. 1987.
- [10] W. P. Huang, "Methods for Modeling and Simulation of Guided-Wave Optoelectronic Devices," EMW publishing, Massachusetts, USA, 1995.
- [11] M. J. O'Hare, R. J. Brecha, "Optical Radiation and Matter class notes," EO program, University of Dayton, 2001.
- [12] H. S. Nalwa, "Photodetectors and Fiber Optics," Academic Press, London, UK, 2001.
- [13] D. M. Gvozdic, P. L. Nikolic, and J. B. Radunovic, "Optimization of a resonant cavity enhanced MSM photodetector," Semicond. Sci. Technol. **15**, 2000.
- [14] S. C. Hagness, R. M. Joseph, "Subpicosecond electrodynamics of distributed Bragg reflector microlasers: Results from finite difference time domain simulations," Radio Science, **31**, 931-941 (1996).
- [15] D. K. Cheng, *Field and Wave Electromagnetics* (Addison-Wesley, Menlo Park, 1992).
- [16] M. V. Hobden, J. Earner, "The temperature dependence of the refractive indices of pure lithium niobate," Phys. Lett. **22** (3), 1966, pp 243-244.
- [17] N. P. Barnes, M. S. Piltch, "Temperature-dependent Sellmeier coefficients and coherence length for cadmium telluride," J. Opt. Soc. Am., **67** (5), 1977, pp 628-629.
- [18] D. H. Jundt, "Temperature-dependent Sellmeier equation for the index of refraction, n_e , in congruent lithium niobate," Opt. Lett. **22** (20), 1997, pp 1553-1555.

- [19] A. Bruner, D. Eger, M. B. Oron, P. Blau, and M. Katz, "Temperature-dependent Sellmeier equation for the refractive index of stoichiometric lithium tantalate," *Opt. Lett.* **23**, (3), 2003, pp 194-196.
- [20] H. Y. Shen, X. L. Meng, G. Zhang, J. J. Qin, W. Liu, L. Zhu, C. H. Huang, L. X. Huang, M. Wei, "Sellmeier's equation and the expression of the thermal refractive-index coefficient for a $\text{Nd}_{0.007}\text{Gd}_{0.993}\text{VO}_4$ crystal," *Appl. Opt.* **43** (4), 2004, pp 955-960.
- [21] J. T. Boyd, "Theory of Parametric Oscillation Phase Matched in GaAs Thin-Film Waveguides," *IEEE J. Quant. Electronic.* **8** (10), 1972, pp 788-796.
- [22] M. Ettenberg, R. J. Paff, "Thermal Expansion of AlAs," *J. Appl. Phys.* **41** (10), 1970, pp 3926-3927.
- [23] S. Adachi, "GaAs, AlAs, and $\text{Al}_x\text{Ga}_{1-x}\text{As}$: Material parameters for use in research and device applications," *J. Appl. Phys.* **58** (3), 1985, pp R1-R29.
- [24] H. Kawai, S. Imanaga, K. Kaneko, N. Watanabe, "Complex refractive indices of AlGaAs at high temperatures measured by *in situ* reflectometry during growth by metalorganic chemical vapor deposition," *J. Appl. Phys.* **61** (1), 1986, pp 328-332.
- [25] G. Sarusi, B. F. Levine, S. J. Pearton, K. M. S. Bandara, R. E. Leibenguth, "Improved performance of quantum well infrared photodetectors using random scattering optical coupling," *Appl. Phys. Lett.*, **64**, 1994, pp 960.
- [26] J. Y. Andersson, L. Lundqvist, "Grating-coupled quantum-well infrared detectors: Theory and performance," *J. Appl. Phys.* Vol. 71, No. 7, 1 April 1992.
- [27] K. W. Goossen, S. A. Lyon, "Grating enhanced quantum well detector," *Appl. Phys. Lett.*, **47**, 1985, pp 1257.

- [28] Jang Pyo Kim, Andrew M. Sarangan, "Simulation of resonant cavity enhanced (RCE) photodetectors using the finite difference time domain (FDTD) method," *Optics Express*, Vol 12, No. 20, October 4, 2004.
- [29] J. Nelson, "Optical absorption in a quantum well, in *Low dimensional semiconductor structures: fundamentals and device applications*, K. Barnham and D. Vvedensky, ed. (Cambridge University Press, Cambridge, UK, 2001).
- [30] D. D. Coon, R. P. G. Karunasiri, "New mode of IR detection using quantum wells," *Appl. Phys. Lett.* **45** (6), 1984.
- [31] B. F. Levine, "Quantum-well infrared photodetectors," *J. Appl. Phys.*, **74**, R1-R81, 1993.
- [32] L. C. West, S. J. Eglash, "First observation of an extremely large-dipole infrared transition within the conduction band of a GaAs quantum well," *Appl. Phys. Lett.* **46** (12), 1985.
- [33] R. Petit, "Electromagnetic theory of gratings," Springer, Berlin, 1980.
- [34] A Taflove, "Computational Electrodynamics: The Finite Difference Time Domain," Artech House, Boston, 1995.
- [35] K. S. Kunz, R. J. Luebbers, "The Finite Difference Time Domain Method for Electromagnetics," CRC Press, Boca Raton, FL, 1993.
- [36] J. P. Berenger, "A perfectly matched layer for the absorption of electromagnetic waves," *J. Comput. Phys.*, **114**, 185-200, 1994.
- [37] D. M. Sullivan, "Electromagnetic simulation using the FDTD method," IEEE Press, New York, 2000.

- [38] J. T. Boyd, "Theory of Parametric Oscillation Phase Matched in GaAs Thin-Film Waveguides," IEEE J. Quant. Electronic. **8** (10), 1972, pp 788-796.
- [39] C. J. Chen, K. K. Choi, M. Z. Tidrow, and D. C. Tsui, "Corrugated quantum well infrared photodetectors for normal incident light coupling, " Appl. Phys. Lett. **68**, 1446 – 1448, 1996.
- [40] K. K. Choi, "The physics of quantum well infrared photodetectors," World Scientific, New Jersey, 1997.
- [41] A. Taflove, S. C. Hagness, "Computational electrodynamics: the finite-difference time-domain method," Artech House, Boston, 2000.
- [42] K. K. Choi, C. J. Chen, D. C. Tsui, "Corrugated quantum well infrared photodetectors for material characterization," J. Appl. Phys. **88**, 1612 – 1623, 2000.
- [43] S. M. Rytov, "Electromagnetic properties of a finely stratified medium," Sov. Phys. JETP **2**, 466 – 475 (1956).
- [44] M. G. Moharam, T. K. Gaylord, "Diffraction analysis of dielectric surface-relief gratings," J. Opt. Soc. Am. **72**, 1385 – 1392 (1982).
- [45] O. Wiener, *Abh. Sachs. Ges. Akad. Wiss., Math.-Phys. Kl. No. 6.* **32** (1912), 575.
- [46] E. D. Palik, "Handbook of optical constants of solids," Academic Press, San Diego, 1998.
- [47] D. T. F. Marple, "Refractive Index of ZnSe, ZnTe, and CdTe," J. Appl. Phys. **35**, 539-542, 1964.
- [48] N. Bokor, R. Shechter, N. Davidson, A. A. Friesem, E. Hasman, "Achromatic phase retarder by slanted illumination of a dielectric grating with period comparable with the wavelength," Appl. Opt. **40** (13), 2001, pp 2076-2080.

- [49] I. Ritcher, P. Sun, F. Xu, Y. Fainman, "Design considerations of form birefringent microstructures," *Appl. Opt.* **34** (14), 1995, pp 2421-2429.
- [50] M. G. Moharam, T. K. Gaylord, "Diffraction analysis of dielectric surface-relief gratings," *J. Opt. Soc. Am.* **72**, 1385-1392 (1982).
- [51] M. G. Moharam, T. K. Gaylord, "Rigorous coupled-wave analysis of planar grating diffraction," *J. Opt. Soc. Am.* **71**, 811-818 (1981).
- [52] M. G. Moharam, T. K. Gaylord, "Rigorous coupled-wave analysis of grating diffraction E-mode polarization and losses," *J. Opt. Soc. Am.* **73**, 451-455 (1983).
- [53] G. P. Nordin, P. C. Deguzman, "Broadband form birefringent quarter-wave plate for the mid-infrared wavelength region," *Optics Express*, Vol 5, No. 8, October 11, 1999.

VITA

March 1, 1965	Born, South Korea
March 1, 1987	B.A., Air Force Academy, South Korea
May 21, 1998	M.E., Stevens Institute of Technology Hoboken, New Jersey
May 7, 2006	Ph.D., University of Dayton Dayton, Ohio

PUBLICATIONS

Jang Pyo Kim, Andrew M. Sarangan, "Simulation of resonant cavity enhanced (RCE) photodetectors using the finite difference time domain (FDTD) method," Optics Express, Vol 12, No. 20, October 4, 2004.

Jang Pyo Kim, Andrew M. Sarangan, "Design and simulation of resonant cavity enhanced (RCE) corrugated quantum well infrared photodetectors (C-QWIPs)," Applied Optics, Accepted (to be published), 2006.

FIELDS OF STUDY

Major Field: Detector

Studies of RCE Photodetector, Professor Andrew M. Sarangan.

R702032624

The HF Group

Indiana Plant

T 052546 F 31 00



6/8/2006